THE UNIVERSITY OF WAIKATO
Te Whare Wānanga o Waikato
Research Commons

https://researchcommons.waikato.ac.nz/

Research Commons at the University of Waikato

Copyright Statement:

The digital copy of this thesis is protected by the Copyright Act 1994 (New Zealand).

The thesis may be consulted by you, provided you comply with the provisions of the Act and the following conditions of use:

- Any use you make of these documents or images must be for research or private study purposes only, and you may not make them available to any other person.
- Authors control the copyright of their thesis. You will recognise the author's right to be identified as the author of the thesis, and due acknowledgement will be made to the author where appropriate.
- You will obtain the author's permission before publishing any material from the thesis.

In-Situ Assessment of Structural Steel: Correlating Mechanical Properties using Multi-Modal Hardness and Leeb Rebound Testing

Wai Myo Htet

A thesis submitted in fulfillment of the requirements

for the degree of Master of Engineering

Main Supervisor: Dr Zhiyuan (Arthur) Fang

Advisers: Kaveh Andisheh, James Lim, Yi Xiao

School of Engineering

The University of Waikato

New Zealand

2026

Table of Contents

Table of Figures

Table of Tables

Abstract

The in-situ diagnostic assessment of existing carbon steel infrastructure often relies on non-destructive testing (NDT) to estimate structural capacity without compromising member integrity. This study investigates the reliability of multi-modal surface hardness testing as a proxy for macroscopic tensile properties in structural carbon steels. Specifically, Brinell, Rockwell, Vickers, and Leeb hardness measurements are correlated with the 0.2% offset yield strength (YS) and ultimate tensile strength (UTS) of Grade 300 Universal Beams and Grade 350 Square Hollow Sections.

To account for manufacturing-induced heterogeneities, 36 localized coupons were systematically extracted from varying spatial zones, including the web and flanges of hot-rolled profiles. Destructive uniaxial tensile benchmarking confirmed significant spatial variation driven by differential cooling rates during manufacturing, with the thinner, faster-cooling web elements demonstrating an average yield strength nearly 100 MPa higher than the corresponding thicker flange elements. This variation is consistent with the expected differences in thermo-mechanical processing and section geometry.

Bivariate linear regression analyses revealed that predictive performance depends on the testing scale and measurement modality. For yield strength prediction, the macro-scale Leeb rebound method showed strong correlation ($R^2 = 0.947$, MAE = 10.49 MPa, MPE = −0.09%). In contrast, the Vickers micro-indentation method demonstrated greater predictive accuracy for UTS ($R^2 = 0.847$), indicating greater sensitivity to localized plastic deformation behaviour at higher strain levels.

A key observation of this study shows that the reliability of dynamic rebound measurements is strongly influenced by testing boundary conditions. It was observed that uncoupled testing on thin structural elements (< 5 mm nominal thickness) induces kinetic energy dissipation via localized flexure, resulting in significant predictive variance. Consequently, operational guidelines are proposed for field assessments, indicating that rigid coupling for thin-walled elements, or the isolation of uncoupled testing to high-rigidity zones (such as flat flange elements), is necessary to maintain measurement accuracy. Ultimately, this research provides a preliminary framework suggesting that the portable Leeb hardness method can serve as a supplementary diagnostic tool for the yield assessment of these specific steel grades, provided appropriate testing boundary conditions are maintained.

Acknowledgements

I would like to express my sincere gratitude to my supervisory team for their invaluable guidance and support throughout this research. My sincere thanks go to my primary supervisor, Dr Arthur Fang, for his academic rigour and constant encouragement. I am equally grateful to my academic advisors: Kaveh Andisheh (General Manager of Structural Systems at HERA), for his expert guidance in bridging the gap between academic theory and industrial practice, and Yi Xiao, for his mentorship, innovative ideas, and hands-on support during the experimental phase of this work. I also extend my gratitude to Professor James Lim for his support during the initial stages of this research.

I also wish to acknowledge the vital contribution of our industry partners. My sincere appreciation goes to Waikato Steel Fabricators, specifically Tertius Terblanche, Commercial Manager, and Ronald Guy, Production Manager, for their generosity in providing the steel samples essential for my testing.

In the laboratory, I would like to thank Jing Xu, Technical Officer at the School of Engineering, for her expertise and assistance with the experimental setup.

I am grateful to the University of Waikato for providing the facilities and academic environment that made this research possible.

Finally, I would like to thank my family and friends for their endless patience, love, and emotional support. This journey would have been significantly more difficult without their unwavering belief in me.

List of Abbreviations

Testing and Statistical Terminology

- **ASTM:** American Society for Testing and Materials
- **EDS:** Energy Dispersive X-Ray Spectroscopy
- **ISO:** International Organization for Standardization
- **ML:** Machine Learning
- **MPE:** Mean Percentage Error
- **MSE:** Mean Squared Error
- **NDE:** Non-Destructive Evaluation
- **NDT:** Non-Destructive Testing
- **r:** Pearson Correlation Coefficient
- **R^2:** Coefficient of Determination
- **RMSE:** Root Mean Square Error
- **SEM:** Scanning Electron Microscopy

Mechanical Properties, Units, and Hardness Scales

- **HB:** Brinell Hardness
- **HL:** Leeb Hardness
- **HRB:** Rockwell Hardness (Scale B)
- **HV1:** Vickers Hardness (using a 1 kgf load)
- **kgf:** Kilogram-force
- **kN:** Kilonewton
- **MPa:** Megapascals
- **R_a:** Surface Roughness Average (µm)
- **UTS:** Ultimate Tensile Strength
- **YS:** Yield Strength

Structural and Specimen Nomenclature

- **B:** Bottom spatial zone
- **EBF:** Eccentrically Braced Frame
- **IB:** Universal Beam (I-Beam)
- **IB-F:** Universal Beam - Flange extraction
- **IB-W:** Universal Beam - Web extraction
- **M:** Middle spatial zone
- **MB:** Middle-Bottom spatial zone

- **MT:** Middle-Top spatial zone
- **RHS:** Rectangular Hollow Section
- **SHS:** Square Hollow Section
- **SQ:** Square Hollow Section specimen designation
- **T:** Top spatial zone
- **UB:** Universal Beam (I Beam)
- **Wt:** Weight

Chapter 1: Introduction

1.1 Background of the Study

Structural steel components in existing infrastructure often require in-situ assessment of mechanical properties, particularly yield strength and ultimate tensile strength (UTS), to support maintenance, retrofit, and safety evaluation. Conventional characterisation relies on destructive mechanical testing, particularly uniaxial tensile testing performed in accordance with standardized procedures [1], [2]. While these methods provide reliable and reproducible results, they require specimen extraction and loading to failure, rendering them unsuitable for in-situ evaluation of existing structures.

Destructive testing is often impractical for structural health monitoring applications due to cost, logistics, downtime, and the irreversible damage caused to structural components. As infrastructure ages and maintenance demands increase, there is a growing need for alternative techniques capable of estimating mechanical properties with minimal structural disruption. Non-destructive evaluation (NDE) methodologies have therefore become increasingly important in structural engineering practice [3]. Among available NDE approaches, hardness testing has gained significant attention due to its operational simplicity and its well-documented empirical relationship with tensile strength [4], [5].

1.2 Mechanical Property Characterisation in Structural Materials

The mechanical performance of structural steel is primarily characterised by yield strength, ultimate tensile strength (UTS), and post-yield deformation behaviour, which govern structural safety and load-carrying capacity. In many structural steels, the transition from elastic to plastic behaviour is not sharply defined; therefore, the yield strength is conventionally determined using the 0.2% offset method to ensure standardized and repeatable measurements [1], [2] (see Figure 1.1).

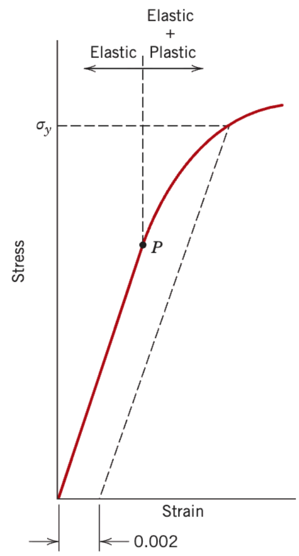

Figure 1.1: Typical engineering stress-strain curve illustrating the 0.2% offset method utilized to determine the standardized yield strength of structural materials exhibiting continuous yielding behaviour. Adapted from [6].

Extensive research has demonstrated that hardness, defined as resistance to localized plastic deformation, correlates with these bulk tensile properties. The theoretical basis for this relationship was established by Tabor, who demonstrated that indentation hardness reflects a constrained plastic flow process related to the material's flow stress [4]. Subsequent studies have refined these empirical relationships. Pavlina and Van Tyne quantified correlations between Brinell hardness and both yield strength and tensile strength for structural steels [5]. Orgánek et al. further examined the relationship between Brinell hardness and strength in structural-grade steels, reinforcing the predictive capability of hardness measurements [7]. Similarly, Lai and Lim investigated the prediction of tensile properties from hardness testing, providing additional statistical validation [8]. These studies collectively support the premise that hardness testing can serve as an alternative indicator of mechanical strength when direct tensile testing is not feasible.

1.3 Hardness Testing as a Non-Destructive Tool

Hardness testing methods such as Brinell, Rockwell, Vickers, and Leeb are standardized under international testing frameworks [9], [10], [11], [12], [13], [14], [15], [16]. These tests introduce localized plastic deformation through controlled indentation or impact, measuring either indentation size, penetration depth, or energy loss to quantify hardness.

Compared to tensile testing, hardness testing offers several advantages:

- Minimal specimen preparation
- Rapid testing time
- Portable equipment availability
- Limited structural damage

Portable devices such as Leeb hardness testers are particularly attractive for field deployment. Research by Brenčič and Campeggio demonstrated the applicability of Leeb hardness for assessing yielding stress in existing structural components [17]. Nashid et al. further explored the non-destructive investigation of hardness-plastic strain relationships under cyclic deformation, highlighting the potential role of hardness testing in structural health monitoring [18].

However, hardness testing is more sensitive to surface condition, microstructural heterogeneity, and testing configuration. Surface roughness has been shown to influence measurement variability [19]. Additionally, conversion between hardness scales must be performed carefully using established standards [20], [21]. Therefore, systematic validation against tensile testing remains essential before hardness-based estimation can be adopted robustly in engineering practice.

1.4 Research Motivation

Although numerous studies demonstrate empirical correlations between hardness and tensile strength, variability exists depending on the specific steel grade, microstructure, and testing method. Many published correlations are material-specific and may not directly apply to the heavily regulated, standardized structural steel grades currently used in construction.

Furthermore, portable hardness testing devices operating on dynamic rebound principles introduce additional uncertainty regarding mass, stiffness, and surface coupling compared to stationary laboratory equipment. Establishing the precise boundary conditions required for these portable tools to function accurately in the field represents a significant gap in current literature. An experimental comparison between field-applicable methods and standardized stationary testing is therefore necessary to establish a reliable predictive framework. This study addresses the need for validated correlations between standardized surface hardness measurements and the mechanical properties of structural-grade steels, with a specific focus on optimizing dynamic testing for in-situ applicability.

1.5 Research Objectives

The primary objective of this research is to evaluate the predictive correlation between non-destructive surface hardness and macroscopic tensile properties. To ensure analytical rigour and clearly define the experimental scope, this study is governed by the following specific objectives:

1. **Material-Specific Characterisation:** To quantify the baseline mechanical properties (0.2% offset Yield Strength and Ultimate Tensile Strength) of specific New Zealand structural steel profiles, limited exclusively to AS/NZS 3679.1 [22] Grade 300 Universal Beams (UB) and Grade 350 Square Hollow Sections (SHS).
2. **Controlled Methodological Evaluation:** To empirically compare four distinct surface hardness testing modalities (Leeb, Vickers, Rockwell, and Brinell) under controlled laboratory conditions. This includes systematically investigating the influence of physical testing parameters, specifically the requirement for rigid heavy-mass coupling during dynamic testing, on diagnostic accuracy.
3. **Targeted Benchmarking and Modelling:** To derive grade-specific bivariate linear regression models linking surface hardness to tensile capacity, and to evaluate predictive error of these localized models against established, generalized international conversion standards (specifically ASTM E140 [21] and SCI P427 [23]).

1.6 Research Scope and Limitations

Scope:

This investigation systematically examines the mechanical behaviour of standardized, modern structural steels. Based on manufacturer mill certificates and standard specifications (such as AS/NZS 3678 and AS/NZS 1163), the study focuses exclusively on structural carbon steel Grades 300 and 350. These grades were selected because they are the most widely utilized and regulated load-bearing materials in the New Zealand and broader Australasian construction industries. By utilizing materials with representative chemical compositions and microstructures representative of the regional industry, the resulting predictive models will have direct, practical relevance to local structural engineering and post-seismic assessment. The study includes:

- Stationary hardness testing in accordance with established ASTM and ISO standards [9], [13], [14], [15], [16].
- Tensile testing according to standardized methodologies to capture stress-strain profiles [1].
- Statistical regression analysis correlating surface hardness with internal yield and tensile strength.
- Evaluation of hardness conversion consistency [20], [21].

Limitations:

Hardness testing fundamentally measures localized surface resistance. Consequently, it may not detect deep internal defects such as subsurface voids, core inclusions, or microcracking. Surface preparation, oxidation, and localized roughness can also influence measurement variability. To mitigate this, environmental variables and surface geometries were strictly controlled during laboratory testing to establish a reliable baseline correlation model. Additionally, the empirical correlations derived in this study are valid only within the specific material classes (Grade 300 and 350) and hardness ranges experimentally investigated.

Chapter 2: Literature Review

2.1 Introduction

The reliable application of non-destructive testing (NDT) in structural health monitoring requires a fundamental understanding of both metallurgical physics and standard mechanical testing protocols. This chapter reviews the existing literature surrounding the mechanical properties of structural carbon steels, with a specific focus on the microstructural mechanisms that govern yield and tensile strength. Furthermore, it evaluates the foundational principles of macroscopic and microscopic hardness testing methodologies; specifically Brinell, Rockwell, Vickers, and dynamic Leeb testing. By examining previously established empirical correlations between localized surface hardness and bulk material strength, this review identifies the current limitations and statistical gaps in predictive structural assessment, thereby establishing the necessary theoretical framework for the experimental methodology conducted in this research.

2.2 Mechanical Properties of Structural Steel

The macro-mechanical performance of engineered structural members, such as Grade 300 Universal Beams and Grade 350 Square Hollow Sections, is strongly influenced by their atomic and microstructural composition. To accurately predict load-bearing capacities using surface NDT methods, the underlying physical properties of the steel must first be understood.

2.2.1 Microstructural Characteristics of Carbon Steels

Standardized structural carbon steels derive their mechanical strength primarily from a dual-phase microstructure consisting of ferrite and pearlite [24]. Ferrite, a body-centred cubic (BCC) solid solution of carbon in iron, is relatively soft and highly ductile. Pearlite, conversely, is a lamellar composite structure comprised of alternating layers of soft ferrite and hard, brittle cementite (Fe_3C), as illustrated in Figure 2.1.

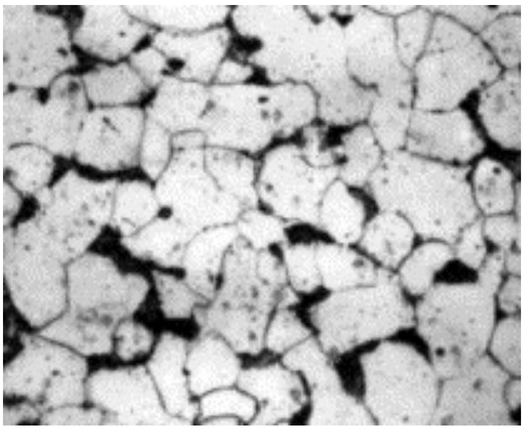

Figure 2.1: Example of micrograph detailing the dual-phase ferrite and pearlite microstructure typical of low-carbon structural steels. Reprinted from [25].

The precise ratio, distribution, and grain size of these two phases govern the bulk mechanical properties of the steel. As the carbon equivalent increases, or as the manufacturing cooling rate is optimized, the volume fraction of pearlite increases, thereby elevating the ultimate tensile strength and hardness of the material [26].

Furthermore, the yield strength of these structural steels is heavily influenced by the Hall-Petch relationship (Figure 2.2), where the refinement of the ferrite grain size creates a higher density of grain boundaries. These boundaries act as physical barriers to dislocation movement (plastic slip) [27].

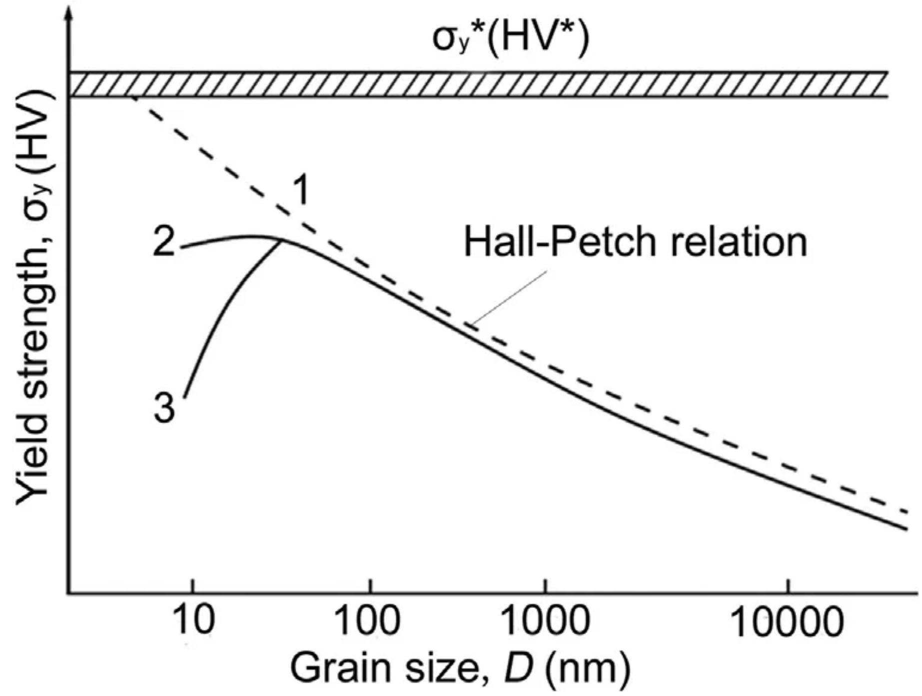

Figure 2.2: Graphical representation of the Hall-Petch relationship, demonstrating the inverse correlation between ferrite grain size and macroscopic yield strength. Adapted from [28].

This relationship is quantitatively expressed as:

$$\sigma_y = \sigma_0 + k_y d^{-\frac{1}{2}} \cdots\cdots\cdots\cdots\cdots\cdots\cdots\cdots \text{(2.1)}$$

where σ_y is the yield stress, σ_0 is the material's constant representing the overall resistance of the crystal lattice to dislocation movement, k_y is the strengthening coefficient, and d is the average grain diameter. Consequently, other testing method, such as surface indentation hardness, are fundamentally measuring the localized resistance of this ferrite-pearlite matrix and its grain boundaries to dislocation glide.

While quantitative metallographic grain size measurements (e.g., via EBSD or intercept methods) were outside the primary experimental scope of this research, the Hall-Petch relationship establishes the physical validity of using hardness as an indicator for tensile strength. Since both yield strength σ_y and hardness (H) follow a similar inverse-square-root relationship with grain diameter (d), a linear correlation between the two macro-mechanical properties is physically expected. In this framework, the surface indentation measurements recorded in this study act as a non-destructive probe of the localized dislocation density and grain-boundary resistance of the ferrite-pearlite matrix, effectively capturing the metallurgical "fingerprint" of the steel's strength without requiring destructive microscopy.

2.2.2 Tensile Testing and the 0.2% Offset Yield Criterion

The universally accepted benchmark for determining the strength of structural steel is uniaxial tensile testing. As a specimen is subjected to an increasing axial load, it initially undergoes elastic deformation, governed by Hooke's Law, where the atomic bonds stretch but do not permanently break. The point at which this elastic behaviour transitions into permanent, plastic deformation is known as the yield point.

While some low-carbon mild steels exhibit a sharply defined upper and lower yield point, modern structural alloys and higher-strength grades (such as cold-formed Grade 350) frequently demonstrate continuous yielding behaviour. In such materials, the transition from elastic to plastic deformation forms a smooth curve on the stress-strain diagram, making the exact point of yielding visually ambiguous.

To resolve this ambiguity and ensure strict repeatability across engineering disciplines, standard testing protocols mandate the use of the 0.2% offset method [1], [2]. This procedure involves plotting a line parallel to the linear elastic modulus of the material, offset by a plastic strain value of 0.002 (0.2%). The intersection of this offset line with the stress-strain curve establishes the standardized yield strength [29].

This offset method relies on a strictly defined mathematical intersection rather than subjective visual interpretation; it serves as the definitive comparative baseline when attempting to correlate surface hardness values to internal bulk yielding limits.

2.3 Principles of Non-Destructive Testing (NDT)

This section explores the fundamental principles of Non-Destructive Testing (NDT) within the context of structural engineering. It first establishes the critical necessity for in-situ assessment methodologies that preserve the physical integrity of active infrastructure. Subsequently, it provides a comparative overview of various NDT modalities, ultimately identifying localized surface hardness testing as the premier non-destructive mechanism for estimating macroscopic mechanical properties.

2.3.1 The Need for In-Situ Assessment

The structural integrity of steel infrastructure is not static; it degrades over time due to cyclic fatigue, environmental corrosion, and unforeseen dynamic loading. While traditional destructive tensile testing provides definitive yield and tensile strength data, it is fundamentally incompatible with the continuous assessment of operational structures [3]. Extracting standardized coupons from an active load-bearing member such as a Grade 300 Universal Beam creates localized stress concentrations and geometrically compromises the member's load capacity. Consequently, the structural engineering industry has increasingly prioritized the development of Non-Destructive Testing (NDT) methodologies that evaluate structural health without inducing macroscopic damage.

2.3.2 Overview of NDT Modalities

NDT encompasses a wide spectrum of diagnostic technologies, each tailored to detect specific material characteristics. For instance, Ultrasonic Testing (UT) uses high-frequency sound waves to detect internal voids and delamination, while Magnetic Particle Testing (MPT) is highly effective at identifying sub-surface cracking in ferromagnetic materials. However, while these methods excel at flaw detection, they cannot directly quantify the mechanical yielding limits of the steel.

To estimate structural capacity and tensile strength, surface hardness testing emerges as the most viable NDT modality. By inducing localized, microscopic plastic deformation, hardness testing probes the same atomic dislocation mechanisms that govern macroscopic yielding, allowing engineers to infer bulk mechanical properties entirely non-destructively [4], [30].

2.4 Hardness Testing Methodologies

Hardness is not a fundamental physical property like mass or density; rather, it is an empirical measurement of a material's resistance to localized plastic deformation. The mechanical basis linking indentation hardness to bulk flow stress was foundationally established by Tabor, who demonstrated that hardness (*H*) is proportional to the representative flow stress σ_f of the material at a specific plastic strain [4]. This is mathematically expressed as:

$$H \approx C.\sigma_f \cdots\cdots\cdots\cdots\cdots\cdots\cdots\cdots\cdots\cdots\cdots \text{(2.2)}$$

where *C* is a constraint factor typically approximating 3 for fully plastic indentation in metals[4]. Consequently, hardness values are dependent on the geometry of the indenter and the applied loading conditions.

2.4.1 Static Indentation Hardness

Static methods apply a controlled, constant load to press an indenter into the surface of the steel. The resulting permanent deformation is then measured.

- **Brinell Hardness (HB):** Standardized under ISO and ASTM specifications [9], [13], the Brinell method presses a hard tungsten carbide spherical ball into the steel under a heavy load. The hardness value is calculated based on the surface area of the resulting circular impression, as illustrated in Figure 2.3.

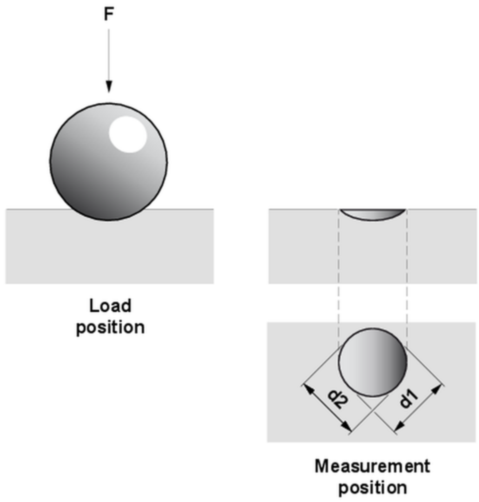

Figure 2.3: Schematic illustration of the Brinell hardness test principle. A standardized test force (F) is applied via a hard spherical indenter, and the resulting indentation is evaluated by measuring two perpendicular diameters (d1 and d2), in accordance with ASTM [13].

- **Rockwell Hardness (HR):** Standardized under ISO and ASTM specifications [11], [14], the Rockwell method differs fundamentally from Brinell by measuring the depth of penetration rather than the surface area (Figure 2.4). It utilizes either a diamond cone (for harder alloys) or a hardened steel ball (for softer steels). A minor preliminary load is applied to seat the indenter and eliminate surface-finish errors, followed by a major load. The difference in penetration depth between the two loads yields the hardness value, offering a rapid, direct readout without the need for optical microscopy.

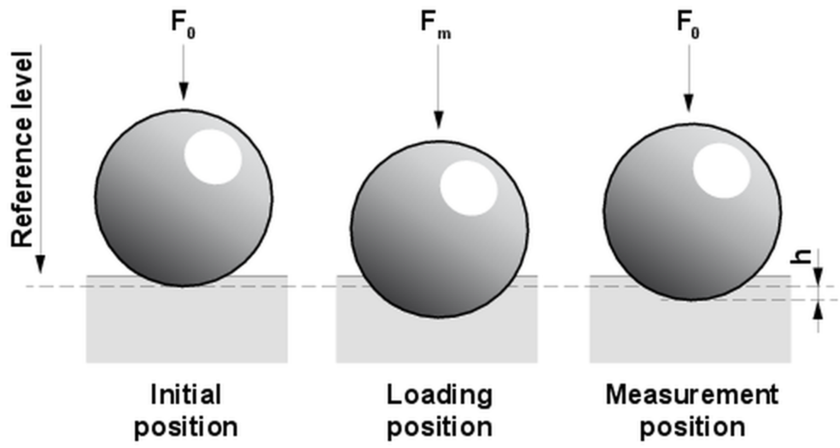

Figure 2.4: Principle of the Rockwell hardness test, showing the minor load (F0), major load (Fm), and resulting depth of penetration (h)[14]

- **Vickers Hardness (HV):** Standardized under ISO and ASTM specifications [12], [15], the Vickers test utilizes a square-based diamond pyramid indenter (Figure 2.5). A key advantage of the Vickers method is its geometric similarity: the shape of the indentation is identical regardless of the applied load. This allows the Vickers scale to be continuous across both macro-hardness and micro-hardness testing, making it ideal for examining specific microstructural phases or the heat-affected zones of steel welds.

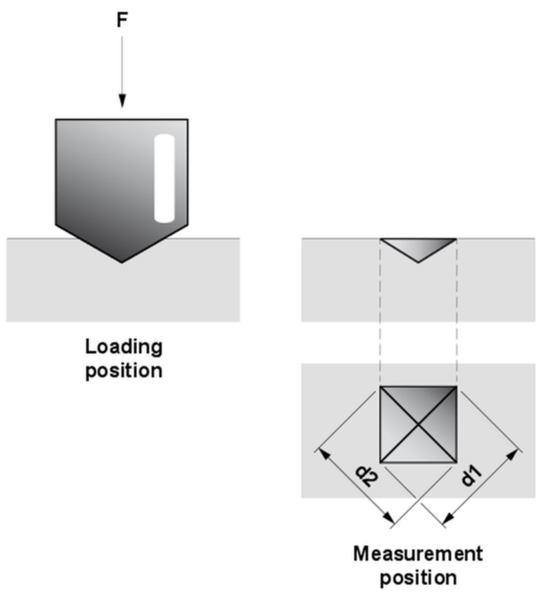

Figure 2.5: Principle of the Vickers hardness test, showing the test force (F) and measurement of the indentation diagonals (d1, d2) [15].

- **Suitability for Tensile Prediction:** When evaluating these static methods for their suitability in predicting bulk tensile properties, literature indicates that Brinell hardness provides robust reliability for macro-scale structural steels[5]. Given that the Brinell indenter creates a comparatively large impression, it is generally considered effective at averaging out localized microstructural heterogeneities. Nevertheless, while the Vickers method provides precision across a continuous hardness scale, its micro-indentation footprint can increase sensitivity to individual microstructural phases, such as ferrite or pearlite grains. Studies suggest this sensitivity may introduce data scatter when extrapolating micro-scale readings to the macroscopic bulk yield strength of structural members[31]. Rockwell testing offers a rapid operational alternative; however, as it relies on depth of penetration rather than optical surface area measurement, it requires stringent surface preparation to minimize variance. Consequently, several foundational predictive models for structural carbon steels have utilized the macroscopic footprint of Brinell hardness to establish baseline tensile correlations [5], [31].

2.4.2 Dynamic Rebound Hardness

While static indentation is the laboratory benchmark, stationary machines cannot be deployed on existing infrastructure. Dynamic hardness testing resolves this logistical limitation.

Leeb Hardness (HL): The Leeb method, governed by [16], operates on the principle of dynamic kinetic energy loss. A portable device propels an impact body against the steel surface using spring force. The impact causes localized plastic yielding, consuming kinetic energy, as illustrated in Figure 2.6.

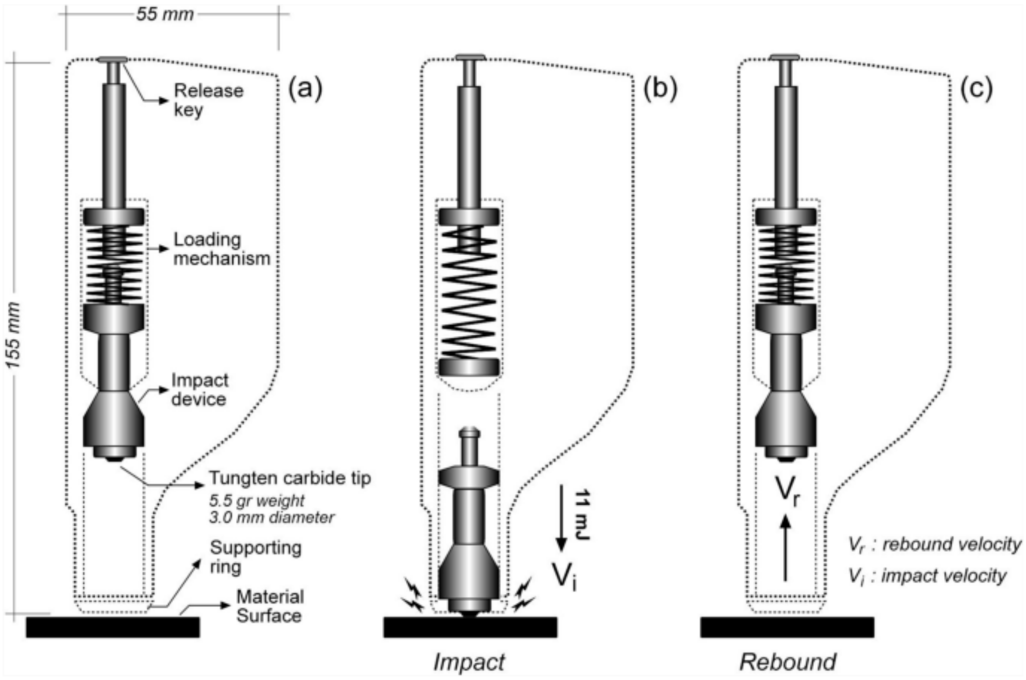

Figure 2.6: Operational principle of the Leeb dynamic rebound hardness test, demonstrating the internal impact body, induction coil, and the measurement of electromotive force to calculate kinetic energy loss. Adapted from [32].

The Leeb hardness value (HL) is quantitatively defined as the ratio of the rebound velocity v_r to the impact velocity v_i, multiplied by 1000[16]:

$$HL = \frac{v_r}{v_i} \times 1000 \cdots\cdots\cdots\cdots\cdots\cdots\cdots\cdots\cdots \text{(2.3)}$$

Mechanics and Limitations of Dynamic Methods: As the Leeb test relies strictly on the conservation of momentum and energy, it is acutely sensitive to the structural boundary conditions of the test subject. If the target steel member lacks sufficient mass, or if its thickness is below the operational threshold (typically 5 mm for standard Type D impact bodies, detailed in Figure 2.7), kinetic energy is lost to macroscopic structural vibration and flexure rather than purely localized plastic yielding.

Impact Device	Minimum Mass without Rigid Support	Minimum Mass with Rigid Support	Minimum Thickness (Uncoupled)	Minimum Thickness (Coupled)
D, DC, D+15, *DL, S, E*	11.0 lb [5 kg]	4.4 lb [2 kg]	0.984 in. [25 mm]	0.118 in. [3 mm]
G	33.1 lb [15 kg]	11.0 lb [5 kg]	2.756 in. [70 mm]	0.394 in. [10 mm]
C	3.3 lb [1.5 kg]	0.3 lb [0.5 kg]	0.394 in. [10 mm]	0.039 in. [1 mm]

Figure 2.7:Minimum thickness and mass boundary conditions required to prevent kinetic energy loss and data scatter during dynamic rebound testing, as defined by ASTM A956. Adapted from [16].

This vibrational energy loss leads to artificially low rebound velocities and severe data scatter [17]. Therefore, for Leeb testing to produce reliable predictions, the steel must exceed minimum stiffness thresholds and remain rigidly coupled.

2.5 Empirical Correlations Between Hardness and Tensile Properties

The theoretical relationship between indentation resistance and bulk plastic flow has driven decades of research aimed at mathematically predicting tensile properties from surface hardness. However, these predictive models have evolved significantly from generalized historical approximations to specific, statistically validated structural frameworks [4], [5], [33].

2.5.1 Historical and Material-Specific Correlation Models

Early efforts to correlate hardness with mechanical strength relied on broad, linear approximations designed primarily for rapid quality control. The most widely recognized historical relationship is the direct proportionality between ultimate tensile strength (UTS) and Brinell hardness (HB), often approximated using a material-specific coefficient [34], [35].These foundational linear models are institutionalized in international conversion tables [20], [21].

However, modern metallurgical research has shifted toward developing high-fidelity empirical correlations tailored to exact material classes. Recent studies have demonstrated that while ultimate tensile strength correlates linearly with hardness across broad material spectra, yield strength exhibits a much higher degree of variance depending on the steel's microstructural homogeneity and thermo-mechanical processing [5], [7], [36]. For structural-grade steels, achieving a reliable prediction of the strictly defined 0.2% offset yield limit requires highly localized, material-specific baseline testing [8], [29].

2.5.2 Dynamic Rebound Correlations in Structural Applications

While static models generally perform reliably in controlled laboratory conditions, transitioning these predictive frameworks to in-situ infrastructure requires a careful evaluation of dynamic rebound methodologies. The Leeb hardness method measures kinetic energy loss by inducing an electromotive force (EMF) via a magnet passing through an induction coil during impact and rebound [37].

Recent literature has investigated the Leeb method's application for estimating residual strength and ultimate tensile limits directly on structural members, including H-shaped beams and steel plates [38], [39], [40]. However, studies note that the accuracy of these dynamic correlations can degrade when applied to non-ideal surface morphologies. Hardness testing, particularly dynamic rebound, exhibits a known sensitivity to surface irregularities. Microscopic peaks and valleys can alter the effective contact area and disrupt the rebound trajectory, potentially leading to increased data scatter and measurement variance [17], [19].

Consequently, for portable Leeb testing to yield statistically viable correlations for Grade 300 and 350 steels, appropriate surface preparation (e.g., localized grinding) and rigid structural coupling protocols are generally required to minimize parasitic vibrational energy loss.

2.5.3 The Impact of Surface Morphology

While material-specific models perform exceptionally well under stationary laboratory conditions, their accuracy often degrades when applied to in-situ environments using portable NDT equipment. The primary physical variable responsible for this degradation is surface morphology.

Hardness testing, particularly micro-indentation (Vickers) and dynamic rebound (Leeb), measures highly localized resistance. Consequently, surface irregularities can introduce measurement uncertainty. Gadelmawla et al. [19] demonstrated that surface roughness influences measurement variability; microscopic peaks and valleys alter the effective contact area of the indenter, which can lead to skewed readings.

In field testing, structural steel is frequently covered in mill scale, oxidation, or protective primers. When these layers are mechanically ground away to prepare a testing surface, the grinding process itself can introduce work-hardening to the extreme outer layer of the steel, artificially inflating the hardness reading compared to the bulk internal material. This compounding error is directly corroborated by Katok et al. (2022), who demonstrated that while the naturally occurring decarburized outer layer of high-strength steels artificially underestimates actual hardness, the mechanical grinding required to expose the true base metal introduces residual surface stresses that further distort the diagnostic measurement [41]. Furthermore, Gušin et al. (2019) emphasize that the inherent uncertainty of field hardness measurements is inextricably linked to these surface preparation methods, confirming that any mathematical correlation must strictly account for preparation-induced variances [42].

Furthermore, as noted by Brenčič and Campeggio [17], failing to achieve a sufficiently smooth and flat surface geometry can prevent the proper coupling of portable Leeb devices, resulting in erratic kinetic energy loss and increased data scatter. Therefore, for an empirical correlation to remain valid, defined surface preparation protocols are typically integrated into the predictive methodology.

To circumvent the physical limitations of surface preparation and the inherent data scatter of traditional methods, recent research has increasingly explored advanced laboratory diagnostic modalities. For instance, Kharchenko et al. (2022) demonstrated that utilizing instrumented indentation, which continuously registers the force and depth of local deformation rather than relying on a single static measurement, can predict the strength characteristics of high-strength steels with a highly minimized deviation of less than 5.2% from standard tensile tests [43]. Similarly, emerging advancements by Qian et al. (2025) have proven the viability of nonlinear laser ultrasonics for the entirely non-contact evaluation of steel mechanical properties [44].

However, while both instrumented indentation and laser ultrasonics represent highly accurate trajectories for laboratory-grade non-destructive evaluation, they require complex continuous-monitoring equipment, sophisticated thermo-mechanical coupling, and advanced data processing frameworks. Consequently, while these methods successfully reduce predictive variance in a controlled environment, optimizing highly portable and economically viable equipment, such as the Leeb dynamic rebound tester, remains the most practical immediate solution for the in-situ, real-world assessment of standardized structural steel.

2.5.4 Post-Earthquake Non-Destructive Assessment of New Zealand Structural Steel

Following the devastating Canterbury earthquake series, the structural engineering community in New Zealand increasingly prioritized the localized, non-destructive evaluation (NDE) of existing steel infrastructure. The necessity to determine the residual capacity of active yielding links without compromising the structural integrity of buildings drove significant advancements in portable hardness testing methodologies.

Nashid (2014) pioneered the application of non-destructive hardness testing, specifically utilizing Leeb and Rockwell methodologies, to estimate plastic strain accumulation in the active links of eccentrically braced frames (EBFs) [18]. While the research demonstrated the feasibility of correlating hardness increases with cyclic plastic deformation, Nashid identified significant operational complexities. A primary limitation was the presence of inherent, manufacturing-induced plastic strains within hot-rolled structural beams [18]. These pre-existing strains severely convoluted the in-situ hardness readings, making purely empirical post-earthquake damage assessments highly challenging without strict, pre-yield baseline data.

Similarly investigating the post-yield behaviour of New Zealand steels, Loporcaro (2017) conducted extensive research on the effects of strain-ageing and low-cycle fatigue, specifically focusing on Grade 300E reinforcing bars [45]. Loporcaro demonstrated that post-seismic strain-ageing drastically alters the mechanical properties of the steel over time, effectively reducing the residual fatigue life of the material by 20% to 70% following an initial yield event [45].

While Nashid and Loporcaro demonstrated the viability of NDT for post-earthquake damage assessment in New Zealand, their findings highlighted a methodological requirement: the need to establish baseline hardness-to-tensile mathematical correlations for un-yielded structural steel [45]. Understanding the fundamental, as-manufactured relationship between surface hardness and tensile strength provides a necessary baseline before post-yield or post-seismic NDE can be reliably conducted. This foundational requirement informed the predictive baseline modelling undertaken in this current study.

2.5.5 Synthesis of Existing Predictive Models for Structural Steel

While global literature provides generalized conversion tables, establishing high-fidelity predictive models for modern structural steel requires localized, strictly controlled testing. Recent empirical investigations at the University of Waikato have sought to refine these correlations by comparing multiple hardness modalities directly against standardized tensile data across specific regional steel grades.

Foundational baseline data was established by Mohammed (2024), whose research demonstrated the initial viability of utilizing specific NDT indentation metrics as an alternative for destructive coupon testing [46]. Building upon this framework, Gopi (2024) significantly expanded the experimental matrix to encompass certified structural grades, specifically Grade

300, Grade 350, and Grade 400, coupling localized surface evaluations with benchmark uniaxial tensile and Charpy impact data[47].

However, rather than viewing these historical standards and recent local studies as isolated datasets, it is necessary to synthesize their methodologies to identify the persistent gaps in predictive accuracy. Table 2.1 summarizes the current landscape of hardness-to-tensile mathematical correlations, highlighting the primary limitations that prevent their seamless integration into New Zealand field assessments.

Table 2.1: Summary of Existing Hardness-to-Tensile Predictive Models

Source / Standard	Target Property	Predictive Methodology / Equation	Primary Limitations for Regional Application
SCI P427 (European Guidelines) [23]	Yield Strength (YS) Ultimate Tensile (UTS)	$f_y = 2.70(HV) - 71$ $f_u = 2.50(HV) + 100$	Generalized for European steel reuse. Introduces high residual error and over-prediction when applied to the specific microstructural and strain-hardened properties of modern AS/NZS hot-rolled and cold-formed profiles.
ASTM E140 (Annex A10) [21]	Scale Conversion	High-order mathematical polynomials (e.g., converting dynamic Leeb to static Vickers).	Introduces compounding mathematical error when utilized as a mandatory intermediate step prior to calculating tensile strength.
Mohammed (2024) & **Gopi (2024)** [46], [47]	YS & UTS (Local NZ Steels)	Multi-modal trendlines generated across Grade 300, 350, and 400 steels.	Relied partially on generalized theoretical conversions (like SCI P427) rather than direct empirical derivation; baseline destructive data experienced variance due to instrumentation limitations. Furthermore, dynamic rebound (Leeb) evaluations exhibited data scatter.

As demonstrated in the synthesis above, the primary limitation of existing frameworks is their reliance on generalized, global approximations or multi-step scale conversions. This aligns with recent findings by Redecki et al. (2026)[48], who demonstrated that even well-established static hardness methodologies require localized calibration rather than relying on universal, generalized equations. To apply NDT predictive models to structural engineering environments with higher confidence, empirical data must be derived from direct experimental correlation, completely bypassing theoretical substitutions. Rather than maintaining a multi-grade exploratory focus, there is immense value in isolating and refining predictive models for specific, widely utilized materials. Consequently, this research targets standardized Grade 300 Universal Beams and Grade 350 Hollow Sections. By narrowing the experimental focus to these foundational construction grades, this study aims to minimize the statistical divergences highlighted in Table 2.1 and establish targeted, direct predictive models for potential field deployment.

2.6 Statistical Evaluation of Predictive Models

The transition from raw data to a reliable Non-Destructive Testing (NDT) protocol requires rigorous statistical validation. Developing a predictive model that translates localized surface hardness into bulk tensile properties, such as the 0.2% offset yield strength, relies on quantifying both the strength of the correlation and the magnitude of the predictive error.

2.6.1 Correlation Coefficients

The foundational step in validating a predictive relationship between hardness and mechanical strength is establishing linear dependency. This is universally quantified in engineering literature using the Pearson correlation coefficient (r). The Pearson coefficient measures the linear covariance between two variables (e.g., Leeb rebound velocity and uniaxial yield strength), returning a value between -1 and 1.

In the context of structural materials, an r value approaching +1 indicates a high-fidelity positive linear relationship, justifying the use of surface indentation as a surrogate for destructive tensile testing. However, while a high Pearson coefficient confirms that a relationship exists, it does not assess the accuracy of the mathematical model used to predict future values.

2.6.2 Error Quantification and Model Accuracy

While historical standards and global conversion tables predominantly assume a linear regression relationship between hardness and ultimate tensile strength (e.g., $UTS = k.HB$), recent structural literature has increasingly explored nonlinear, polynomial, and power-law regression models to better capture the complex strain-hardening behaviours of modern alloys [5]. To evaluate whether a linear or non-linear predictive hardness-to-tensile model is practically reliable, the variance between the predicted values and the actual laboratory benchmark data must be stringently quantified. This research uses two error metrics:

- **Mean Squared Error (MSE):** The MSE measures the average of the squares of the errors; that is, the average squared difference between the estimated values and the actual benchmark values derived from the standardized tensile tests. By mathematically squaring the errors, the MSE heavily penalizes large predictive outliers [49]. This makes it a critical metric for structural engineering, where overestimating yield strength on a single beam can lead to disproportionate structural failure.
- **Mean Percentage Error (MPE):** While MSE provides a measure of variance, the MPE offers a highly practical relative assessment. In field applications of NDT, engineers require a clear percentage-based confidence interval (e.g., "± 5% error") when assessing the residual capacity of existing Grade 300 and 350 structural members. Minimizing the MPE ensures the model is viable for industry use.

2.7 Summary and Research Gap

The existing literature extensively documents the metallurgical basis for utilizing hardness testing as a non-destructive method for predicting the mechanical properties of steel. Foundational studies establish the physics of static and dynamic indentation, while localized empirical models, such as those developed by Mohammed [46] and Gopi [47], confirm the statistical viability of these correlations on structural carbon steels.

The Research Gap: Despite advancements in generalized metallurgical models, opportunities remain in optimizing non-destructive methodologies for immediate, localized field application. Specifically, this research addresses three interrelated gaps:

1. **Refining correlations for specific New Zealand structural steels:** Existing global conversion formulas do not account for the specific manufacturing tolerances, microstructural profiles, and strain-hardened properties of AS/NZS standardized Grade 300 and 350 steels, often leading to over-prediction and high residual error.
2. **Further evaluation of portable hardness methods:** While stationary static hardness (Brinell/Vickers) is well-established, the reliability of dynamic rebound (Leeb) testing on these specific structural profiles requires further validation, particularly regarding surface preparation and boundary condition variables.
3. **Deriving targeted statistical predictive models:** Previous regional datasets have highlighted the variance introduced by relying on theoretical formulas[46], [47]. There is a need to develop targeted empirical models that aim to minimize prediction variance (MSE and MPE) for the 0.2% offset yield strength.

Chapter 3: Methodology

3.1 Introduction

This chapter describes the experimental methodology used to investigate the relationship between surface hardness and the mechanical properties of structural steel. The study focuses on Grade 300 Universal Beams (UB) and Grade 350 Square Hollow Sections (SHS), representing commonly used structural steel profiles.

An empirical testing framework was established to enable direct comparison between non-destructive hardness measurements and destructive tensile properties. The methodology consists of a two-stage experimental program, including multi-modal hardness testing and benchmark uniaxial tensile testing. Section 3.2 details the material sourcing, precision extraction, and stringent surface preparation protocols required to mitigate morphological data scatter. Section 3.3 defines the multi-modal non-destructive hardness testing matrix, encompassing the specific operational parameters for Brinell, Vickers, Rockwell, and portable Leeb methodologies. Finally, Section 3.4 details the benchmark destructive uniaxial tensile testing utilized to derive the true yield and ultimate tensile strengths, which serve as the empirical foundation for the final mathematical correlations.

3.2 Materials and Specimen Preparation

This section details the physical materials utilized in the experimental program and the comprehensive preparation methodologies applied to ensure baseline testing validity. It first outlines the procurement and precision extraction of the 36 standardized steel coupons, emphasizing the preservation of inherent microstructural properties during the cutting phase. Subsequently, it details the progressive mechanical polishing protocols required to achieve the optimal surface topography necessary for high-fidelity non-destructive hardness evaluation.

3.2.1 Material Sourcing and Specimen Extraction

Standardized Grade 300 Universal Beams (UB) and Grade 350 Square Hollow Sections (SHS) were procured through Waikato Steel Fabricators Ltd. The chemical composition and baseline mechanical properties of the sourced steel were verified against the manufacturer's mill certificates, which are provided in Appendix A. Figure 3.1 illustrates the raw steel sections upon delivery, prior to specimen extraction and indicating the typical extraction zone for SHS and UB which is subsequently detailed in Figure 3.3.

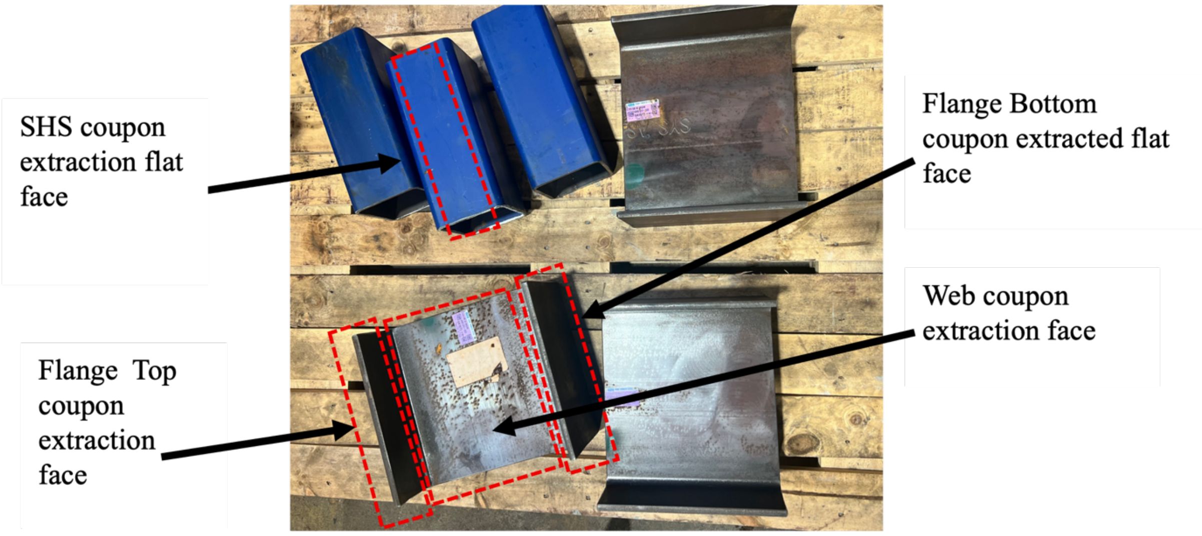

Figure 3.1: As-received Grade 300 UB and Grade 350 SHS steel samples prior to specimen extraction.

Specimen extraction was carried out using abrasive water jet cutting to minimize thermal effects associated with conventional cutting processes, such as the formation of heat-affected zones (HAZ). The cutting was performed by NDL Engineering. The specimens were precision-cut into standardized "dog-bone" geometries in strict accordance with ASTM A370 specifications for the mechanical testing of steel products [2]. Figure 3.2 details the specific dimensional geometry of the specimens used for this research.

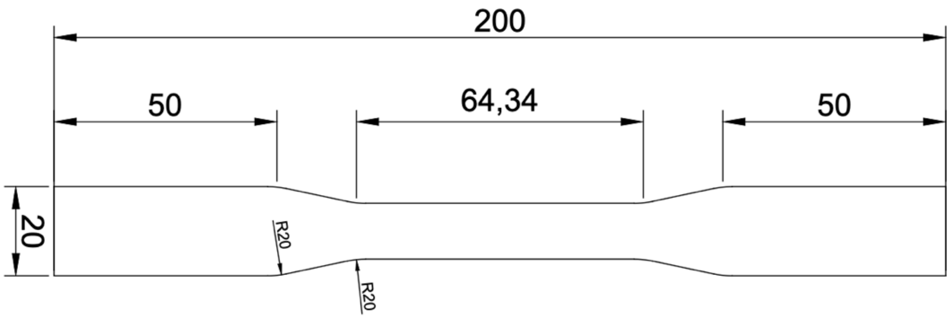

Figure 3.2: Schematic of the standardized dog-bone tensile test specimen geometry (all dimensions in mm)

The final extracted test coupons, ready for experimental analysis, are shown in Figure 3.3.

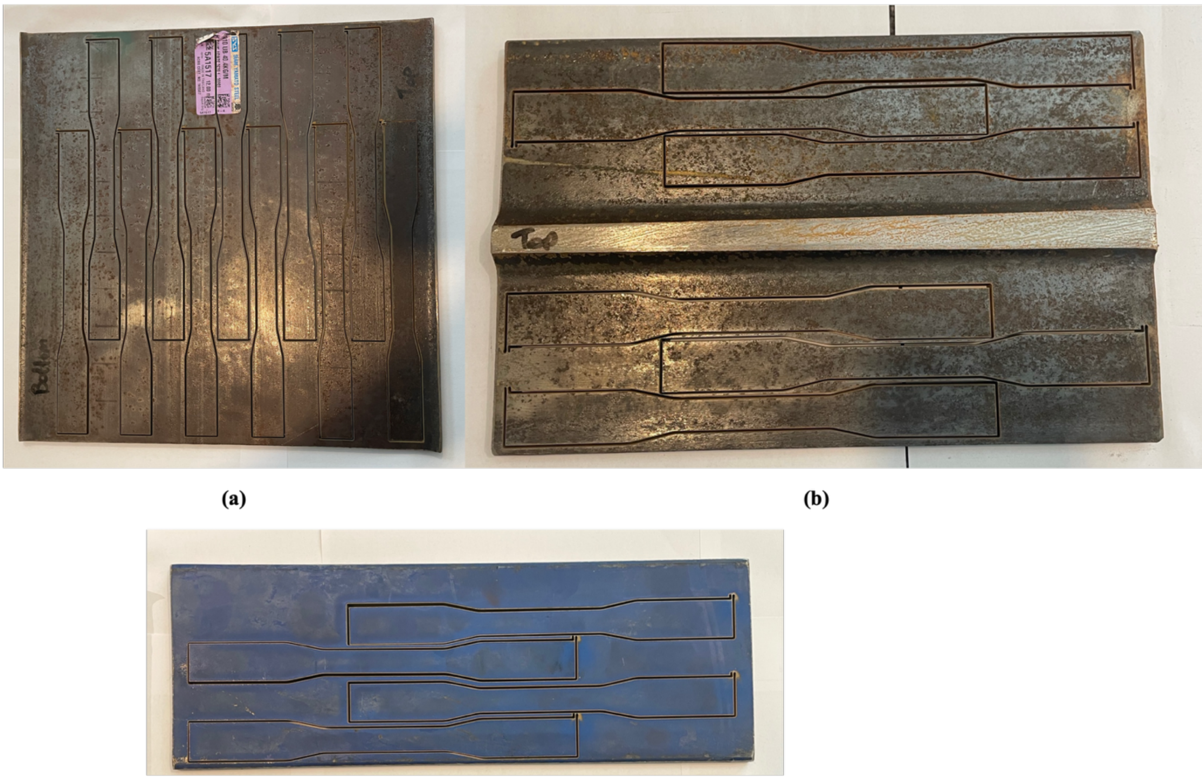

(a) (b) (c)

Figure 3.3: Specimen extraction layouts via water jet cutting to preserve microstructural integrity (a) UB Web (b) UB Flange (c) SHS

A total of 36 individual coupons were extracted to form the experimental matrix. To account for potential microstructural and residual stress variations inherent to the manufacturing process, the coupons were systematically extracted and indexed according to their spatial origin:

- **Grade 300 (UB) Web:** 11 coupons extracted from the web section, with an average thickness of 5 to 6 mm. These specimens were indexed across the vertical profile of the web, categorized precisely as Top, Middle-Top, Middle, Middle-Bottom, and Bottom extraction zones.
- **Grade 300 (UB) Flange:** 12 coupons extracted from the flange sections, with an average thickness of approximately 10 mm. These were explicitly tracked and designated based on their extraction from either the superior (top) or inferior (bottom) flange.
- **Grade 350 (SHS):** 13 coupons extracted from the flat faces of the hollow sections, with an average thickness of 5 to 6 mm.

3.2.1.1 Specimen Nomenclature

To ensure consistency across all subsequent empirical data and statistical modelling, a standardized alphanumeric nomenclature system was established for all 36 extracted specimens. The naming convention systematically identifies the structural profile, the specific macroscopic component, and the precise spatial extraction zone, formatted as follows:

- **SQ (Square Hollow Section):** Denotes Grade 350 structural steel. These specimens are numbered sequentially (e.g., SQ-1, SQ-2).

- **IB-W (Universal Beam - Web):** Denotes Grade 300 structural steel extracted specifically from the web of the I-beam. To track cooling-rate variances across the height of the web, these are tagged with a spatial identifier:
  - **T:** Top
  - **MT:** Middle-Top
  - **M:** Middle
  - **MB:** Middle-Bottom
  - **B:** Bottom

*(Example: **IB-W-MT** designates a coupon extracted from the middle-top spatial zone of the I Beam web).*

- **IB-F (Universal Beam - Flange):** Denotes Grade 300 structural steel extracted specifically from the flange of the I-beam. These are tagged to differentiate between the superior and inferior flanges:
  - **T:** Top Flange
  - **B:** Bottom Flange

*(Example: **IB-F-B** designates a coupon extracted from the bottom flange of the I Beam).*

3.2.2 Surface Preparation and Topography Control

As established in the literature review, precise surface morphology is critical to mitigating data scatter in non-destructive hardness testing. To remove inherent mill scale and oxidation without introducing artificial work-hardening to the localized surface layer, a strictly controlled, two-stage mechanical polishing protocol was implemented.

Initial macro-removal of the native mill scale was conducted using a high-speed rotary tool (Dremel 3000) equipped with an abrasive profile, see Figure 3.4(a). To prevent microstructural phase changes or the induction of artificial surface stresses driven by high-RPM friction, sustained or concentrated polishing in isolated areas was strictly avoided.

Following the removal of the macroscopic scale, the specimens underwent a manual sanding phase utilizing successively finer abrasive papers, culminating in a P800-grit finish. This continuous, sweeping application ensured the uniform removal of the decarburized layer while effectively preserving the original residual stress profile of the base metal.

Following mechanical preparation, the surface topography of each coupon was quantitatively verified using a portable surface roughness tester (Time 3221), as shown in Figure 3.4(b). The surface roughness average (R_a) was maintained below 0.4 µm. Achieving this sub-0.4 µm threshold was a critical prerequisite mandated by the Vickers micro-indentation testing, which requires a highly polished surface to ensure optical measurement accuracy and prevent localized surface asperities from influencing the micro-scale deformation. Additionally, this finish exceeded the operational requirements for the dynamic Leeb rebound test (which specifies a maximum R_a of 1.6 µm [16]), thereby ensuring proper mechanical coupling and mitigating kinetic energy loss across all testing modalities.

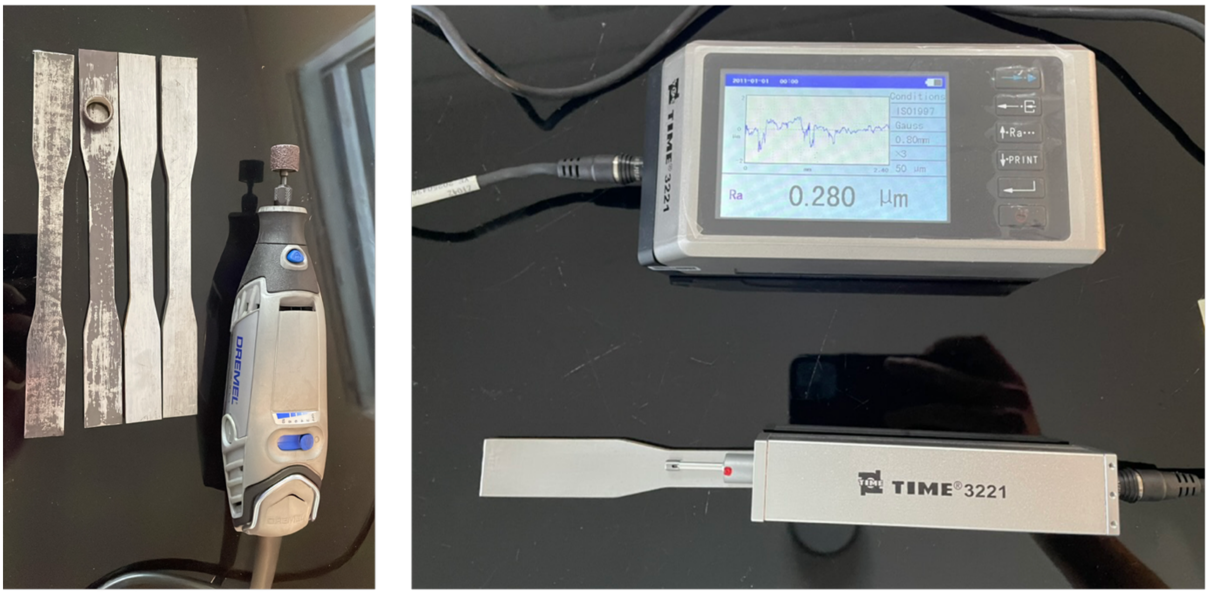

(a) (b)

Figure 3.4: Equipment utilized for surface topography control: (a) Dremel 3000 high-speed rotary tool for mechanical polishing, and (b) Time 3221 portable surface roughness tester used to verify the R_a < 0.4µm threshold requirement.

The physical transformation achieved via this mechanical protocol is visually documented in Figure 3.5, illustrating the stark transition from the raw condition to the final P800-grit finish required for testing topography.

(a) (b)

Figure 3.5: Specimen surface conditions: (a) Raw structural extraction exhibiting native mill scale and atmospheric oxidation; and (b) Final mechanically hand-polished surface requisite for high-fidelity non-destructive evaluation.

3.2.3 Experimental Testing Sequence

To generate the necessary data for the predictive correlation models, a sequential, multi-modal testing framework was established for each of the 36 prepared coupons. Prior to any destructive evaluation, each standardized dog-bone coupon was subjected to a comprehensive localized hardness matrix. This non-destructive matrix consisted of four distinct hardness methodologies (Brinell, Vickers, Rockwell, and Leeb), with five spatially distributed test points executed per method on every individual coupon to establish a statistically viable mean hardness value. Following the completion of the 20 localized hardness indentations per sample, the coupons were subjected to destructive uniaxial tensile testing utilizing an Instron universal testing machine to record the benchmark macro-mechanical yield and ultimate tensile strengths.

3.3 Non-Destructive Hardness Testing Procedures

Following surface preparation and topographical verification using the Time 3221 roughness profilometer, the 36 extracted coupons were subjected to a multi-modal hardness evaluation matrix. To ensure statistical reliability and account for localized microstructural variations, five spatially distributed indentations were executed for each of the four testing methods per coupon, resulting in a 20-point testing matrix for every specimen.

To minimize the influence of localized plastic deformation and potential work-hardening effects, sufficient spacing was maintained between individual indentations. While standardized testing protocols (Figure 3.6) dictate a minimum centre-to-centre spacing of three times the indentation diameter (≥ 3d) and an edge clearance of two and a half times the diameter (≥ 2.5d), the actual experimental execution deliberately exceeded these baseline requirements.

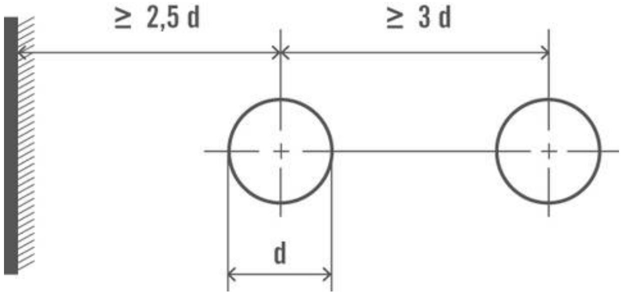

Figure 3.6: Standard baseline spacing requirements for indentations from edge and center to center.

To provide a conservative safeguard against microstructural interference, the test points were conservatively distributed across both the wider 20 mm grip sections and the 12.5 mm parallel gauge length (Figure 3.7). This strategic mapping maximized the available surface area, resulting in inter-indentation distances significantly greater than the code minimums while still accommodating the dense 20-point evaluation matrix.

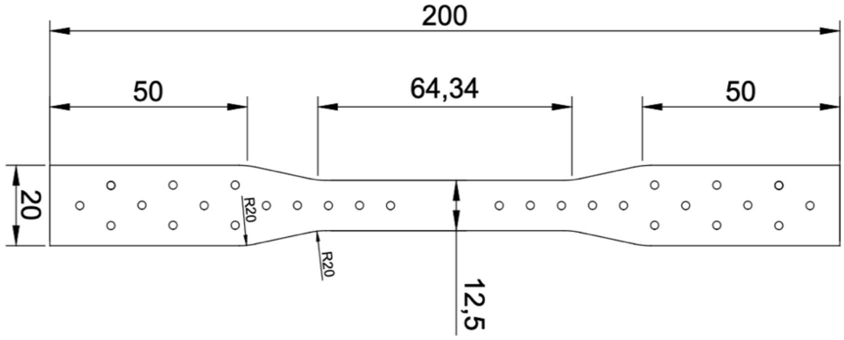

Figure 3.7: Schematic of hardness testing points exceeding the baseline spacing to ensure isolation of localized strain hardening zones.

3.3.1 Portable Dynamic Rebound Testing (Leeb)

To establish the baseline data required for optimizing in-situ field diagnostics, dynamic rebound testing was conducted utilizing a TIME 5100 portable Leeb hardness tester (Figure 3.8). The device was equipped with a standard Type D impact body, utilizing a tungsten carbide test tip. Measurements were executed in strict compliance with ASTM A956 standard test methods for the Leeb hardness testing of steel products [16]. The dynamic rebound velocity quotient (HL) was recorded at five distinct locations across the polished gauge length of each coupon.

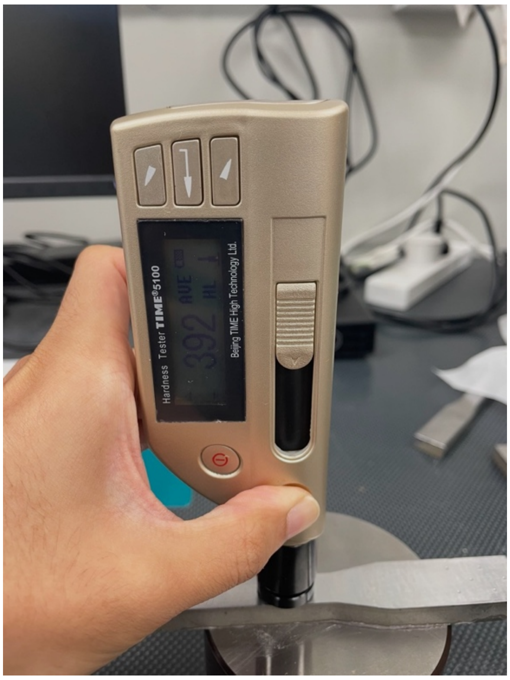

Figure 3.8: The TIME 5100 portable Leeb hardness tester utilized for dynamic rebound evaluations, equipped with a standard Type D impact body.

Measurements were executed with consideration of both international standards and manufacturer operational limits. While ASTM A956 [16] dictates highly conservative boundary conditions for uncoupled specimens (25 mm minimum thickness), the TIME 5100 manufacturer specifies an operational capability for direct, uncoupled testing on specimens exceeding 5 mm in thickness and 5 kg in mass. Therefore, to establish a reliable baseline, the extracted laboratory coupons (5≤ mm thick, <5 kg) were rigidly coupled to a support block to strictly satisfy ASTM requirements. Subsequent in-situ evaluations on full structural members utilized the manufacturer's verified operational thresholds (>5 mm, >5 kg) to accurately capture authentic field-testing conditions without the need for artificial coupling.

During the initial phase of Leeb testing, specimens were mechanically clamped to a rigid support table (Figure 3.9 (a)). However, preliminary data analysis revealed severe kinetic energy dissipation (resulting in artificially low HL values), indicating that mechanical clamping alone failed to achieve the rigid acoustic boundary conditions required for 5-6 mm coupons. Consequently, the methodology was refined. To strictly satisfy ASTM A956 [16] requirements for rigid coupling, a viscous acoustic couplant (petroleum jelly) was applied between the unpolished back face of the coupons and a high-mass reference metal block (Figure 3.9 (b)). This viscous layer successfully displaced microscopic air voids, creating a continuous acoustic boundary that allowed the specimen and the block to act as a single, infinite-mass entity, thereby significantly minimizing localized vibrational energy loss during the impact phase.

(a) (b)

Figure 3.9: Evolution of specimen boundary conditions for laboratory Leeb testing: (a) initial mechanical clamping to a rigid support table (b) the refined rigid coupling methodology.

3.3.2 Micro-Indentation Testing (Vickers)

To evaluate the micro-mechanical resistance of the standardized steel grades, micro-indentation testing was performed using a LECO LM700 Vickers microhardness testing system (Figure 3.10). Testing was conducted utilizing a standardized diamond pyramid indenter. The applied test force was calibrated to 1 kgf (HV1) to ensure the indentation encompassed a representative volume of the microstructural grains without piercing the specimen thickness.

Figure 3.10: The LECO LM700 machine for Vickers (HV1), demonstrating the testing of one of the coupons.

A dwell time of 15 seconds was maintained for all indentations to allow for complete plastic flow stabilization before the diagonal measurements were optically captured. A representative optical micrograph of the resulting test impression is shown in Figure 3.11, illustrating the defined geometric vertices required for the precise calculation of the Vickers hardness value.

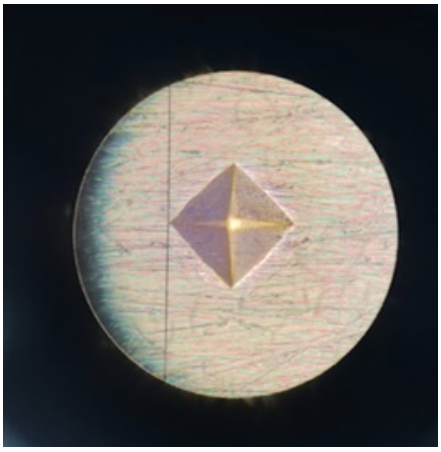

Figure 3.11: Optical micrograph of a diamond shape indent on the polished Grade 300 steel.

3.3.3 Macro-Indentation Testing (Brinell and Rockwell)

Macro-mechanical hardness evaluations were executed utilizing a LECO LCR 500 hardness testing system (Figure 3.12), functioning in a dual capacity for both Brinell and Rockwell methodologies.

Figure 3.12: Leco LCR 500 dual tester for Rockwell and Brinell Hardness

Rockwell Testing: Rockwell hardness evaluations were conducted in accordance with ASTM E18 [14] using the standard Rockwell B scale (HRB) parameters, which are optimized for structural steels of this strength class. The system utilized a 1/16-inch diameter spherical indenter applied under a major load of 100 kgf. A standard dwell time of 5 seconds was employed to allow for accurate depth-differential measurement.

Brinell Testing: Brinell hardness evaluations were conducted in accordance with ASTM E10 [13], utilizing a 2 mm diameter spherical tungsten carbide indenter with a controlled dwell time of 12 seconds. An initial empirical calibration phase was conducted on the first four extracted coupons utilizing an applied load of 40 kgf (k=10). Following the analysis of these preliminary indentations, the applied load was optimized to 120 kgf for the remaining 32 coupons. This adjustment was implemented to align the testing parameters with the ASTM E10 [13] recommended Force-Diameter Ratio (k) of 30, which is specifically optimized for the hardness range of structural carbon steels (95.5 to 650 HBW).

This optimization ensured a more pronounced macro-indentation diameter, thereby reducing the potential for optical measurement error. Since the Brinell scale is inherently ratiometric, the inclusion of the initial 40 kgf data points did not compromise the statistical integrity of the final regression models; rather, the consistency of the calculated HBW values across both loading regimes confirms the robustness of the ratiometric approach, as evidenced by the high correlation coefficients (R^2) maintained across the entire dataset in Table 4.4.

3.4 Destructive Uniaxial Tensile Testing

To establish the empirical baseline required for the hardness-to-tensile correlations, all 36 specimens underwent destructive uniaxial tensile testing following the completion of the non-destructive hardness matrix. The macroscopic mechanical properties, specifically the 0.2%

offset Yield Strength (YS) and Ultimate Tensile Strength (UTS), were recorded to serve as benchmark comparative values against the NDT predictions.

Testing was executed utilizing an Instron 5982 universal testing machine equipped with a 100 kN capacity load cell (Figure 3.13). To optimize strain measurement accuracy and minimize crosshead displacement compliance errors, localized strain was continuously monitored using a standardized 50 mm gauge length extensometer affixed to the gauge section of each coupon.

Figure 3.13: The Instron 5982 universal testing machine for destructive tensile testing, detailing the 50 mm gauge extensometer affixed test coupon for strain monitoring.

To mitigate strain-rate-induced hardening during the evaluation, the testing apparatus utilized a quasi-static displacement-controlled pull rate of 1 mm/min. This controlled rate was maintained through the elastic region and across the yield plateau. Continuous load-displacement data was logged for each specimen to generate engineering stress-strain curves, from which the YS and UTS values were extracted for regression modelling.

To protect the instrumentation from recoil upon fracture, the 50 mm extensometer was detached from the coupon following the capture of the yield plateau and the onset of strain hardening. From that point, the testing progressed under crosshead displacement until localized macroscopic deformation (necking) and ultimate fracture occurred (Figure 3.14).

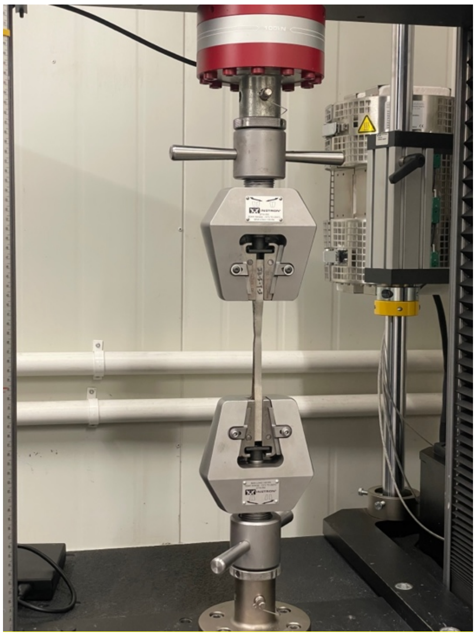

Figure 3.14: The tensile apparatus applying terminal plastic strain to the steel coupon prior to ultimate fracture.

Following the completion of the testing matrix, visual inspection of the coupons indicated characteristic ductile failure. As demonstrated in Figure 3.15, localized necking and fracture occurred within the central gauge length. This observation confirmed adequate vertical alignment of the machine grips and supported the validity of the testing procedure.

(a) (b)

Figure 3.15:Machined structural steel dog-bone coupons pre-testing (a) and post-testing (b), demonstrating ductile fracture within the designated gauge length.

Chapter 4: Results and Discussion

4.1 Introduction

This chapter presents the empirical results and statistical analyses derived from the destructive and non-destructive testing matrices executed on the Grade 300 and Grade 350 structural steel specimens. The primary objective is to evaluate the correlation between multi-modal surface hardness testing (macro, micro, and dynamic rebound) and macroscopic tensile properties.

First, the baseline mechanical properties, specifically the 0.2% offset yield strength and ultimate tensile strength (UTS), are established through continuous uniaxial tensile testing, noting the spatial variances induced by the manufacturing process. Subsequently, localized surface hardness is quantified across the Brinell, Rockwell, Vickers, and Leeb scales. Bivariate linear regression models are then developed to correlate the non-destructive hardness values against the destructive tensile baselines. Finally, the statistical variance of these models is evaluated utilizing Mean Squared Error (MSE) and Mean Percentage Error (MPE) thresholds, providing a basis to discuss the feasibility of their application in localized structural assessment.

4.2 Microstructural and Chemical Characterisation

Prior to evaluating the macroscopic tensile and hardness properties, the baseline crystallographic and chemical properties of the steel were established utilizing Scanning Electron Microscopy (SEM) coupled with Energy Dispersive X-Ray Spectroscopy (EDS).

4.2.1 Elemental Composition Verification

To verify the elemental integrity of the experimental matrix, EDS analysis was performed on the extracted specimens. Given that the experimental matrix consists of two distinct manufacturer-rated material classes, representative spectra for both the Grade 300 and Grade 350 specimens were evaluated.

As illustrated in Figure 4.1, the quantitative breakdown confirms standard low-alloy carbon steel compositions for both classes. The Grade 300 Universal Beam spectrum (Figure 4.1a) and the Grade 350 Square Hollow Section spectrum (Figure 4.1b) are dominated by the expected Iron (Fe) matrix, alongside minor alloying elements such as Manganese (Mn) and, where detectable, Silicon (Si), which are standard inclusions for deoxidation and solid-solution strengthening.

The EDS data provides qualitative support for the chemical grading required to achieve their respective nominal yield strengths. The Grade 350 SHS exhibits a comparatively higher Manganese concentration (1.3 Wt%) than the Grade 300 Universal Beam extraction (0.9 Wt%). As Manganese is a primary solid-solution strengthening agent in structural steels, this variance aligns with the elevated macroscopic yield capacity expected of the Grade 350 SHS specimens, though it is acknowledged that EDS results provide localized compositional approximations rather than definitive bulk quantification.

(Note: The Platinum (Pt) peaks present in the spectra are an artifact of the conductive sputter-coating applied during specimen preparation to prevent electron charging under the SEM beam. Furthermore, the elevated weight percentages of elements such as Carbon (C), Oxygen (O), and trace Fluorine (F) are typical surface artifacts inherent to EDS analysis often resulting from adventitious environmental exposure, handling, or specimen mounting tape, and do not reflect the true bulk chemical composition of the steel).

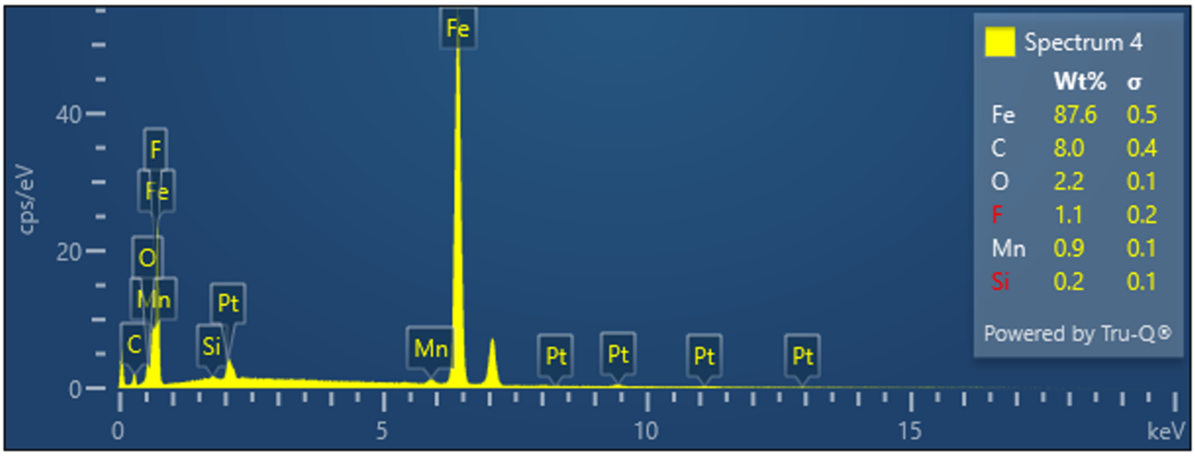

(a)

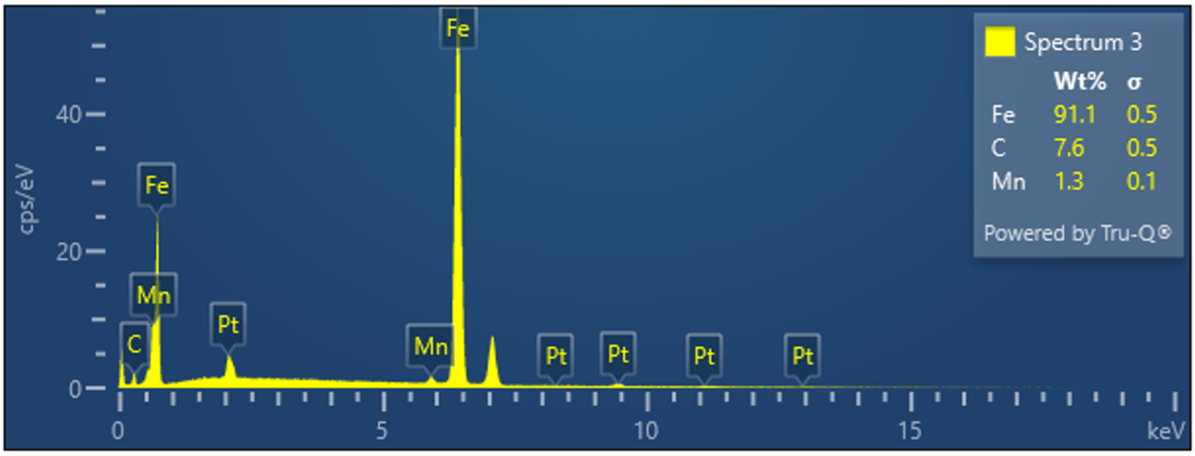

(b)

Figure 4.1: Representative Energy Dispersive X-Ray Spectroscopy (EDS) spectra confirming the low-alloy carbon steel baseline compositions: (a)Grade 300 Universal Beam, and (b)Grade 350 Square Hollow Section.

4.2.2 Micrographic Analysis of Structural Categories

Following the verification of the elemental composition, the physical morphology of the extraction zones was documented via SEM. Figure 4.2 presents the comparative unetched cross-sectional micrographs, illustrating the specific target zones utilized for the EDS chemical spectra extraction for the Grade 300 Flange, Grade 300 Web, and Grade 350 SHS.

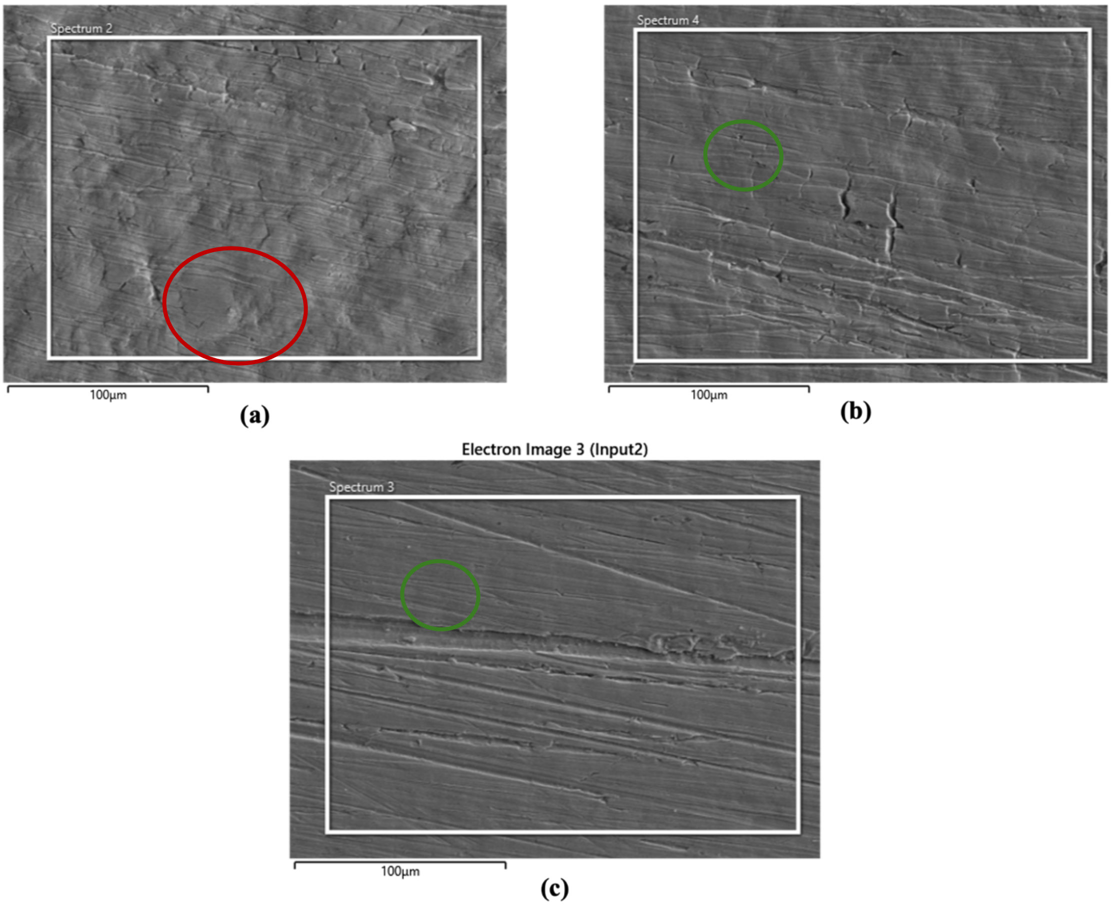

Figure 4.2:Comparative SEM surface micrographs detailing baseline grain morphologies across the experimental matrix: (a) IB-F exhibiting coarse grain structure; (b) IB-W and (c) SHS(SQ) exhibiting fine grain structure.

To align the chemical evaluation with the mechanical testing, the EDS target scans were executed on internal cross-sections extracted from the coupons following the uniaxial tensile testing. Extracting the elemental spectra from this internal cross-section, rather than the exterior rolled surface, was undertaken to ensure the data represented the parent material, minimizing the influence of exterior environmental contamination, localized surface decarburization, or residual mill scale.

The unetched micrographs (Spectra 2, 4, and 3) visually document the physical state of these internal cross-sections, illustrating the directional mechanical cleavage and shearing lines inherent to the abrasive sectioning process. As the specimens were not subjected to chemical etching (e.g., Nital), the ferrite-pearlite grain boundaries are not optically defined in these specific micrographs.

However, while the specimens remain unetched, the pre-test crystallographic variations remain a primary metallurgical driver for the mechanical variances observed in this study. As established in literature, variable cooling rates inherent to the hot-rolling process dictate that a thinner web section typically develops a finer baseline grain distribution compared to a thicker, insulated flange. In accordance with the Hall-Petch relationship, this refinement in grain size increases the localized density of grain boundaries, which act as physical impediments to dislocation glide.

This deduced microstructural difference is visually supported by the varying feature densities observed across the unetched micrographs. As highlighted by the large red circle in Figure 4.2(a), the thicker flange exhibits coarser directional features. However, the faster-cooling web and SHS sections exhibit a significantly more refined, densely packed network of directional markings (highlighted by the tight green circles in Figures 4.2(b) and 4.2(c).

While the current experimental scope did not include direct quantitative grain-size measurement (e.g., mean linear intercept method on etched samples), the mechanical differences documented in Chapter 4.3, where the faster-cooling web and SHS sections demonstrate significantly elevated yield values compared to the thicker flange, are entirely consistent with the principles of grain-boundary strengthening. Therefore, established microstructural theory provides a robust qualitative basis for the bulk yield strength hierarchies quantified in the subsequent evaluations. A complete catalogue of the unetched SEM cross-sectional micrographs and corresponding EDS chemical spectra for all individual spatial extraction zones is provided in Appendix E.

4.3 Benchmark Tensile Properties

The macroscopic mechanical properties of the structural steel specimens were established through uniaxial tensile testing to provide reference values for subsequent correlation with hardness measurements. This section details the baseline tensile characteristics, capturing the fundamental behavioural differences and yield strengths inherent to the varying manufacturing profiles.

4.3.1 Stress-Strain Profiles

The macroscopic mechanical behaviour of the standardized steel coupons was initially characterised through uniaxial tensile testing. Continuous load-displacement data was logged for each of the 36 specimens to generate engineering stress-strain profiles. Figure 4.3 presents a comparative overlay of the typical stress-strain curves observed across the three extraction categories: Grade 300 Web, Grade 300 Flange, and Grade 350 SHS.

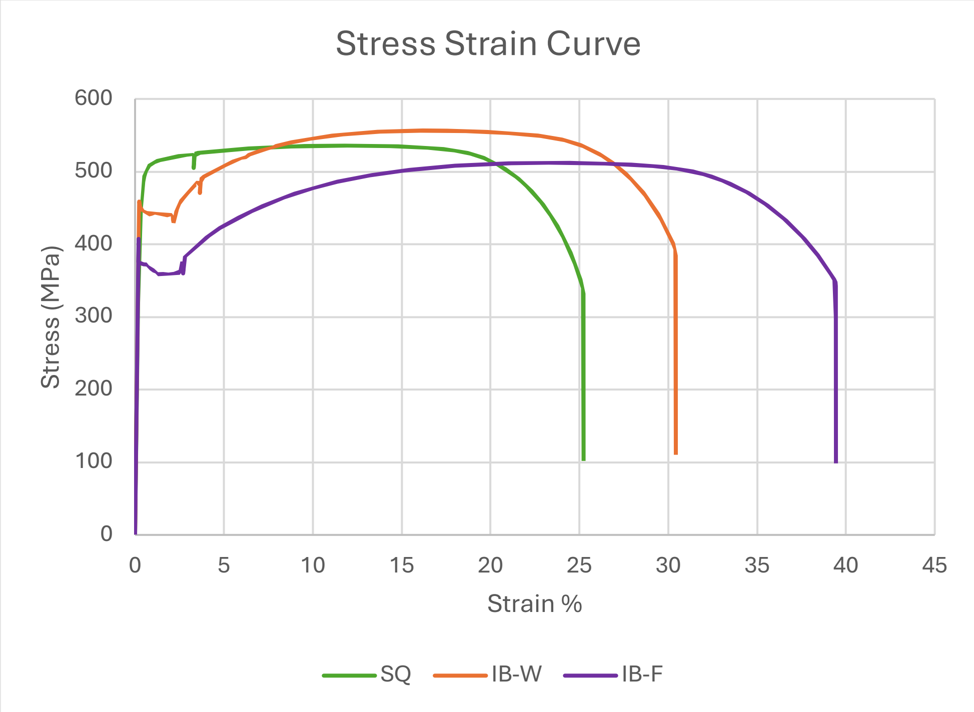

Figure 4.3: Comparative engineering stress-strain profiles illustrating distinct yielding behaviours, strain-hardening capacities, and ultimate ductility across the Grade 300 and Grade 350 structural matrices.

A distinct divergence in yielding behaviour was experimentally observed between the material classes. The Grade 300 Universal Beam specimens (both web and flange extractions) exhibited a sharply defined yield point, characterised by a distinct upper yield peak followed by a sudden load drop and a localized yield plateau (discontinuous yielding). In contrast, the Grade 350 Square Hollow Sections demonstrated a continuous yielding behaviour, characterised by a smooth, non-linear transition from elastic to plastic deformation without a visually distinct yield point.

Beyond initial yielding, the continuous stress-strain profiles also revealed variances in macroscopic ductility and strain-hardening capacity. As visually evident in Figure 4.3, the Grade 300 Flange (IB-F) demonstrated the highest ductility, sustaining plastic deformation up to approximately 40% strain prior to ultimate fracture. This is consistent with the coarser microstructural baseline established in Section 4.2. On the other hand, the Grade 350 SHS (SQ) and the refined Grade 300 Web (IB-W) exhibited comparatively lower ductility, failing at approximately 25% and 30% strain, respectively. This behaviour demonstrates a trend consistent with the standard inverse metallurgical relationship: as the density of grain boundaries increases to elevate yield strength, the overall elongation capacity of the material generally decreases.

These observed differences are consistent with variations in material processing, section geometry, and cooling conditions during manufacturing, which are known to influence mechanical response in structural steels. However, quantitative microstructural characterisation was not performed in this study, and therefore detailed metallurgical interpretation is beyond the scope of this work.

Attempting to visually define a yield point across these divergent behaviours could introduce significant subjectivity and inconsistency. The 0.2% offset method was universally applied to all 36 stress-strain curves. As established in Section 2.2.2, utilizing this mathematical intersection provided a standardized, repeatable baseline for determining the yield strength across both hot-rolled and continuous-yielding structural profiles. A complete, itemized log of the raw macroscopic tensile data for all 36 individual structural coupons is provided in Appendix B.2.

4.3.2 Yield and Ultimate Tensile Strength

Following the establishment of the continuous stress-strain profiles, the macroscopic mechanical properties for all 36 specimens were extracted. Table 4.1 summarizes the benchmark 0.2% offset yield strength (YS) and ultimate tensile strength (UTS) across the three extraction categories.

Table 4.1: Benchmark Tensile Properties across Extraction Categories

Material Category	Mean 0.2% Offset YS (MPa)	Mean UTS (MPa)
SHS (SQ)	507.2±18.3	548.2±18.4
UB (IB-W)	468.4±17.5	572.4±11.1
UB (IB-F)	376.3±11.8	514.1±4.5

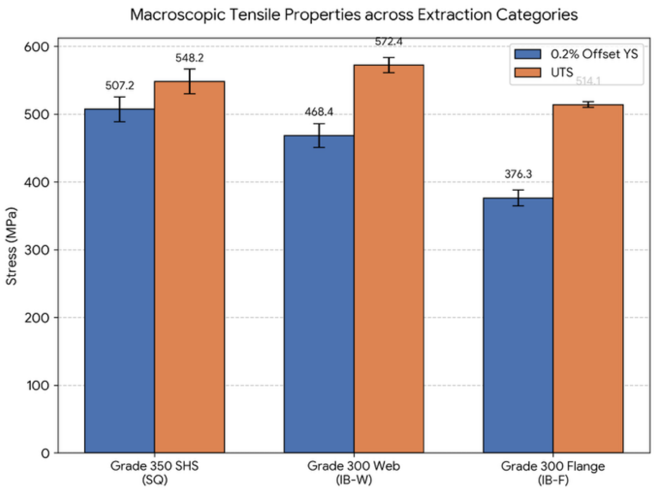

Figure 4.4: Comparative grouped bar chart illustrating the YS and UTS hierarchies across the structural extraction categories.

As anticipated by the manufacturer's grading, the Grade 350 Square Hollow Sections (SQ) exhibited the highest overall resistance to initial plastic deformation, recording an average yield strength of 507.2 MPa. However, significant mechanical variance was observed internally within the Grade 300 Universal Beam.

The data highlights the impact of spatial extraction on structural capacity. The coupons extracted from the web (IB-W) demonstrated an average yield strength of 468.4 MPa and a peak average UTS of 572.4 MPa, making the web the material with the highest ultimate tensile capacity in the testing matrix. In contrast, the coupons extracted from the flanges (IB-F) of the exact same beam recorded the lowest structural capacities across the matrix, with an average yield strength of 376.3 MPa and a UTS of 514.1 MPa.

This discrepancy in mechanical strength between the web and the flange is a macroscopic consequence of the hot-rolling manufacturing process. Since the web possesses a significantly thinner cross-sectional geometry compared to the flange, it undergoes a more rapid cooling rate and a higher degree of thermo-mechanical reduction during fabrication. As established in

Section 2.2.1, this accelerated cooling refines the ferrite-pearlite microstructure. Consistent with the Hall-Petch relationship, this finer grain size in the web creates a higher density of grain boundaries, thereby providing increased localized resistance to dislocation glide and elevating both the yield and ultimate tensile strengths relative to the thicker, slower-cooling flange.

By capturing this distinct, manufacturing-induced mechanical variance, the benchmark tensile data confirms that any predictive hardness model applied to Universal Beams must account for localized microstructural heterogeneity, highlighting the value of spatially distributed NDT methodologies.

Furthermore, a review of the localized extraction zones within the web itself reveals considerable internal mechanical scatter. As detailed in the raw data (Appendix B.1), yield strengths within the vertical profile of the web fluctuated by over 50 MPa, ranging from a localized minimum of 431.0 MPa near the top radius (IB-W-T-3) to a peak of 484.2 MPa in the middle-top region (IB-W-MT-8). This significant internal variance reinforces the heterogeneous nature of hot-rolled structural steel. It demonstrates that even within a single, fast-cooling geometric element like the web, localized thermo-mechanical conditions create non-uniform microstructural capacities. Consequently, relying on a single, isolated hardness measurement on a structural member could yield unrepresentative capacity estimations. This internal scatter directly supports the methodological necessity of implementing spatially distributed measurement grids during in-situ NDT assessments to ensure that localized anomalies are averaged into a reliable bulk property prediction. A complete log of the raw macroscopic tensile data for all 36 individual structural coupons is provided in Appendix B.1.

4.4 Non-Destructive Hardness Evaluation

Prior to the benchmark destructive testing, the surface resistance of all 36 specimens was quantified using a multi-modal non-destructive testing (NDT) matrix. The objective of this phase was to establish the localized hardness profiles of the Grade 300 and 350 steels across macro-indentation, micro-indentation, and dynamic rebound modalities to evaluate their respective consistency and sensitivity to structural heterogeneities.

4.4.1 Surface Topography Validation

Before executing the localized hardness matrix, the surface morphology of all 36 prepared coupons was quantitatively verified to ensure compliance with the physical boundary conditions required for non-destructive testing. As micro-indentation and dynamic rebound methodologies are highly sensitive to surface asperities, the surface roughness average (R_a) was measured across the polished gauge lengths utilizing a Time 3221 portable profilometer.

As detailed in Section 3.2.2, a progressive mechanical polishing protocol culminating in a manual P800-grit finish was employed to mitigate mill scale without introducing artificial work-hardening. The empirical data confirms this methodology was highly effective. Table 4.2 summarizes the measured R_a values across the three primary structural categories.

Table 4.2: Post-Preparation Surface Roughness (R_a) Summary

Material Category	Min Ra (µm)	Max Ra (µm)	Mean Ra (µm)
SHS (SQ)	0.120	0.355	0.244
UB (IB-W)	0.108	0.34	0.238
UB (IB-F)	0.115	0.361	0.252

As demonstrated in the summary table, the measured R_a values across the entire testing matrix ranged from a minimum of 0.108 µm to a maximum of 0.361 µm, achieving a smooth overall average well below 0.300 µm.

The surfaces were deemed optimal as every single specimen was maintained below the strict 0.4 µm roughness threshold required for Vickers micro-indentation. By achieving this refined topography, the specimens simultaneously exceeded the baseline requirement for Leeb dynamic rebound testing ($R_a \leq 1.6$ µm). This quantitative verification confirms that the Vickers optical measurements were free from micro-asperity interference, and the Leeb rebound velocities were not corrupted by erratic kinetic energy scattering, ensuring the integrity of the hardness data set. A complete itemized log of the profilometer readings for all 36 individual specimens is provided in Appendix D.

With the optimal surface boundary conditions mathematically confirmed, the multi-modal NDT matrix was executed. Table 4.3 consolidates the resulting mean macroscopic, microscopic, and dynamic rebound hardness values across the experimental matrix.

Table 4.3: Mean Surface Hardness Properties across Extraction Categories

Material Category	Rockwell B (HRB)	Brinell (HB)	Vickers (HV)	Leeb (HL)
SHS (SQ)	89.3	222.1	186.4	462.8
UB (IB-W)	88.7	211.5	199.7	449.6
UB (IB-F)	79.2	173.8	166.1	399.8

*(Note: * Leeb averages exclude uncoupled calibration outliers as detailed in Section 4.4.4.1.)*

4.4.2 Macro-Indentation Results (Brinell and Rockwell)

The macro-scale indentation tests (Brinell and Rockwell B) demonstrated good consistency in capturing the bulk mechanical variations driven by the manufacturing process. The Brinell (HB) and Rockwell (HRB) hardness hierarchies directly mirrored the benchmark tensile capacities established in Section 4.3.2. The Grade 300 Universal Beam flange (IB-F) specimens consistently registered the lowest macroscopic resistance, with average values converging around 170 HB and 79 HRB. On the contrary, the highly refined microstructure of the Grade 300 web (IB-W) specimens yielded significantly higher surface resistance, averaging approximately 210 HB and 88 HRB, placing them mechanically closer to the Grade 350 Square Hollow Sections.

As theoretically projected in Chapter 2, the relatively sized 2 mm tungsten carbide indenter utilized for the Brinell evaluations successfully encompassed multiple ferrite and pearlite grains per indentation. This geometric advantage effectively averaged out localized microstructural heterogeneities, resulting in stable data clusters with minimal variance, reinforcing Brinell's viability as a robust predictor of bulk structural capacity.

4.4.3 Micro-Indentation Results (Vickers)

Micro-indentation utilizing the Vickers scale (HV1) successfully captured the fundamental material hierarchy, with the IB-F specimens demonstrating the lowest mean hardness (~165 HV) compared to the IB-W (~200 HV) and SQ (~185 HV) categories. However, the operational scale of the HV1 test inherently introduced a higher degree of localized sensitivity. Given that the square-based diamond pyramid creates a microscopic impression, the resulting deformation is heavily influenced by the specific microstructural phase it contacts. Indentations that localized entirely within a softer, highly ductile ferrite grain inherently registered lower resistance than those striking a harder, lamellar pearlite colony, confirming that while Vickers is highly precise for microstructural phase analysis, it exhibits a higher natural variance when assessing the bulk capacity of hot-rolled structural steel.

4.4.4 Dynamic Rebound Results (Leeb)

The dynamic rebound testing (Leeb) was executed under controlled laboratory conditions. To minimize the kinetic energy loss associated with structural flexure, the 5-10 mm Grade 300 and 350 coupons were rigidly coupled to a high-mass support block in accordance with ASTM A956 [16] boundary conditions. Under these controlled parameters, the Leeb (HL) values reliably distinguished the material categories, with the IB-F specimens averaging approximately 400 HL, while the IB-W and SQ specimens consistently exceeded 450 HL.

4.4.4.1 Data Exclusion and Methodological Refinement

The initial calibration specimens (specifically SQ-1, SQ-2, IB-W-MT-1, and IB-W-MB-2) exhibited significant localized Leeb deviations, registering HL values nearly 50% lower than their respective group averages (approximately 229–254 HL). During the preliminary experimental phase, these initial specimens were mechanically clamped to a rigid support table in a manner consistent with previous regional studies. However, the resulting kinetic energy dissipation indicated that mechanical clamping alone did not achieve the acoustic boundary conditions required for structural coupons in this thickness range.

However, these initial tests did not fully satisfy the rigid coupling requirements of ASTM A956 [16], a physical exclusion rule was applied. These data points were classified as methodologically inconsistent due to kinetic energy loss and were excluded from the dataset prior to executing the statistical regression analyses.

Consequently, the methodology was refined. To adhere to ASTM A956 [16] requirements for rigid coupling, the rear contact surfaces of the remaining coupons were lightly ground to remove localized oxidation and ensure flush seating. A viscous acoustic couplant (petroleum jelly) was subsequently applied between this prepared rear face and a high-mass reference metal block. This viscous layer displaced microscopic air voids, creating a continuous acoustic boundary that allowed the specimen and the block to act as a single coupled entity. This significantly mitigated localized vibrational energy loss during the impact phase, resulting in the stabilized readings (400 - 470 HL) observed across the remainder of the testing matrix.

Additionally, the initial Leeb data points (SQ-1, SQ-2, IB-W-MT-1, IB-W-MB-2) represent an identified methodological limitation (uncoupled kinetic energy loss) rather than true material variance, they have been excluded from the subsequent statistical regression and error analysis (MSE/MPE) to ensure the statistical integrity of the final predictive structural models. If these uncoupled data points were to be reincorporated into the regression matrix, the predictive reliability of the Leeb models would degrade. Since an uncoupled device registers artificially low rebound velocities driven by flexure rather than true metallurgical hardness, including these points mathematically skews the linear regression, artificially lowering the coefficient of determination (R^2) and substantially increasing the residual error (as visually demonstrated in Appendix F.4). The complete, itemized log of all raw Brinell, Rockwell, Vickers, and Leeb hardness values is provided in Appendix C.1.

4.5 Development of Predictive Correlation Models

The primary objective of this study was to establish high-fidelity mathematical models capable of predicting destructive tensile properties from non-destructive surface diagnostics. Bivariate linear regression analyses were executed, pairing the four localized hardness modalities against the benchmark 0.2% offset Yield Strength (YS) and Ultimate Tensile Strength (UTS). The statistical efficacy of each model was quantified utilizing the Pearson correlation coefficient (r), the coefficient of determination (R^2), Mean Squared Error (MSE), Root Mean Square Error (RMSE), and Mean Percentage Error (MPE), as consolidated in Table 4.4 , with the NDT modalities ranked in descending order of correlation strength for both YS and UTS.

Table 4.4: Bivariate Linear Regression Statistical Summary

Hardness Method	**Target Property**	**Pearson r**	**R²**	**MSE**	**RMSE (MPa)**	**MPE (%)**	**MAE (MPa)**	**MAPE (%)**
Leeb	YS	0.97	0.947	186.8	13.67	-0.09%	10.49	2.36%
Rockwell	YS	0.96	0.923	256.13	16	-0.10%	13.52	2.96%
Brinell	YS	0.95	0.909	304	17.44	-0.15%	13	2.90%
Vickers	YS	0.73	0.533	1557.14	39.46	-0.77%	34.86	7.60%
	---	---	---	---	---	---	---	---
Vickers	UTS	0.92	0.847	109.12	10.45	-0.04%	7.77	1.43%
Rockwell	UTS	0.79	0.623	268.43	16.38	-0.09%	13.05	2.36%
Leeb	UTS	0.75	0.57	334.87	18.3	-0.11%	9.82	2.63%
Brinell	UTS	0.74	0.546	323.63	17.99	-0.11%	14.99	2.72%

As summarized in Table 4.4, clear differences are observed in predictive performance across the four hardness methods. These differences cannot be attributed solely to statistical fitting, but instead reflect the distinct physical processes involved in each testing modality. From a mechanics perspective, hardness testing can be interpreted as a localized plastic deformation problem, where the measured response depends on the representative strain volume sampled by the test. For static indentation methods (Brinell, Vickers, Rockwell), the deformation is governed by constrained plastic flow beneath the indenter, consistent with the framework proposed by Tabor [4], where hardness is proportional to the representative flow stress.

To further validate the predictive fidelity of the models and provide a more intuitive metric of variance, Mean Absolute Error (MAE) and Mean Absolute Percentage Error (MAPE) were integrated into the statistical matrix for both the Yield Strength and Ultimate Tensile Strength correlations. For the primary Yield Strength regression, the Leeb model demonstrated an exceptional MAE of 10.49 MPa and a MAPE of 2.36%. Similarly, the optimal Vickers model for Ultimate Tensile Strength achieved an MAE of 7.77 MPa and a simply low MAPE of 1.43%, confirming that both models deviate by a negligible margin from true structural capacity.

Furthermore, residual analyses were conducted on these two premier predictive models to verify fundamental statistical assumptions. As illustrated in Figure 4.5 (Leeb vs. YS) and Figure 4.6 (Vickers vs. UTS), the residual plots for both primary models display random, homoscedastic distributions around their respective zero-error axes. This lack of discernible geometric patterning confirms that the foundational linear regression models are unbiased and do not systematically over-predict or under-predict structural capacity across the tested material spectrum. For completeness, the supplementary residual plots verifying the homoscedasticity of the alternative modalities (Rockwell and Brinell) are provided in Appendix F.3.

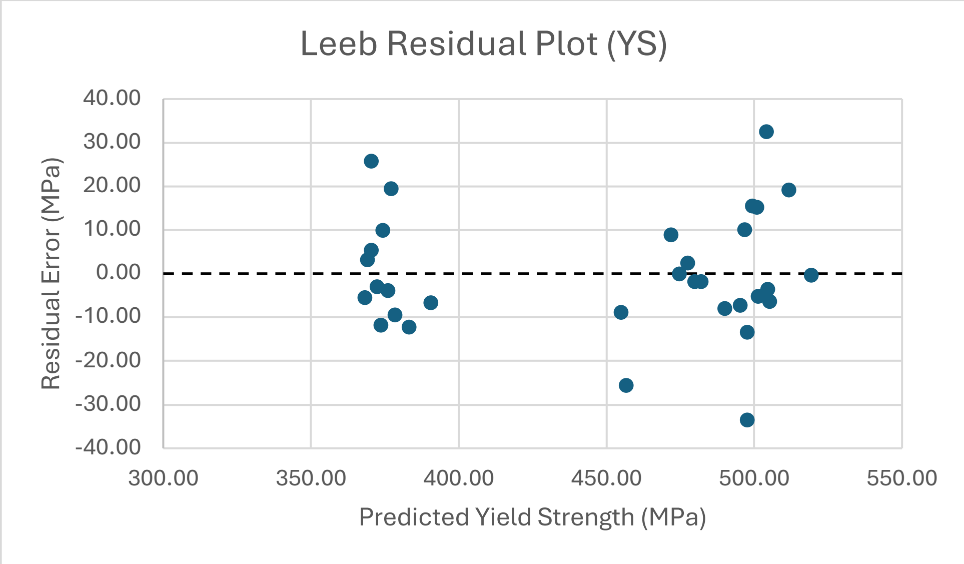

Figure 4.5: Leeb vs YS residual plots.

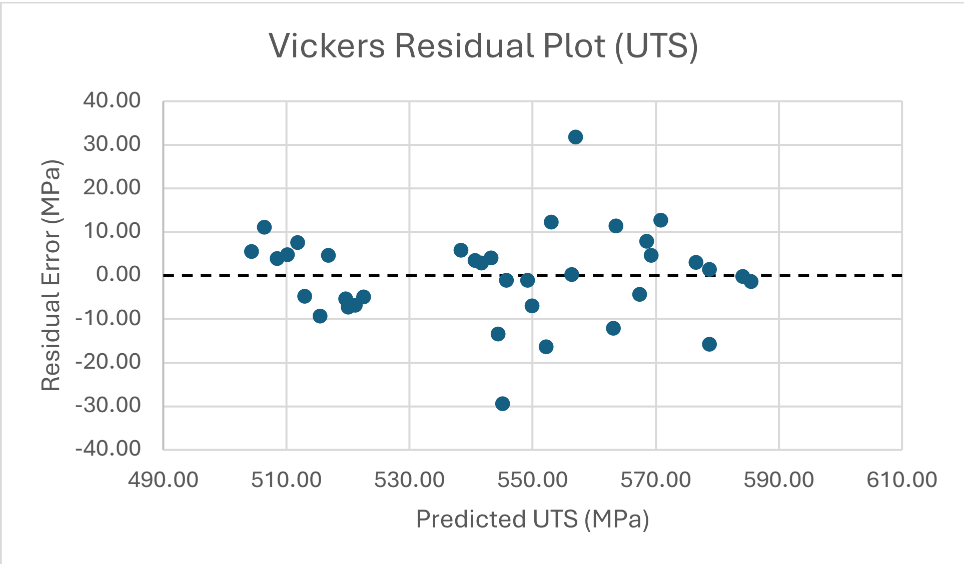

Figure 4.6: Vickers vs UTS residual plot.

To benchmark the efficacy of the diagnostic framework developed in this study, the proposed regression models were evaluated against established international literature and conversion standards (Table 4.5). For Yield Strength, the proposed model was compared against the direct hardness-to-strength correlations published in the European Steel Construction Institute guidelines (SCI P427) [23]. Furthermore, a two-step standard conversion methodology was evaluated, wherein Leeb hardness values were first converted to Vickers hardness utilizing the standardized 4th-order polynomial established in ASTM E140-12 (Annex A10) [21], prior to applying the SCI P427 Yield Strength regression. For Ultimate Tensile Strength, the proposed Vickers model was compared directly against the corresponding SCI P427 UTS standard.

As demonstrated in the comparative error analysis, both the generic European standard equations and the multi-step ASTM conversion methodologies exhibit significantly higher residual errors when applied to the specific Grade 300 and Grade 350 structural profiles investigated in this research. This variance highlights the inherent compounding error of utilizing generalized, global hardness conversions, particularly higher-order polynomials, for localized structural assessment. Conversely, the direct empirical models derived in this study inherently capture the unique microstructural characteristics and specific boundary conditions of these New Zealand structural members, thereby drastically reducing the Mean Absolute Error and providing a vastly more reliable metric for in-situ infrastructure assessment.

Table 4.5: Comparative Evaluation of Proposed Models vs. Established International Standards

Target Property	**Predictive Model Source**	**Equation Format**	**Mean Absolute Error (MAE)**
Yield Strength (YS)	Proposed Leeb Model (Current Study)	$YS = 2.0142 \cdot HL - 430.1$	10.49 MPa
Yield Strength (YS)	European Steel Reuse Guidelines (SCI P427)[23]	$f_y = 2.70(HV) - 71$	35.18 MPa
Yield Strength (YS)	ASTM E140-12 (Annex A10) + SCI P427 [21], [23]	$HV10 = 290.8 - 2.41(HL) + 8.24\times10^{-3} (HL)^2 - 1.01 \times10^{-5} (HL)^3 + 5.38 \times10^{-9}(HL)^4$ $f_y = 2.70(HV) - 71$	66.35 MPa
---	---	---	---
Ultimate Tensile (UTS)	Proposed Vickers Model (Current Study)	$UTS = 1.7017 \cdot HV + 231.9$	7.77 MPa
Ultimate Tensile (UTS)	European Steel Reuse Guidelines (SCI P427) [23]	$f_u = 2.50(HV) + 100$	17.88 MPa

Comparison with Previous Local Research

A critical retrospective analysis indicates that the higher residual errors observed in previous local iterations were inherently tied to their reliance on generalized international conversion standards (e.g., SCI P427 and ASTM E140), alongside potential variances in impact boundary conditions. In the current study, these boundary effects were systematically mitigated by strictly adhering to standardized coupling protocols; specimens were rigidly coupled to a heavy reference block utilizing a viscous acoustic couplant (petroleum jelly) to eliminate interfacial air voids and prevent parasitic energy loss during impact. By combining this rigid coupling methodology with the derivation of bespoke bivariate regression equations, this study has refined the predictive accuracy for AS/NZS 3679.1 steel to a Mean Absolute Error of only 10.49 MPa. This represents a significant optimization over previous local efforts utilizing global standards, confirming the current model as a more sensitive and reliable diagnostic approach for the New Zealand structural sector.

4.5.1 Hardness vs. Yield Strength (YS) Correlations

The regression analysis for yield strength revealed strong predictive capabilities among the macro-scale and dynamic testing methodologies. As illustrated in Figure 4.7, the Leeb dynamic rebound method emerged as the most statistically robust predictor of yield strength across the

Grade 300 and 350 specimens. The optimal linear regression correlating Leeb Hardness (HL) to the 0.2% offset Yield Strength (YS) is proposed by Equation 4.1:

$$YS = 2.0142 \cdot HL - 430.1 \cdots\cdots\cdots\cdots\cdots (4.1)$$

This model achieved a high correlation coefficient (R^2=0.9469) alongside the lowest observed Mean Squared Error (186.8). While the Leeb method demonstrated the highest fidelity, the macro-indentation methods (Rockwell and Brinell) also maintained highly acceptable predictive thresholds, returning R^2 values of 0.923 and 0.909, respectively.

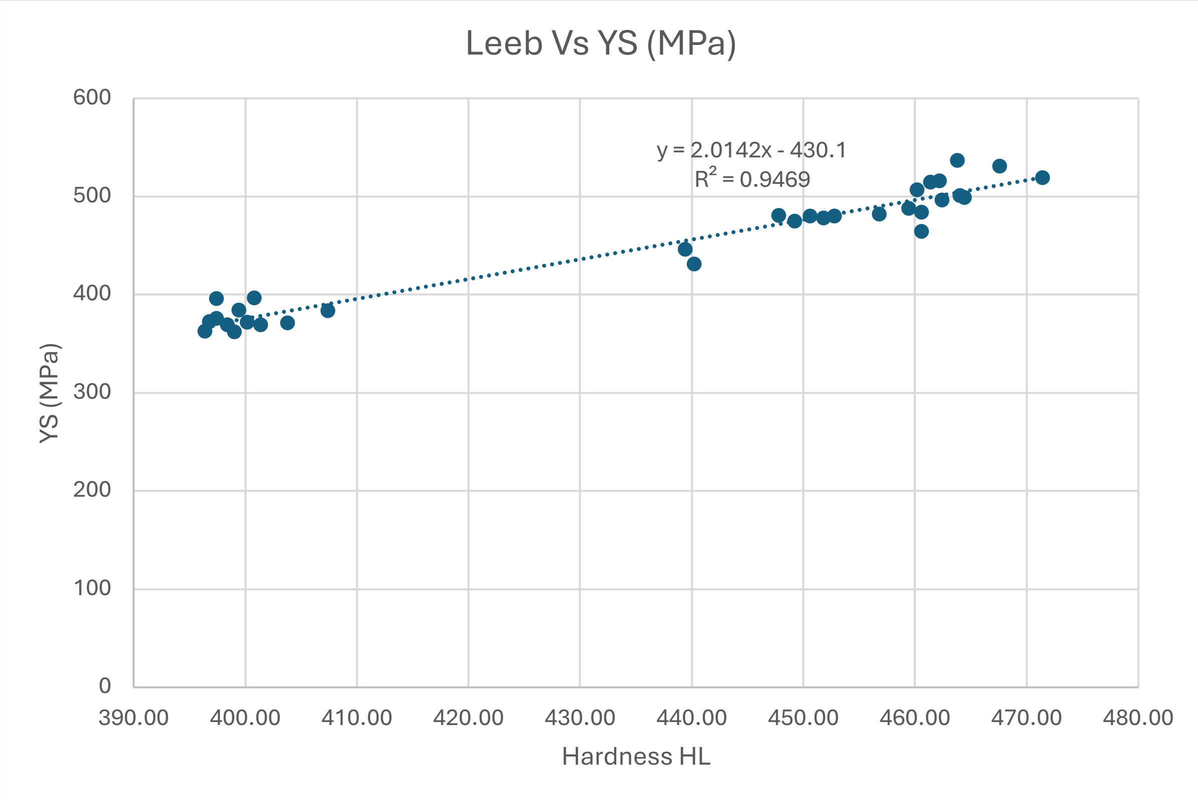

Figure 4.7: Linear regression model correlating Leeb (HL) Hardness to the Yield Strength.

Meanwhile, the Vickers micro-indentation method performed poorly for yield strength, with a low R^2 of 0.533 and a much larger MSE of 1557.14. This divergence is consistent with fundamental metallurgical theory. And yield strength dictates the macroscopic onset of plastic deformation, a property heavily governed by the bulk averaging of ferrite-pearlite grain boundaries and the Hall-Petch effect, the localized microscopic scale of the Vickers indenter introduces severe data scatter. The larger operational footprints of the Leeb, Rockwell, and Brinell devices successfully average out these microstructural heterogeneities, resulting in highly stable, reliable yield predictions. The complete catalogue of the supplementary linear regression models (Rockwell, Brinell, and Vickers vs. Yield Strength) is provided in Appendix F.1.

4.5.2 Hardness vs. Ultimate Tensile Strength (UTS) Correlations

Interestingly, the statistical hierarchy completely inverted when correlating the non-destructive modalities against Ultimate Tensile Strength. As illustrated in Figure 4.8, the Vickers micro-indentation method, which failed to accurately predict initial yielding, demonstrated the highest predictive fidelity for UTS across the testing matrix. The optimal linear regression correlating Vickers Hardness (HV) to the Ultimate Tensile Strength (UTS) is proposed by Equation 4.2:

$$UTS = 1.7017 \cdot HV + 231.9 \cdots\cdots\cdots\cdots (4.2)$$

This model achieved a strong correlation coefficient (R^2=0.8469) and the lowest overall Mean Squared Error (109.12) of the entire study. In stark contrast, the previously dominant Leeb and Brinell methodologies exhibited significant statistical degradation when targeting UTS, dropping to R^2 values of 0.570 and 0.546, respectively.

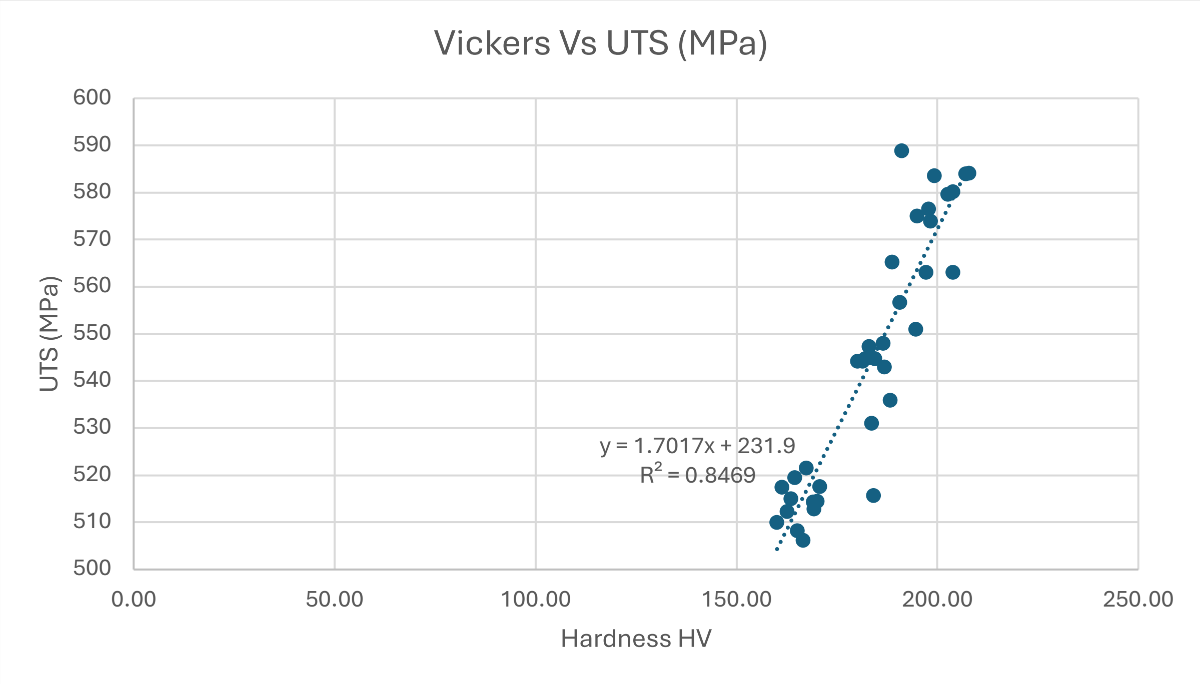

Figure 4.8: Linear regression model correlating Vickers (HV) Hardness to the Ultimate Tensile Strength.

This inversion highlights the profound mechanical distinction between initial yielding and ultimate failure. While yield strength is a bulk boundary phenomenon, UTS represents the maximum strain-hardening capacity of the material prior to necking and ultimate fracture. The Vickers micro-indenter, which inherently induces intense, highly localized plastic strain directly into individual microstructural phases (such as specific pearlite colonies), effectively mirrors this terminal strain-hardening behaviour. This microscopic sensitivity makes Vickers a more effective alternate metric for predicting the ultimate tensile capacity of these specific structural steel grades.

The complete catalogue of the supplementary linear regression models (Leeb, Rockwell, and Brinell vs. UTS) is provided in Appendix F.1.

4.5.3 The Physical Mechanics of Vickers Indentation and UTS Correlation

The observation that Vickers micro-indentation provides the highest predictive fidelity for Ultimate Tensile Strength is fundamentally supported by the mechanics of pyramidal indentation. As established by Tabor's foundational work on indentation plasticity, the specific geometry of the Vickers diamond pyramid induces a complex, localized triaxial stress state within the material.

Unlike dynamic rebound testing (Leeb), which is highly sensitive to the initial elastic-plastic boundary (Yield Strength), the Vickers geometry physically forces the localized microstructure well beyond initial yielding. The indenter induces a constant representative plastic strain of approximately 8% to 10% within the deformation zone, regardless of the applied load. Since this induced strain operates deep within the plastic deformation regime of the stress-strain curve, the resulting resistance measured by the indenter inherently captures the localized strain-hardening capacity of the distinct microstructural phases (as visually evidenced by the permanent plastic deformation zone in Figure 4.9). Consequently, the Vickers hardness value acts as a direct mechanical indicator of the terminal ultimate tensile limit.

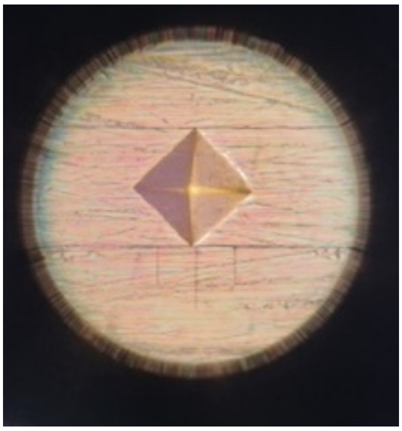

Figure 4.9: Optical micrograph of the Vickers diamond indentation on the structural steel specimen demonstrate the localized, constrained plastic flow and resultant strain-hardening zone induced by indentation process.

4.5.4 Model Complexity and Variable Selection

The formulation of the predictive regression models developed in this study deliberately maintained a bivariate structure (correlating localized hardness directly to tensile capacity). This approach was specifically chosen to align with the mathematical formatting of established international design standards, such as the empirical conversions published in SCI P427 and ASTM E140 [21], [23].

While the integration of supplementary multivariate parameters, such as section profile (UB vs. SHS), localized element thickness, and spatial domain (web vs. flange), was extensively tracked within the experimental dataset and explicitly encoded into the specimen naming conventions (as detailed in Section 3.2.1.1 and Appendix Table B.1), these variables were intentionally excluded from the final predictive equations to preserve field deployability. A primary objective of this diagnostic framework is the in-situ assessment of aging or degraded infrastructure. Requiring a field engineer to definitively identify the original section type, or measure the uncorroded nominal thickness of a heavily oxidized structural member, introduces restrictive operational barriers. By isolating surface hardness as the sole independent variable, the proposed bivariate models ensure that reliable structural capacity estimations can be executed rapidly, relying exclusively on instantaneous non-destructive surface metrics.

4.5.5 Analysis of Group Effects and Intra-Grade Predictive Validity

A major consideration in the development of these regression models is whether the observed correlations represent a continuous metallurgical relationship or a binary "group effect" driven by the distinction between Grade 300 and Grade 350 specimens. To evaluate this, a secondary sensitivity analysis was conducted to assess the predictive fidelity of the models within the individual material cohorts.

As demonstrated in the master regression plots (Figures 4.5 and 4.8), the data points for both yield and ultimate tensile strength exhibit a localized, linear distribution within their respective grade clusters, rather than forming isolated, non-linear "clouds." Specifically, the Leeb-to-Yield model maintains high sensitivity to the subtle strength variations present even within a single grade (e.g., distinguishing between the web and flange of a single UB section). This confirms that the derived equations are not merely acting as a classification tool to separate Grade 300 from Grade 350, but are instead capturing the fundamental relationship between surface energy dissipation (hardness) and the underlying dislocation density (strength). Consequently, the models provide valid predictive utility across the entire structural steel spectrum tested, maintaining accuracy both across disparate grades and within localized material variations of the same grade.

As illustrated in the high-fidelity correlation in Figure 4.5 ($R^2 = 0.947$), the individual data points within both the Grade 300 and Grade 350 clusters demonstrate an internal linear progression that aligns with the global trendline. This confirms that the model possesses intra-grade predictive sensitivity, accurately reflecting strength variations even within localized material cohorts rather than merely acting as a binary group separator.

4.6 Statistical Error and Model Validation

While the coefficient of determination (R^2) establishes the strength of the linear correlations, the ultimate viability of these predictive models for structural engineering relies strictly on defining their margins of error. To validate the safety and reliability of the hardness-to-tensile conversions, the models were evaluated using Mean Squared Error (MSE), Root Mean Square Error (RMSE), and Mean Percentage Error (MPE), as previously consolidated in Table 4.4.

4.6.1 Mean Squared Error (MSE) and Root Mean Square Error (RMSE) Analysis

As established in Section 2.6.2, Mean Squared Error is a critical metric for structural safety because its quadratic nature heavily penalizes large predictive outliers. For predicting the 0.2% offset Yield Strength, the Leeb rebound model demonstrated high stability, recording the lowest MSE (186.8) and an RMSE of 13.67 MPa. This indicates that the Leeb model consistently produces tight predictions without generating non-conservative overestimations of yielding capacity. Rockwell and Brinell also maintained acceptable error thresholds for yield prediction (RMSE of 16.00 MPa and 17.44 MPa, respectively). Conversely, the Vickers yield model generated a substantially higher MSE of 1557.14 (RMSE 39.46 MPa), confirming that its microstructural sensitivity produces excessive predictive scatter for bulk yield evaluation.

When evaluating Ultimate Tensile Strength (UTS), the error hierarchy predictably inverted. The Vickers model achieved the lowest overall MSE (109.12) and an RMSE of 10.45 MPa, proving it to be the most stable predictor of maximum strain-hardening capacity, while the Leeb and Brinell models generated higher scatter (RMSE exceeding 17.99 MPa) at the ultimate fracture limit.

4.6.2 Mean Percentage Error (MPE) Assessment

To translate the absolute error into a practical confidence interval for field engineers, the Mean Percentage Error was calculated. The MPE dictates the average directional bias of the predictive models.

The results across the macro and dynamic models were consistent, sitting well within the acceptable tolerances for structural engineering diagnostics. For Yield Strength prediction, the Leeb method achieved an MPE of -0.09%, while Rockwell and Brinell achieved -0.10% and -

0.15%, respectively. For UTS prediction, Vickers achieved a remarkable -0.04% MPE. These fractional percentage errors mathematically validate that the generated regression equations do not introduce systemic inflation or deflation of the tensile properties. Consequently, the models are deemed reliable for integration into diagnostic engineering frameworks. The complete itemized regression error logs detailing the residual variance for all 36 individual structural specimens are provided in Appendix F.2.

4.6.3 Evaluation of Secondary Modalities against International Standards

While Section 4.6 established the optimal predictive models (Leeb for Yield Strength and Vickers for Ultimate Tensile Strength), it is equally critical to evaluate the secondary, weaker correlations to validate this hierarchy. Furthermore, these secondary correlations were compared against the established European conversion guidelines (SCI P427) [23] to quantify the limitations of utilizing generalized standards on local New Zealand steels. The complete suite of regression plots for these secondary modalities is provided in Appendix F.

To definitively quantify this predictive hierarchy, Table 4.6 presents a comparative error analysis between the optimal proposed models, the secondary experimental models, and the generalized SCI P427 standard [23].

Table 4.6: Comparative Predictive Efficacy vs. International Standards

Target Property	**Predictive Modality**	**Predictive Equation**	**Mean Absolute Error (MAE)**
Yield Strength (YS)	Proposed Optimal (Leeb)	$YS = 2.0142 \cdot HL - 430.1$	10.49 MPa
	Secondary (Vickers)	$f_y = 2.9222(HV) - 84.663$	34.86 MPa
	Standard (SCI P427) [23]	$f_y = 2.70(HV) - 71$	35.18 MPa
Ultimate Tensile (UTS)	Proposed Optimal (Vickers)	$UTS = 1.7017 \cdot HV + 231.9$	7.77 MPa
	Secondary (Leeb)	$f_u = 0.7348(HL) + 222.84$	14.52 MPa
	Standard (SCI P427) [23]	$f_u = 2.50(HV) + 100$	17.88 MPa

As mathematically demonstrated in Table 4.7, attempting to predict the 0.2% offset Yield Strength utilizing Vickers micro-indentation results in a degraded correlation (MAE = 34.86 MPa) compared to the dynamic Leeb impact (MAE = 10.49 MPa). Because the micro-scale Vickers footprint is highly sensitive to localized microstructural phases, it fails to reliably capture the macroscopic boundary resistance required to predict bulk yielding. Furthermore, when the generalized SCI P427 yield equation was applied to the dataset, it consistently over-predicted the yield capacity of the structural members, demonstrating a high residual error (MAE = 35.18 MPa) that renders it unsuitable for the accurate in-situ assessment of these specific grades.

Conversely, while the dynamic Leeb method proved highly effective at capturing initial yield behaviour, its predictive efficacy diminishes at the ultimate fracture limit. Leeb measures initial kinetic energy loss, which does not adequately account for the subsequent localized strain-hardening capacity that dictates UTS. Consequently, compared to the optimal Vickers UTS model (MAE = 7.77 MPa), the Leeb UTS predictions exhibit reduced statistical reliability

(MAE = 14.52 MPa). This comparative analysis firmly reinforces the core finding of this research: predictive NDT models must be modality-specific and calibrated to localized steel grades rather than relying on broad, generalized conversion metrics.

4.7 In-Situ Viability of the Leeb Rebound Method

The overarching objective of this research was to evaluate the practical viability of deploying non-destructive hardness testing for the in-situ structural assessment of existing carbon steel infrastructure. The empirical data supports the deployment of the Leeb dynamic rebound method as a practical diagnostic tool for field engineers targeting yield strength prediction.

4.7.1 Predictive Fidelity for Structural Yielding

As established in Sections 4.5 and 4.6, the Leeb method demonstrated stronger predictive correlation than static indentation techniques for predicting the 0.2% offset Yield Strength of Grade 300 and 350 steels. Achieving a correlation coefficient (R^2) of 0.947, the Leeb predictive model demonstrated a Root Mean Square Error (RMSE) of 13.67 MPa. Furthermore, the Mean Percentage Error (MPE) for the Leeb yield model was calculated at -0.09%. These results indicate that, under controlled laboratory conditions, the Leeb method can provide a consistent correlation with yield strength.

4.7.2 Translation from Laboratory to Field Boundary Conditions

While the statistical correlation is robust, the practical field application of the Leeb device is contingent upon satisfying dynamic boundary conditions. During the laboratory phase (Section 4.4.4.1), it was demonstrated that low-mass, thin-walled elements (5-10 mm coupons and < 5 kg) suffer significant kinetic energy loss unless rigidly coupled with an acoustic medium to a high-mass support.

This behaviour is attributed to partial dissipation of impact energy through structural flexure rather than localized plastic deformation. When rigid coupling was applied, the variability was significantly reduced, and stable measurements were obtained.

In practical structural applications, full-scale members such as Universal Beams and Square Hollow Sections generally provide sufficient mass and stiffness to satisfy the testing requirements. As a result, these elements may inherently meet the boundary conditions required for reliable Leeb measurements, unlike small laboratory coupons.

4.7.3 Field Validation Case Study

To evaluate the translation of laboratory models to full-scale members, a multi-tiered diagnostic assessment was conducted on existing structural elements in the field. Testing was executed across three distinct structural boundary conditions: a thin-walled steel floor decking system, a load-bearing chassis of a prefabricated transportable cabin, and a heavy Universal Beam integrated into an existing steel framework (Figure 4.10).

(a) (b) (c)

Figure 4.10: In-situ deployment of the Leeb testing, done on (a) thin floor decking rectangular hollow section (RHS), (b) cabin chassis C channel, (c) heavy rusted Beam UB.

Prior to dynamic testing, the localized test zones on all three structural elements were mechanically prepared using portable manual abrasives (standard industrial sandpaper) to remove surface oxidation, mill scale, and protective coatings. To ensure the physical boundary conditions approximated the laboratory environment, surface topography was verified in-situ utilizing a portable surface roughness profilometer (Figure 4.11). The in-situ preparation achieved Mean Surface Roughness (R_a) values of 0.191 µm for the C-channel, 0.21 µm for the thin RHS decking, and 0.34 µm for the heavy Universal Beam. This empirical data indicates that the optimal threshold established during laboratory testing ($R_a \leq 0.4$ µm) can be achieved in the field without the need for stationary metallographic polishing equipment.

(a) (b) (c)

Figure 4.11: In-situ surface topography verification using a portable roughness profilometer on the mechanically prepared test zones, (a) thin floor decking RHS, (b) cabin chassis C channel, (c) Heavy rusted Beam UB.

Following surface qualification, testing commenced. The heavy Universal Beam and the loaded cabin chassis inherently satisfied the requisite mass boundary conditions. To ensure statistical reliability during the field assessment, 5 spatially distributed Leeb impact tests was executed on each structural element (all individual in-situ Leeb measurements is provided in Appendix G).

As demonstrated in Table 4.7, the Leeb method produced highly stable and repeatable rebound readings across both of these rigid elements. Applying the primary predictive regression model (Equation 4.1) to these mean Leeb values yielded calculated Yield Strengths that align closely with expected structural design parameters for these types of members.

Table 4.7: In-Situ Assessment of Structural Members

Structural Element	Mean Leeb Hardness (HL)	Predicted Yield Strength (MPa)
Heavy Rusted Universal Beam	393.6	362.69
C-Channel (Cabin Chassis)	365.4	305.89
Thin RHS (Floor Decking)	Invalid Scatter (218 – 254)	N/A

On the other hand, testing conducted on the thin steel floor decking demonstrated significant predictive variance. The Leeb impactor registered considerable data scatter, fluctuating between 218 and 254 HL. The thin nature of the decking acted as a localized diaphragm, dissipating the kinetic energy of the impactor via macroscopic flexure rather than inducing pure plastic deformation. Therefore, while effective on massive or fully-loaded structural members, the Leeb method should not be deployed on unsupported, thin-walled geometries without rigid backing, as the resulting structural resonance will compromise the predictive model.

It should be noted that the field validation was conducted on active, in-service structural elements, destructive coupon extraction was physically impermissible. Consequently, a definitive empirical baseline (true yield strength) is unavailable, precluding standard statistical error analysis for the in-situ data. However, the efficacy of the model can be evaluated through the metric of predictive rationality. The predicted yield strengths generated by the Leeb model (362.7 MPa for the heavy Universal Beam and 305.9 MPa for the C-Channel) are consistent with the expected over-strength margins of historical and contemporary structural steel elements, which are typically specified as Grade 250 or Grade 300 in the New Zealand structural steel standards (AS/NZS 3679.1) [22] and industry guidelines [50]. This supports the premise that, when boundary conditions are satisfied, the laboratory-derived mathematical models translate effectively to the field, outputting historically consistent structural capacities.

4.7.4 Operational Directives for Field Engineers

For in-situ diagnostic assessments, equipment manufacturer guidelines stipulate that a global mass exceeding 5 kg and a nominal localized thickness of ≥5 mm are sufficient to negate the need for acoustic coupling. The empirical field testing conducted in this study validated this operational threshold. The uncoupled testing on the standard Universal Beam and the C-channel chassis (both possessing localized thicknesses well above 5 mm and satisfying the mass requirement) yielded stable, mathematically valid yield strength predictions.

However, dynamic measurement limitations are introduced when assessing structural profiles that fall below this 5 mm threshold. This was empirically observed during the assessment of the 1 to 2 mm steel floor decking. Striking this unsupported, thin profile induced a localized vibration, dissipating the impact body's kinetic energy and resulting in the significant data scatter observed in Section 4.7.3. Furthermore, ASTM A956 [16] explicitly dictates that for a standard Type D impact device, the minimum material thickness is 3 mm, even when rigid acoustic coupling is applied. As the floor decking (1–2 mm) fell below this operational threshold, the Type D impactor was fundamentally incapable of inducing pure localized plastic deformation without structural resonance.

Therefore, for valid in-situ deployment, field engineers can utilize the Leeb dynamic rebound method for standard structural frameworks (beams, columns, and heavy channels) possessing a nominal thickness of 5 mm or greater. On the other hand, it is recommended that standard Leeb testing (Type D) never be deployed on ultra-thin geometries (such as 1–2 mm light-gauge RHS or floor decking). For such profiles, even the application of rigid acoustic coupling and a temporary backing block is insufficient to satisfy ASTM codes, and alternative NDT modalities or specialized low-impact devices (e.g., Leeb Type C) must be utilized.

Regarding surface preparation for in-situ assessment, while the laboratory-derived regression models in this study utilized mechanically ground surfaces ($R_a \leq 0.4$ µm) to limit baseline scatter, the field validation phase demonstrated that these conditions are achievable without specialized stationary equipment. Standard equipment specifications for the TIME 5100 Impact Device dictate a maximum surface roughness (R_a) of 1.6 µm for valid dynamic testing. The in-situ profilometer verifications conducted in this study (with R_a values ranging from 0.191 µm to 0.34 µm) prove that the stricter laboratory baseline can be met using simple manual abrasives.

Crucially, while this optimal topography is easily attainable in the field, for practical field applications the primary objective is to remove loose oxidation, flaking mill scale, and protective coatings to expose a flat, uniform base metal. As long as this localized preparation successfully mitigates energy loss from surface irregularities and maintains a general surface roughness below the manufacturer's 1.6 µm threshold, the laboratory-derived regression models remain a deployable asset for on-site engineers.

4.8 Chapter Summary

This chapter presented the empirical results and statistical analysis of the non-destructive hardness and destructive tensile testing on Grade 300 and 350 structural steels. By diagnosing surface boundary conditions and microstructural variances, highly reliable bivariate linear regression models were developed. Error analysis confirmed the statistical reliability of these models, and in-situ field testing successfully validated the practical deployment of the Leeb dynamic rebound method for existing infrastructure. Having established these mathematical correlations, the subsequent chapter will synthesize these findings into final conclusions and outline recommendations for future research.

Chapter 5: Conclusions and Recommendations

5.1 Research Summary

The primary objective of this research was to evaluate the predictive correlation of multi-modal non-destructive hardness testing (macro, micro, and dynamic rebound) as a mechanical indicator for determining the bulk tensile properties of standard Grade 300 and Grade 350 structural carbon steels. By physically extracting 36 localized coupons from a Universal Beam and Square Hollow Section, benchmark destructive uniaxial tensile tests were correlated against Brinell, Rockwell, Vickers, and Leeb hardness scales to establish empirically validated predictive models for potential structural assessment.

5.2 Key Conclusions

Based on the empirical data and statistical analyses of the investigated Grade 300 Universal Beams and Grade 350 Square Hollow Sections, the following core conclusions are drawn:

- **Spatial Variability in Structural Profiles:** Uniaxial tensile testing confirmed clear spatial variability. The thinner Universal Beam web (IB-W) exhibited an average yield strength nearly 100 MPa higher than the thicker flange (IB-F). Qualitative SEM observations suggest this variance aligns with microstructural refinement driven by cooling-rate disparities during manufacturing. Consequently, predictive NDT models should account for localized spatial extraction.
- **Leeb Rebound for Yield Prediction:** Under controlled surface preparation, dynamic macro-scale testing demonstrated stronger correlation than static indentation for predicting the 0.2% offset Yield Strength. The Leeb method yielded high statistical correlation (R^2 = 0.947, MPE = -0.09%), effectively capturing the fundamental boundary resistance governing initial macroscopic plastic deformation.
- **Proposed Equation for Yield Prediction (Leeb):** Under controlled surface preparation, dynamic macro-scale testing demonstrated stronger correlation than static indentation for predicting the 0.2% offset Yield Strength. The proposed Leeb predictive equation ($YS = 2.0142 \cdot HL - 430.1$) yielded high statistical correlation (R^2 = 0.947, MPE = -0.09%), effectively capturing the fundamental boundary resistance governing initial macroscopic plastic deformation.
- **Proposed Equation for Ultimate Tensile Capacity (Vickers):** The predictive hierarchy inverted at the ultimate fracture limit. The proposed Vickers regression model ($UTS = 1.7017 \cdot HV + 231.9$) provided the most reliable Ultimate Tensile Strength (UTS) estimates (R^2 = 0.847, MPE = -0.04%), reflecting its sensitivity to localized strain-hardening capacity. Conversely, Vickers exhibited higher scatter and larger prediction errors for Yield Strength and is less suitable for bulk yield prediction.
- **Vickers Micro-Indentation for Ultimate Tensile Capacity:** The predictive hierarchy inverted at the ultimate fracture limit. The Vickers method provided the most reliable Ultimate Tensile Strength (UTS) estimates (R^2 = 0.847), reflecting its sensitivity to localized strain-hardening capacity. Conversely, Vickers exhibited higher scatter and larger prediction errors for Yield Strength and is less suitable for bulk yield prediction.
- **Criticality of Boundary Conditions:** The accuracy of Leeb-based prediction is highly sensitive to specimen boundary conditions. Uncoupled testing on thin-walled elements (nominal thickness < 5 mm) produced significant predictive variance due to kinetic energy loss via localized flexure. Rigid coupling is mandatory for structural members falling below this operational threshold, as further dictated by ASTM A956 [16].

- **Viability for Assessment:** When adequate structural boundary conditions (a nominal section thickness of ≥ 5 mm and a global mass > 5 kg) are present, or when rigid coupling is applied to thinner geometries, portable Leeb hardness testing can serve as a practical supplementary tool for yield strength assessment within the specific steel grades, geometries, and surface conditions investigated in this research.
- **Scope of Validity for Proposed Models:** It must be explicitly noted that the empirical regression models derived in this study are strictly calibrated to the structural profiles investigated. Therefore, the proposed equations are currently validated only for standardized AS/NZS hot-rolled Grade 300 and cold-formed Grade 350 carbon steels. Extrapolating these predictive models to higher-strength alloys, significantly thicker cross-sections, or alternate manufacturing profiles without conducting further localized baseline testing is not recommended.

5.3 Preliminary Recommendations for Practice

To support diagnostic reliability, the following operational recommendations are proposed for engineers considering non-destructive hardness testing for structural assessments:

- **Model Applicability and Scope:** The predictive correlations developed in this study are specifically derived from Grade 300 Universal Beams and Grade 350 Square Hollow Sections. For differing material specifications, chemistries, or manufacturing routes, localized calibration against destructive tensile testing is advised before relying on hardness-based capacity assessments.
- **Target Selection and Spatial Rigidity:** Leeb measurements are best taken on relatively flat, high-rigidity regions, such as thicker flange elements, that allow for flush seating of the impact device. Furthermore, it is recommended that multiple impacts be averaged at each verified location to reduce the influence of localized variances.
- **Coupling Compliance:** Testing uncoupled on thin-walled members (nominal thickness < 5 mm) should be avoided due to the risk of significant kinetic energy loss. If thinner sections must be evaluated, engineers are advised to temporarily affix an acoustic backing mass and utilize a viscous couplant to approximate infinite-mass boundary conditions.
- **Surface Topography Qualification:** To maintain hardness variability within the bounds observed under laboratory conditions, field test zones should be mechanically prepared to achieve a uniform surface. While laboratory baselines utilized Ra ≤ 0.4 µm, field engineers should ensure that, at a minimum, all loose mill scale, corrosion products, and protective coatings are removed prior to impact to comply with manufacturer specifications (typically Ra ≤ 1.6 µm).
- **Modality Selection:** Portable Leeb hardness testing is recommended as the primary modality for evaluating 0.2% offset Yield Strength. Conversely, correlations derived from Vickers micro-indentation for Ultimate Tensile Strength (UTS) should be treated as supplementary, and UTS estimates derived from field hardness should ideally be validated against representative tensile data where possible.

5.4 Recommendations for Future Research

While this benchmark study established correlations under controlled boundary conditions, future research should expand the diagnostic framework:

- **Influence of Surface Morphology:** Future investigations should systematically isolate surface roughness as an independent variable, deliberately generating graded roughness profiles (e.g., using field-standard angle grinders) to quantify the exact acoustic sensitivity thresholds of portable Leeb devices outside of laboratory polishing parameters.

- **Assessment of Aged and Fatigued Infrastructure:** The predictive models in this study were developed utilizing virgin structural steel. Subsequent research should apply these established correlations to historically aged or cyclically fatigued steel members to evaluate the impact of long-term microstructural degradation on surface hardness relationships.
- **Expanded Material Grade Matrix:** Future research should apply these predictive methodologies to higher-grade structural steels. Integrating the empirical baseline generated in this study with future high-grade datasets could contribute to a more comprehensive hardness-to-tensile diagnostic database for the New Zealand infrastructure sector.
- **Integration of Machine Learning Algorithms:** While the bivariate linear regression models developed in this study demonstrated high correlation, future research could leverage this empirical dataset as a foundational training matrix for advanced machine learning (ML) models. Feeding multi-modal NDT data, coupled with secondary variables such as localized thickness and surface roughness, into neural networks may aid in developing multi-variable predictive algorithms for structural assessment.

References

[1] International Organization for Standardization, “ISO 6892-1:2019 — Metallic materials — Tensile testing — Part 1: Method of test at room temperature,” ISO 6892-1, 2019. [Online]. Available: https://www.iso.org/standard/78322.html

[2] ASTM International, *A370-22 Test Methods and Definitions for Mechanical Testing of Steel Products*, West Conshohocken, PA. doi: 10.1520/A0370-22.

[3] C. Hellier, *Handbook of nondestructive evaluation*, 2nd ed. New York: McGraw-Hill, 2013.

[4] D. Tabor, “The Hardness of Metals,” vol. 192, no. 1049, pp. 247–274, 1951, doi: 10.1098/rspa.1951.0104.

[5] E. J. Pavlina and C. J. Van Tyne, “Correlation of Yield Strength and Tensile Strength with Hardness for Steels,” *J. Mater. Eng. Perform.*, vol. 17, no. 6, pp. 888–893, Dec. 2008, doi: 10.1007/s11665-008-9225-5.

[6] W. D. Callister and D. G. Rethwisch, *Materials science and engineering: an introduction*, 10th edition. Hoboken, NJ: Wiley, 2018.

[7] P. Organek, B. Gosowski, and M. Redecki, “Relationship between Brinell hardness and the strength of structural steels,” *Structures*, vol. 59, p. 105701, Jan. 2024, doi: 10.1016/j.istruc.2023.105701.

[8] M. O. Lai and K. B. Lim, “On the prediction of tensile properties from hardness tests,” *J. Mater. Sci.*, vol. 26, no. 8, pp. 2031–2036, Apr. 1991, doi: 10.1007/BF00549163.

[9] International Organization for Standardization, “ISO 6506-1:2014 — Metallic materials — Brinell hardness test — Part 1: Test method,” Geneva, Switzerland, ISO 6506-1, 2014. [Online]. Available: https://www.iso.org/standard/59671.html

[10] International Organization for Standardization, “ISO 6506-2:2014 — Metallic materials — Brinell hardness test — Part 2: Verification and calibration of testing machines,” Geneva, Switzerland, ISO 6506-2, 2014. [Online]. Available: https://www.iso.org/standard/59672.html

[11] International Organization for Standardization, “ISO 6508 — Metallic materials — Rockwell hardness test — Part 1: Test method,” Geneva, Switzerland, ISO 6508-1, 2023. [Online]. Available: https://www.iso.org/obp/ui/en/#iso:std:iso:6508:-1:ed-5:v1:en

[12] International Organization for Standardization, “ISO 6507 — Metallic materials — Vickers hardness test — Part 1: Test method,” Geneva, Switzerland, ISO 6507, 2023. [Online]. Available: https://www.iso.org/standard/83898.html

[13] ASTM International, *E10-23 Test Method for Brinell Hardness of Metallic Materials*, West Conshohocken, PA., 2023. doi: 10.1520/E0010-23.

[14] ASTM International, *E18-18A Test Methods for Rockwell Hardness of Metallic Materials*, West Conshohocken, PA. doi: 10.1520/E0018-18A.

[15] ASTM International, *E92-23 Test Methods for Vickers Hardness and Knoop Hardness of Metallic Materials*, West Conshohocken, PA., 2023. doi: 10.1520/E0092-23.

[16] ASTM International, *A956-22 Test Method for Leeb Hardness Testing of Steel Products*, West Conshohocken, PA. doi: 10.1520/A0956_A0956M-22.

[17]A. Brencich and F. Campeggio, “Leeb hardness for yielding stress assessment of steel bars in existing reinforced structures,” *Constr. Build. Mater.*, vol. 227, p. 116570, Dec. 2019, doi: 10.1016/j.conbuildmat.2019.07.296.

[18]H. Nashid *et al.*, “Non-destructive method to investigate the hardness-plastic strain relationship in cyclically deformed structural steel elements,” *Bull. N. Z. Soc. Earthq. Eng.*, vol. 47, no. 3, pp. 181–189, Sep. 2014, doi: 10.5459/bnzsee.47.3.181-189.

[19]E. S. Gadelmawla, M. M. Koura, T. M. A. Maksoud, I. M. Elewa, and H. H. Soliman, “Roughness parameters,” *J. Mater. Process. Technol.*, vol. 123, no. 1, pp. 133–145, Apr. 2002, doi: 10.1016/S0924-0136(02)00060-2.

[20]International Organization for Standardization, “ISO 18265:2013 — Metallic materials — Conversion of hardness values,” Geneva, Switzerland, 2013. [Online]. Available: https://www.iso.org/standard/53810.html

[21]ASTM International, *ASTM E140-12B Hardness Conversion Tables for Metals Relationship Among Brinell Hardness, Vickers Hardness, Rockwell Hardness, Superficial Hardness, Knoop Hardness, Scleroscope Hardness, and Leeb Hardness*, West Conshohocken, PA., 2013. doi: 10.1520/E0140-12B.

[22]Standards Australia/Standards New Zealand, *Structural steel - Part 1: Hot-rolled bars and sections*, AS/NZS 3679.1:2016, Wellington., 2016.

[23]M. Sansom and N. Baddoo, “Structural Steel Reuse: Assessment, testing and design principles,” The Steel Construction Institute, Berkshire, U.K., SCI Publication P427, 2019. [Online]. Available: https://steel-sci.com/assets/downloads/steel-reuse-event-8th-october-2019/SCI_P427.pdf

[24]H. Qiu, R. Ueji, and T. Inoue, “Yield-Point Phenomenon and Plastic Bands in Ferrite–Pearlite Steels,” *Materials*, vol. 16, no. 1, p. 195, Dec. 2022, doi: 10.3390/ma16010195.

[25]J. T. Wang, C. Xu, Z. Z. Du, G. Z. Qu, and T. G. Langdon, “Microstructure and properties of a low-carbon steel processed by equal-channel angular pressing,” *Mater. Sci. Eng. A*, vol. 410–411, pp. 312–315, Nov. 2005, doi: 10.1016/j.msea.2005.08.111.

[26]T. Hanamura and S. Torizuka, “Dependence of Yield Strength on Ferrite Grain Size in Ferrite/Cementite and Ferrite/Pearlite Structures of Medium Carbon Steel,” *Mater. Sci. Forum*, vol. 638–642, pp. 3248–3253, Jan. 2010, doi: 10.4028/www.scientific.net/MSF.638-642.3248.

[27]E. O. Hall, “The Deformation and Ageing of Mild Steel: III Discussion of Results,” *Proc. Phys. Soc. Sect. B*, vol. 64, no. 9, pp. 747–753, Sep. 1951, doi: 10.1088/0370-1301/64/9/303.

[28]A. M. Glezer, N. A. Shurygina, E. N. Blinova, I. E. Permyakova, and S. A. Firstov, “Approach to the Theoretical Strength of Ti–Ni–Cu Alloy Nanocrystals by Grain Boundary Design,” *J. Mater. Sci. Technol.*, vol. 31, no. 1, pp. 91–96, Jan. 2015, doi: 10.1016/j.jmst.2014.09.006.

[29]Conrad Paulson; Jeffrey M. Rautenberg; Scott K. Graham; David Darwin, “Defining Yield Strength for Nonprestressed Reinforcing Steel,” *ACI Struct. J.*, vol. 113, no. 1, pp. 169–178, Jan. 2016, doi: 10.14359/51688199.

[30]W. C. Oliver and G. M. Pharr, “An improved technique for determining hardness and elastic modulus using load and displacement sensing indentation experiments,” *J. Mater. Res.*, vol. 7, no. 6, pp. 1564–1583, Jun. 1992, doi: 10.1557/JMR.1992.1564.

[31]G. E. Dieter, *Mechanical metallurgy*, 3. ed., 14. [print.]. in McGraw-Hill series in materials science and engineering. Boston, Mass.: McGraw-Hill, 2000.

[32]R. Ulusay, H. Ersoy, M. O. Sünnetci, and M. Karahan, “The leeb (Equotip) hardness test for rock materials: An overview, assessments on the factors influencing test results, and prediction models based on a large database,” *Bull. Eng. Geol. Environ.*, vol. 84, no. 3, p. 148, Feb. 2025, doi: 10.1007/s10064-025-04170-w.

[33]J. R. Cahoon, W. H. Broughton, and A. R. Kutzak, “The determination of yield strength from hardness measurements,” *Metall. Trans.*, vol. 2, no. 7, pp. 1979–1983, Jul. 1971, doi: 10.1007/BF02913433.

[34]Markovets, M. P., *Determination of mechanical properties of metals by hardness*. Moscow: Mashinostroenie, 1979.

[35]Dudkiewicz J. , Gosowski B., “Generalizations of relations between strength and hardness of steel in structural elements under logitudinal load,” vol. 50, no. 1, pp. 45–67, 2004.

[36]S. Yang, G. Gao, and Z. Xu, “In Situ Steel Strength Evaluation Using Brinell Hardness Method: A Case Study on Q235 and Q345 Steel,” *J. Mater. Civ. Eng.*, vol. 38, no. 5, p. 04026103, May 2026, doi: 10.1061/JMCEE7.MTENG-22292.

[37]A. Umanskii, K. Gogolinskii, V. Syasko, and A. Golev, “Modification of the Leeb Impact Device for Measuring Hardness by the Dynamic Instrumented Indentation Method,” *Inventions*, vol. 7, no. 1, p. 29, Feb. 2022, doi: 10.3390/inventions7010029.

[38]D. Liu, X. Liu, F. Fu, and W. Wang, “Nondestructive Post-fire Damage Assessment of Structural Steel Members Using Leeb Harness Method,” *Fire Technol.*, vol. 56, no. 4, pp. 1777–1799, Jul. 2020, doi: 10.1007/s10694-020-00954-6.

[39]M. Gajdzicki, “Określanie wytrzymałości na rozciąganie stali na podstawie pomiaru twardości Leeba,” *Mater. Bud.*, vol. 1, no. 3, pp. 21–25, Mar. 2024, doi: 10.15199/33.2024.03.04.

[40]A. Formisano, A. Davino, and E. Meglio, “Leeb hardness tests for mechanical characterisation of carpentry steels,” *Int. J. Mason. Res. Innov.*, vol. 8, no. 1, p. 30, 2023, doi: 10.1504/IJMRI.2023.127473.

[41]O. A. Katok, M. R. Muzyka, V. P. Shvets, A. V. Sereda, V. V. Kharchenko, and S. P. Bisyk, “Determination of Hardness of High-Strength Steels by Brinell Method. Part 2. Improvement of the Method and Measurement Results,” *Strength Mater.*, vol. 54, no. 5, pp. 802–808, Sep. 2022, doi: 10.1007/s11223-022-00456-6.

[42]A. Z. Guštin, B. Žužek, B. Podgornik, and V. Kevorkijan, “The uncertainty of hardness measurements related to the measurement method, surface preparation and range of the measurements,” *Mater. Tehnol.*, vol. 53, no. 6, pp. 897–904, Dec. 2019, doi: 10.17222/mit.2019.098.

[43]V. Kharchenko, O. Katok, A. Sereda, M. Rudnitskyi, R. Kravchuk, and S. Bisyk, “Determination of strength characteristics of high-strength sheet steels by hardness and instrumented indentation,” *Procedia Struct. Integr.*, vol. 36, pp. 277–283, 2022, doi: 10.1016/j.prostr.2022.01.035.

[44]C. Qian, Y. Qu, N. Chen, S. Xia, C. Pei, and Z. Chen, “Noncontact evaluation of steel mechanical properties using nonlinear laser ultrasonics,” *NDT E Int.*, vol. 156, p. 103445, Dec. 2025, doi: 10.1016/j.ndteint.2025.103445.

[45]G. Loporcaro, “A least invasive method to estimate the residual strain capacity of steel reinforcement in earthquake-damaged buildings.,” University of Canterbury, 2017. doi: 10.26021/2587.

[46]Mohammed Al-Adawi, “An experimental investigation to estimate the mechanical properties of structural steel using hardness testing,” Thesis, The University of Waikato, Hamilton, New Zealand, 2024.

[47]Govind Gopi, “Comparing hardness tests to estimate, evaluate, and analyse themechanical properties of structural steel,” The University of Waikato, Hamilton, New Zealand, 2024. [Online]. Available: https://hdl.handle.net/10289/17281

[48]B. Gosowski, P. Organek, and M. Redecki, “The relationship between the strength parameters of historical steels and Brinell hardness, and the determination of its ultimate strength,” *Constr. Build. Mater.*, vol. 517, p. 145694, Mar. 2026, doi: 10.1016/j.conbuildmat.2026.145694.

[49]D. C. Montgomery, *Design and analysis of experiments*, Tenth edition. Hoboken, NJ: Wiley, 2020.

[50]M. J. Feeney and G. C. Clifton, “Seismic design procedures for steel structures,” Heavy Engineering Research Association, HERA Report R4-76, 1995.

Appendix A: Mill Cert

The following mill test certificate, provided by Waikato Steel Fabricators Ltd., details the chemical composition and factory-certified baseline mechanical properties for the Grade 350 SHS and Grade 300 Universal Beam (UB) specimens utilized in this research program.

AustubeMills

SUPPLIER: Dalian Steelforce Hi-Tech Co., Ltd.
No. 26 Number 2 Street DD Port,
Dalian Development Zone,
Liaoning, China.

TEST CERTIFICATE NUMBER: 20241202-D046395
LOT NUMBER: D046395
DATE PRINTED: 26-02-2025
PAGE 1 OF 1

CUSTOMER: HJ ASMUSS AUCKLAND

CUSTOMER REFERENCE: 162705

CUSTOMER ITEM NUMBER:

PRODUCT DESCRIPTION

PRODUCT: 125x125x6.0/12m RHS
FINISH: DURAPRIMED
MATERIAL: Cold Formed Structural Steel Hollow Sections
SPECIFICATION: AS/NZS 1163:2016
GRADE: C350L0
STEELMAKING: Basic Oxygen, Continuously Cast, Fine Grained, Fully Killed
STEEL FEED: Coil from Hot Strip Mill
MANUFACTURED DATE: 02-12-2024

CHEMICAL COMPOSITION (% of Elements by Mass)

SGS Test Report Number	Heat Number	SGS Test Laboratory CNAS Accreditation Number	Analysis Type	C	P	Mn	Si	S	Ni	Cr	Mo	Cu
DLIN2411001353ML	AGR21424CD6430	L3437	L	0.050	0.013	1.390	0.020	0.008	0.010	0.030	< 0.010	0.010

CHEMICAL COMPOSITION (% of Elements by Mass)

SGS Test Report Number	Heat Number	SGS Test Laboratory CNAS Accreditation Number	Analysis Type	Al(t) min = 0.02 max = 0.10	B	Ti	Nb	V	CE	CF2	CF3	
DLIN2411001353ML	AGR21424CD6430	L3437	L	0.049	0.0004	0.030	0.010	< 0.010	< 0.293	< 0.050	0.053	

Notes: Chemical Composition
Test Laboratory: SGS-CSTC Standards Technical Services Co., Ltd., Dalian Branch   Analysis Type: Ladle and Cast Analysis (L); Product Analysis (P)
CE = C+Mn/6+(Cr+Mo+V)/5+(Ni+Cu)/15   CF2 = Nb+V+Ti   CF3 = Si+2.5P

MECHANICAL PROPERTIES

SGS Test Report Number	Heat Number	SGS Test Laboratory CNAS Accreditation Number	Test Type	Test Category	Yield (Mpa)	Tensile (Mpa)	Elongation (%)	Impact Testing (Joules) SGS Test Report Number DLIN2412001530ML			
								Test 1	Test 2	Test 3	Average
DLIN2412001463ML	AGR21424CD6430	L3437	LSA	B	465	520	23.5	111	110	124	115

Only for hollow sections, flats, angles, and channels with nominal gauge ⩾ 6mm

Notes: Tensile Test
Test Laboratory: SGS-CSTC Standards Technical Services Co., Ltd., Dalian Branch
Test Type: LSA = Longitudinal strip specimen tested in the artificially aged condition   Test Category - B = Batch; S = Statistical Sampling
Gauge Length Method - E = 5.65xSQRT(So)
All Tensile properties are determined using samples from production personnel and tested in accordance with AS 1391:2020

Notes: Impact Test
Test Laboratory: SGS-CSTC Standards Technical Services Co., Ltd., Dalian Branch
All Impact properties on gauges ⩾ 6mm are determined using samples from production personnel and tested in accordance with AS 1544.2:2003 at 0°
For products complying to AS/NZS1163:2016 with a nominal thickness < 6.0mm L0 properties have been derived as per Clause 9.4.2.3

MANAGEMENT SYSTEM CERTIFICATION:
Dalian Steelforce Hi-Tech Co.,Ltd. has the following management system certificates:-

Standard	Certificate Number	Expiry Date	Certification Body
ISO 9001:2015	FM 641461	29/11/2027	British Standards Institution (BSI)
ISO 14001:2015	EMS 641462	29/11/2027	British Standards Institution (BSI)
ISO 45001:2018	OHS 641463	29/11/2027	British Standards Institution (BSI)

JAS-ANZ ACCREDITED CONFORMANCE ASSESSMENT BODY:
Steelforce Australia Pty Ltd has the following product certification for it's Dalian Steelforce Hi-Tech Co.,Ltd. manufacturing facility:-

Standard	Certificate Number	Expiry Date	Certification Scheme	Certification Body
AS/NZS1163:2016	BMP 680293	20/09/2027	BSI Benchmark Product Certification	British Standards Institution (BSI)

Australian Tube Mills has the following certification for product manufactured under exclusive agreement by Dalian Steelforce Hi-Tech Co.,Ltd.:-

Standard	Certificate Number	Expiry Date	Certification Scheme	Certification Body
AS/NZS1163	191003	31/12/2025	ACRS Product Certification	Australasian Certification Authority for Reinforcing and Structural Steels

Dalian Steelforce Hi-Tech Co.,Ltd. confirms that the information included in this Test Certificate agrees with the records of Dalian Steelforce Hi-Tech Co., Ltd. and the product supplied conforms to the requirements of the Standard.

Authorized Signatory: Gary Chen   Title: Quality Manager

Figure A. 1: Certified mill test report and chemical analysis for the Grade 350 SHS.

SIAM YAMATO STEEL CO., LTD.
MILL INSPECTION CERTIFICATE
In Accordance with DIN 50049 / EN 10204-3.1
Head office : 1 Siam Cement Road, Bangsue, Bangkok Thailand 10800
Tel : (662) 586-2783-4, 5865329-30 Fax: (662) 586 2687, 910-3123

This document issued in accordance with NSC-ONSC Accreditation requirement. NSC-ONSC accredited testing No.0033 for compliance with ISO/IEC 17025
NSC-TISI-TIS 17025
TESTING 0033

SYS's Quality management system is certified by MASCI (Certificate No. QMS 03173/777)

Certificate No. : **42125050123**
Reference No. : **OCE2500247/1**
D/P No. : 3810073744 , 3810073745 , 3810073746 , 3810073747 , 3810074534 , 3810074535 , 3810074536
Customer : **STEEL AND TUBE HOLDINGS LTD**
Description of Goods : Hot Rolled Structural Steel
Remark 1 : CONFORMED TO AS/NZS 3679.1 : 2016 GRADE AS/NZS 3679.1-300S0
Remark 2 :
Remark 3 :

Standard : AS/NZS 3679.1:2016 AS/NZS 3679.1-300S0
Steelmaking and Manufacturing Process:EAF,Cast Analysis (L)
Location of sample and test piece : Comply with AS/NZS 3679.1 :2016
Type of Impact test piece : Charpy V-notch
Tensile Test : Comply with AS 1391:2020
Impact Test : Comply with AS 1544.2-2003
Shape of Tensile test piece : Rectangular cross-section
Marking of the product : Marking and Information available on Sticker

Revision : 00
Date of Issue : 24/05/2025
Page 1 of 2

Dimension & Length	Grade	Qty (Pcs.)	Heat No.	Yield Str. (MPa)	Mechanical Property (Test Piece Direction : L) Tensile Str. (MPa)	Elong.(%) (5.65√S0)	Bend Test	Charpy Impact (J) /0°C Test1	Test2	Test3	Avg.	Chemical Composition (%) C x100	Si x100	Mn x100	Cu x100	Al x1000	P x1000	S x1000	Nb x1000	V x1000	Ni x100	Cr x100	Ti x1000	Mo x1000	CE(1) x100	B x10000
310 UB 40.4KG/MX12.00M	AS/NZS 3679.1-300S0	2	5A1516	385	520	31.92	-	-	-	-	-	14	21	94	21	2	14	10	0	4	8	13	0	17	35	4
				395	530	33.66	-	-	-	-	-	14	21	94	21	2	14	10	0	4	8	13	0	17	35	4
310 UB 40.4KG/MX12.00M	AS/NZS 3679.1-300S0	5	5A1517	375	500	32.96	-	-	-	-	-	14	20	93	19	3	16	9	0	3	8	12	0	16	34	4
				380	510	34.46	-	-	-	-	-	14	20	93	19	3	16	9	0	3	8	12	0	16	34	4
310 UB 40.4KG/MX12.00M	AS/NZS 3679.1-300S0	3	5A1673	385	510	34.88	-	-	-	-	-	14	20	99	23	2	13	15	0	3	8	8	0	13	35	4
				385	520	34.08	-	-	-	-	-	14	20	99	23	2	13	15	0	3	8	8	0	13	35	4
310 UB 40.4KG/MX9.00M	AS/NZS 3679.1-300S0	8	5A1516	385	520	31.92	-	-	-	-	-	14	21	94	21	2	14	10	0	4	8	13	0	17	35	4
				395	530	33.66	-	-	-	-	-	14	21	94	21	2	14	10	0	4	8	13	0	17	35	4
310 UB 40.4KG/MX9.00M	AS/NZS 3679.1-300S0	1	5A1517	375	500	32.96	-	-	-	-	-	14	20	93	19	3	16	9	0	3	8	12	0	16	34	4
				380	510	34.46	-	-	-	-	-	14	20	93	19	3	16	9	0	3	8	12	0	16	34	4
310 UB 46.2KG/MX12.00M	AS/NZS 3679.1-300S0	23	5A1518	340	480	32.50	-	-	-	-	-	14	20	94	19	3	16	13	0	3	7	12	0	17	34	4
				355	490	33.16	-	-	-	-	-	14	20	94	19	3	16	13	0	3	7	12	0	17	34	4
310 UB 46.2KG/MX12.00M	AS/NZS 3679.1-300S0	1	5A1519	340	490	35.88	-	-	-	-	-	13	19	91	21	3	20	10	0	4	8	18	0	21	34	4
				360	500	34.16	-	-	-	-	-	13	19	91	21	3	20	10	0	4	8	18	0	21	34	4
360 UB 44.7KG/MX12.00M	AS/NZS 3679.1-300S0	4	5A1515	365	510	34.66	-	-	-	-	-	14	20	85	19	3	13	13	0	5	9	14	0	24	33	4
				385	510	29.14	-	-	-	-	-	14	20	85	19	3	13	13	0	5	9	14	0	24	33	4

Checked By : Finished Goods Checking Operator
Remark : CE(1) = Carbon equivalent
- Carbon equivalent (CE)(1) = C+ (Mn/6) + (Cr+Mo+V)/5 + (Ni+Cu)/15

We hereby certify that the material described herein has been tested and inspected in accordance with the requirements of the above specification.
Manufactured by Siam Yamato Steel Co.,Ltd.
-A Chemical composition of carbon(C), Phosphorus(P), manganese (Mn), Silicon (Si),sulphur (S), chromium (Cr), molybdenum (Mo), vanadium (V), nickel (Ni), copper (Cu),titanium (Ti), niobium (Nb), boron (B) test performed by NSC-ONSC accredited testing No. as above for compliance with ISO/IEC 17025

Kowit P.
Mr. Kowit Phakdeelikit
Quality Promotion Department Manager

QP 206 (11-01/07/50)

Figure A. 2: Certified mill test report and chemical analysis for the Grade 300 Universal Beam.

Appendix B: Destructive Tensile Testing Results

B.1 Tensile Data Summary

Table B. 1:Master Experimental Data Log (Hardness and Destructive Tensile Result)

Specimen	Section Type	Location	Thickness (mm)	Yield (MPa)	UTS (MPa)
SQ-1	SHS	Wall	6	510	544.24
SQ-2	SHS	Wall	6	511	544.67
SQ-3	SHS	Wall	6	516	531
SQ-4	SHS	Wall	6	499	543
IB-W-MT-1	UB	Web	6	456.46	563
IB-W-MB-2	UB	Web	6	459.23	563
IB-W-T-3	UB	Web	6	431.01	551
IB-W-MT-4	UB	Web	6	479.98	575
IB-W-M-5	UB	Web	6	480.05	584
IB-F-B-1	UB	Flange	10	383.89	517.58
IB-F-B-2	UB	Flange	10	372.05	512.8
SQ-5	SHS	Wall	6	514.8	548
SQ-6	SHS	Wall	6	506.9	547.29
SQ-7	SHS	Wall	6	464.13	515.7
IB-W-MB-6	UB	Web	6	474.68	576.449
IB-W-B-7	UB	Web	6	446.11	556.64
IB-W-MT-8	UB	Web	6	484.21	584.1
IB-F-T-3	UB	Flange	10	361.79	508.27
IB-F-T-4	UB	Flange	10	369.02	514.429
SQ-8	SHS	Wall	6	519.02	565.22
SQ-9	SHS	Wall	6	487.96	535.89
SQ-10	SHS	Wall	6	530.87	573.94
SQ-11	SHS	Wall	6	496.05	544.15
SQ-12	SHS	Wall	6	500.92	544.76
SQ-13	SHS	Wall	6	536.68	588.88
IB-W-MB-9	UB	Web	6	482.02	579.57
IB-W-MB-10	UB	Web	6	480.77	580.12
IB-W-MT-11	UB	Web	6	478.16	583.52
IB-F-T-5	UB	Flange	10	371.05	514.32
IB-F-B-6	UB	Flange	10	362.86	506.19
IB-F-B-7	UB	Flange	10	375.79	514.98
IB-F-B-8	UB	Flange	10	372.31	512.31
IB-F-T-9	UB	Flange	10	396.7	521.53
IB-F-T-10	UB	Flange	10	384.36	517.47
IB-F-B-11	UB	Flange	10	396.08	519.46
IB-F-T-12	UB	Flange	10	369.4	509.95

B.2 Individual Stress-Strain Curves

B.2.1 Grade 350 SHS (SQ)

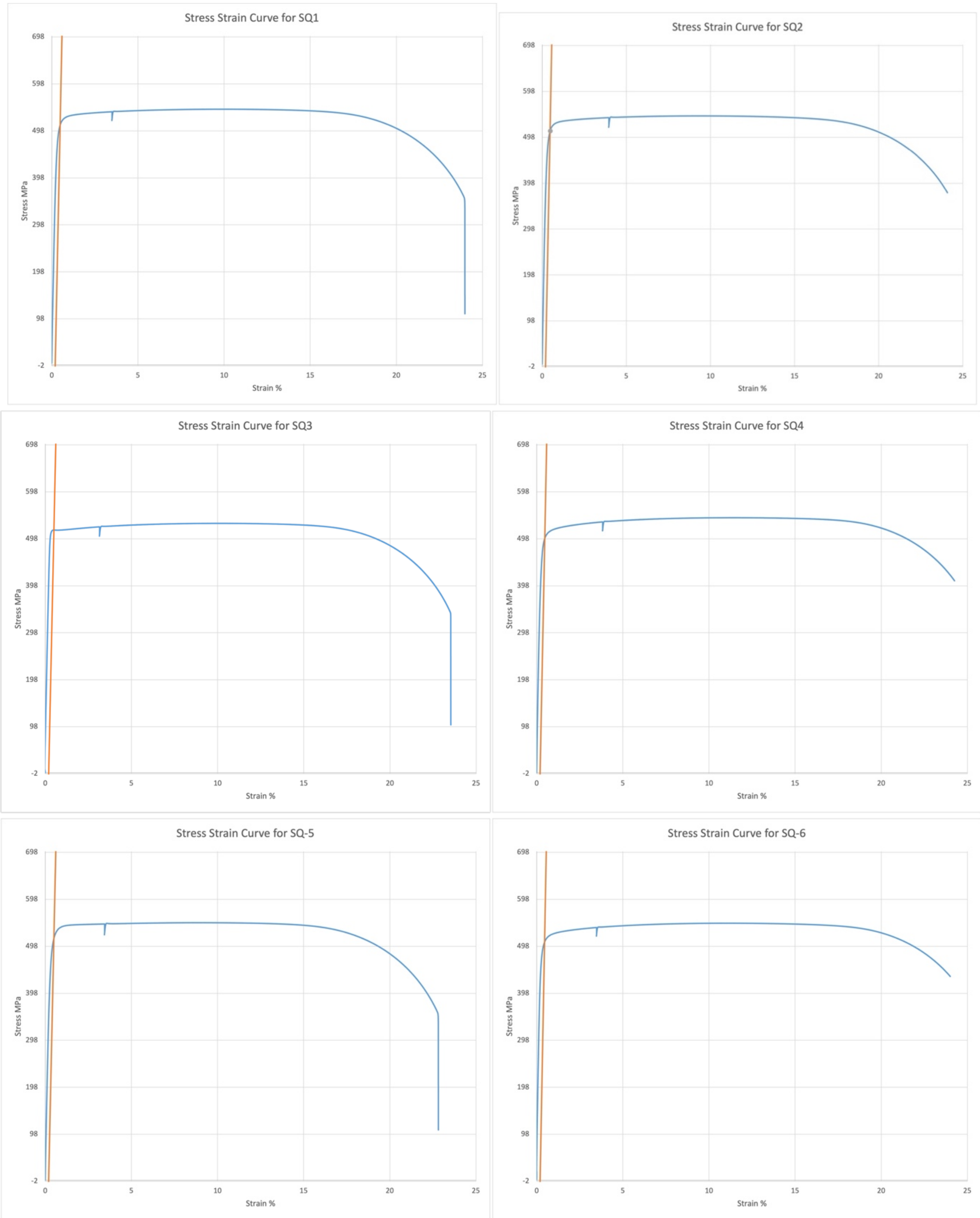

Figure B. 1:Individual stress-strain profiles with 0.2% offset line for Grade 350 SHS SQ tensile specimens (1-6).

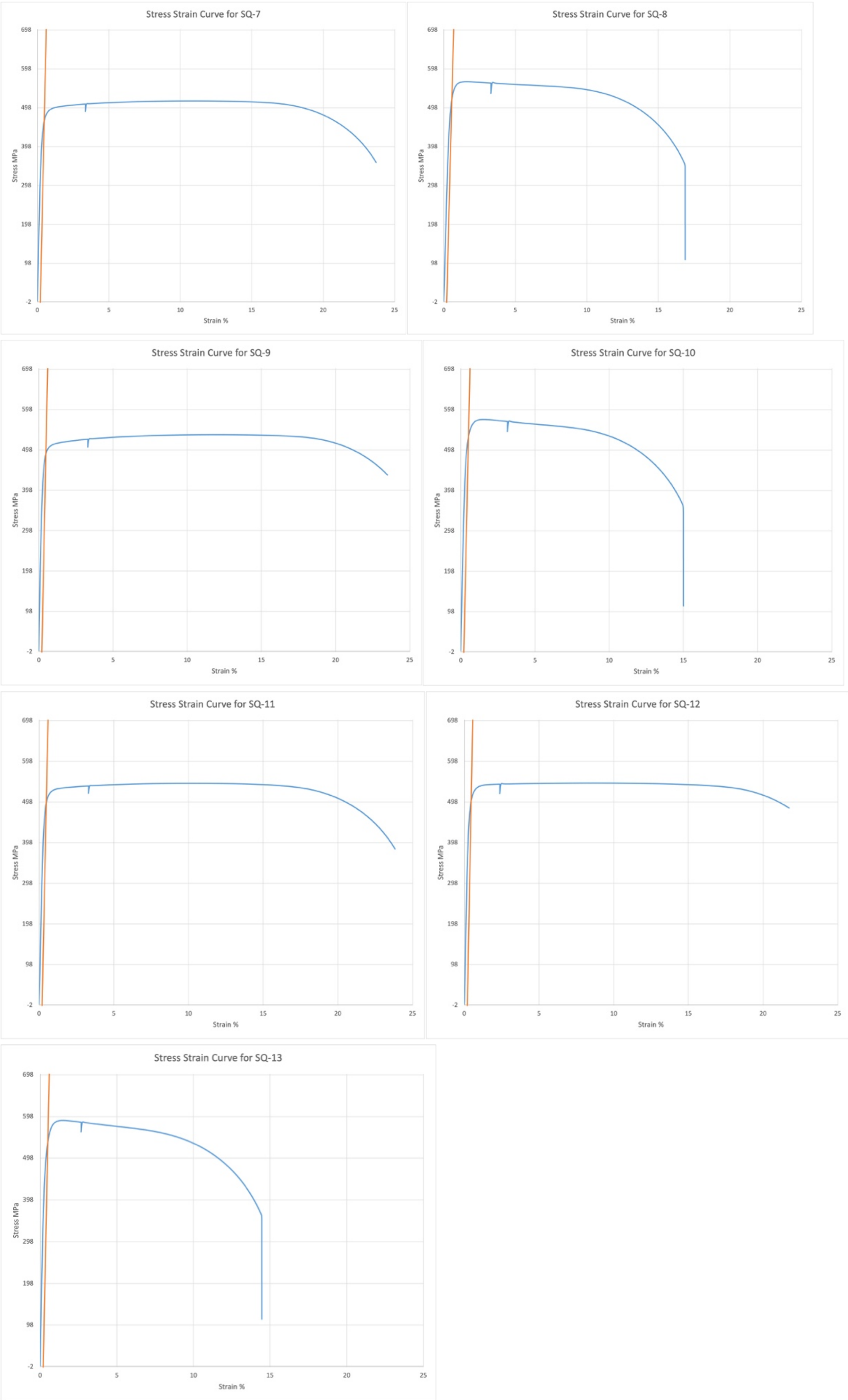

Figure B. 2: Individual stress-strain profiles with 0.2% offset line for Grade 350 SHS (SQ) tensile specimens (7-13).

B.2.2 Grade 300 UB Web (IB-W)

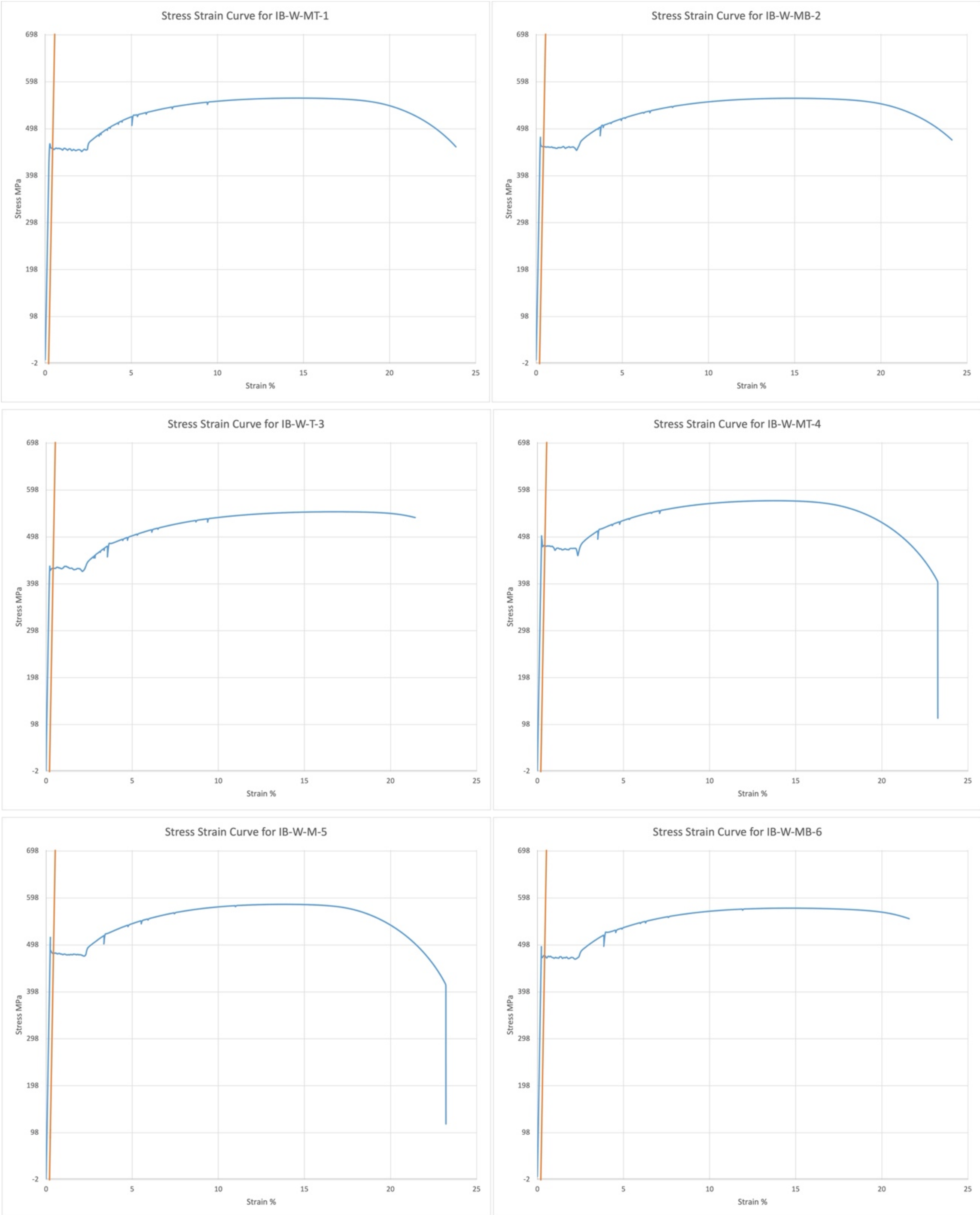

Figure B. 3: Individual stress-strain profiles with 0.2% offset line for Grade 300 UB Web (IB-W) tensile specimens (1-6).

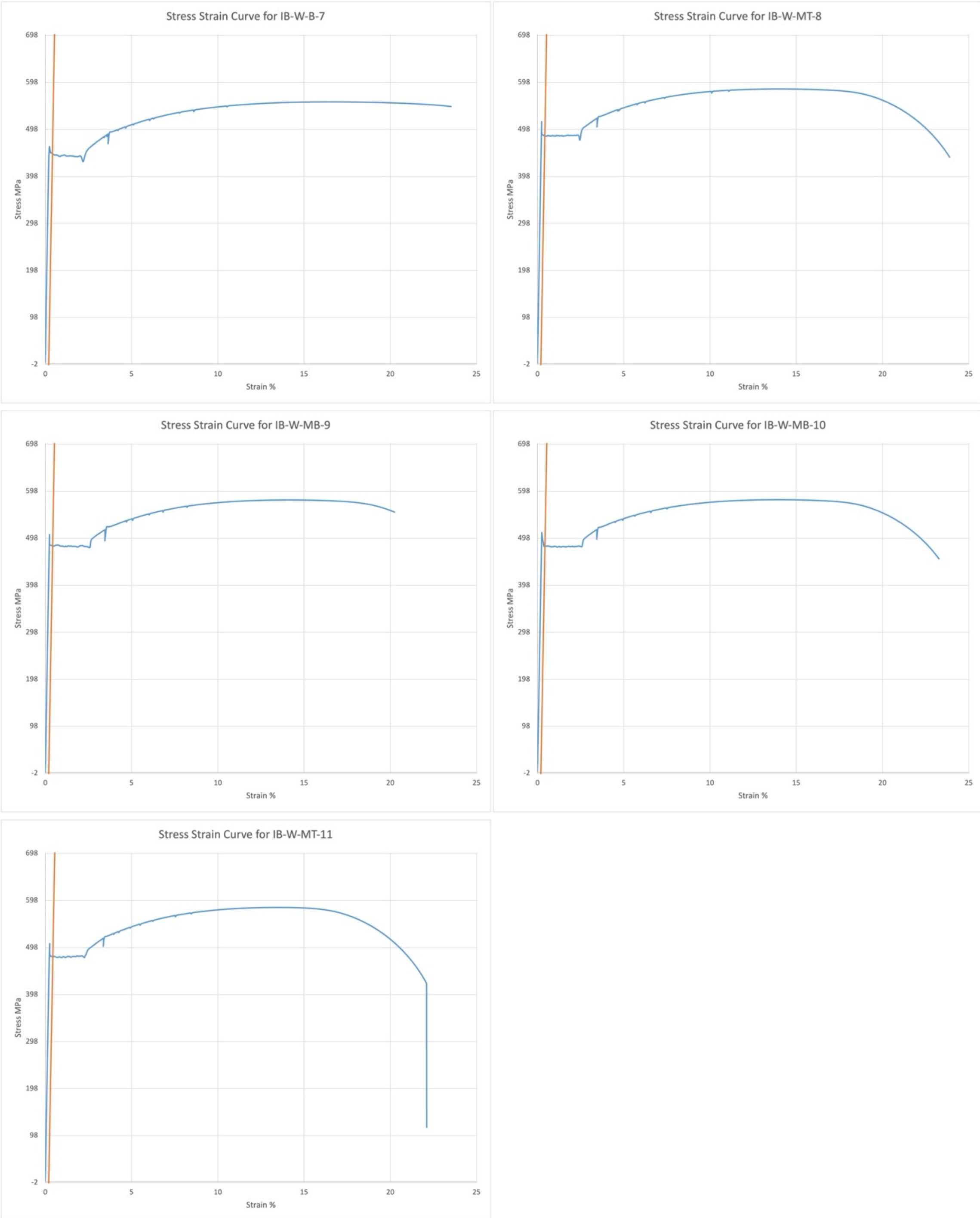

Figure B. 4: Individual stress-strain profiles with 0.2% offset line for Grade 300 UB Web (IB-W) tensile specimens (7-11).

B.2.3 Grade 300 UB Flange (IB-F)

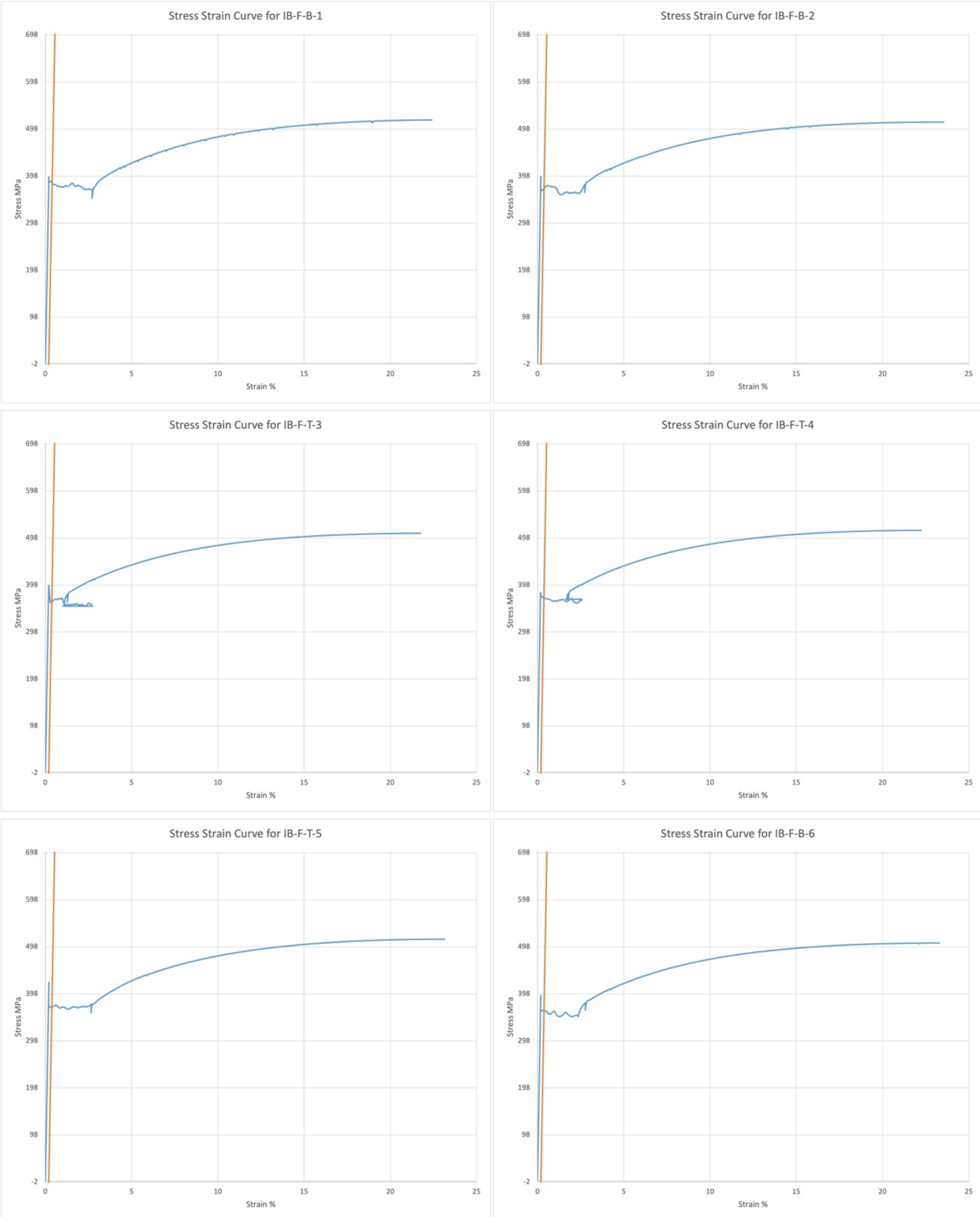

Figure B. 5: Individual stress-strain profiles with 0.2% offset line for Grade 300 UB Flange (IB-F) tensile specimens (1-6).

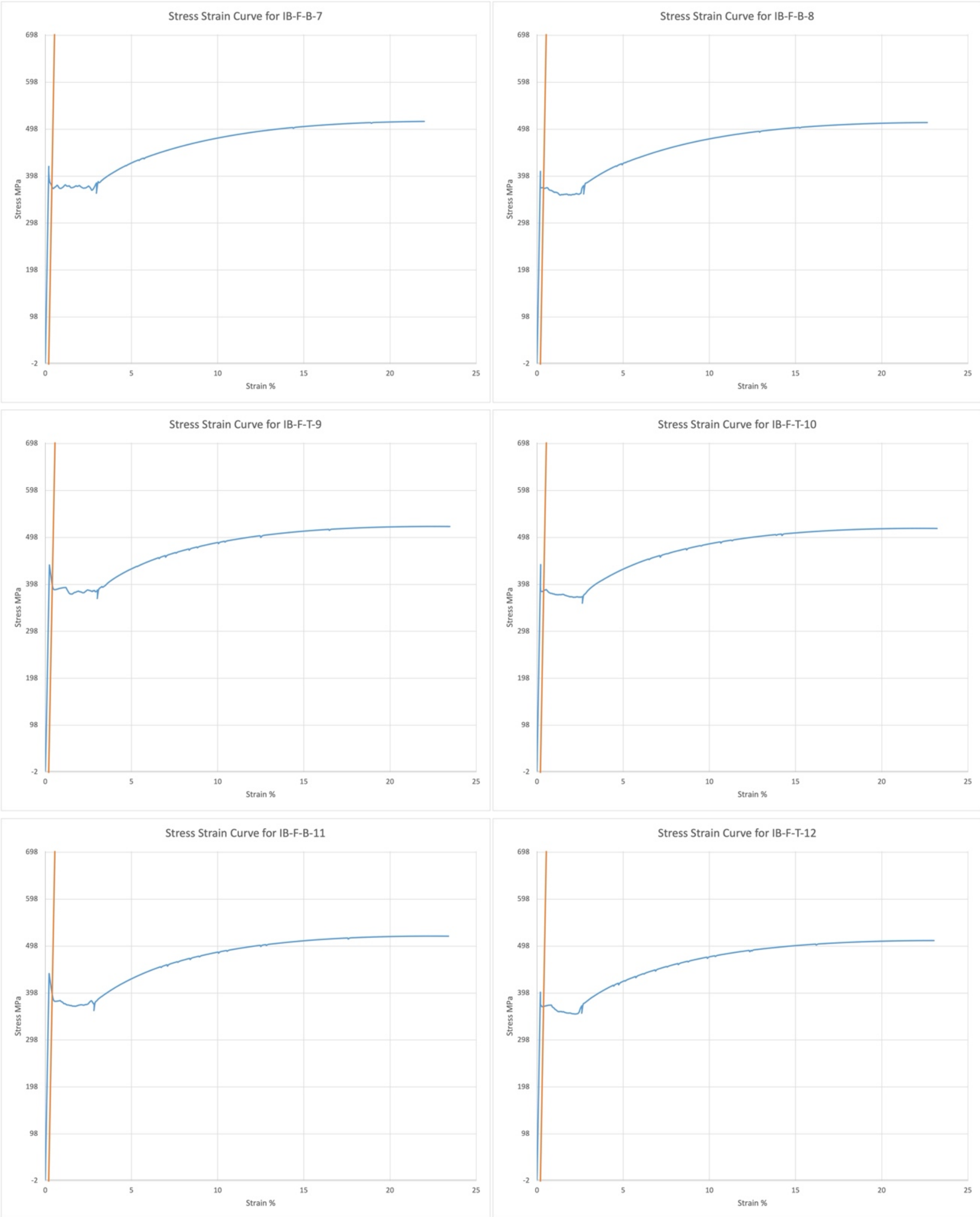

Figure B. 6: Individual stress-strain profiles with 0.2% offset line for Grade 300 UB Flange (IB-F) tensile specimens (7-12).

Appendix C: Non-Destructive Hardness Logs

Table C. 1: Master Data Log (NDT results).

Specimen	Rockwell (mean)	Vickers (mean)	Leeb (mean)	Brinell (mean)
SQ-1	88.93	180.10	229.20	214.57
SQ-2	89.14	182.06	252.40	226.26
SQ-3	88.70	183.66	462.20	208.14
SQ-4	89.97	186.86	464.40	224.81
IB-W-MT-1	86.93	197.12	254.00	202.08
IB-W-MB-2	87.08	203.78	240.60	206.26
IB-W-T-3	85.26	194.64	440.20	197.58
IB-W-MT-4	86.51	194.88	450.60	212.68
IB-W-M-5	89.00	207.01	452.80	204.08
IB-F-B-1	78.97	170.78	407.40	171.17
IB-F-B-2	79.18	169.32	400.20	169.05
SQ-5	88.34	186.42	461.40	227.93
SQ-6	87.92	182.96	460.20	224.45
SQ-7	88.50	184.04	460.60	221.76
IB-W-MB-6	88.56	197.82	449.20	212.10
IB-W-B-7	86.59	190.66	439.40	205.09
IB-W-MT-8	88.96	207.80	460.60	213.85
IB-F-T-3	77.57	165.16	399.00	171.54
IB-F-T-4	79.80	170.02	401.40	164.34
SQ-8	90.62	188.68	471.40	230.03
SQ-9	89.51	188.22	459.40	217.89
SQ-10	90.46	198.24	467.60	222.57
SQ-11	89.31	181.44	462.40	211.56
SQ-12	88.93	184.44	464.00	227.19
SQ-13	90.09	191.06	463.80	230.88

IB-W-MB-9	88.96	202.54	456.80	225.44
IB-W-MB-10	88.28	203.78	447.80	214.93
IB-W-MT-11	89.95	199.16	451.80	224.05
IB-F-T-5	79.07	169.06	403.80	176.06
IB-F-B-6	77.75	166.62	396.40	174.22
IB-F-B-7	80.35	163.52	397.40	173.53
IB-F-B-8	76.45	162.52	396.80	177.76
IB-F-T-9	80.67	167.42	400.80	183.06
IB-F-T-10	79.82	161.31	399.40	178.30
IB-F-B-11	80.75	164.52	397.40	171.41
IB-F-T-12	80.27	160.10	398.40	177.38

Table C. 2: Rockwell Hardness Raw Data log.

Rockwell Hardness (HRB)	1	2	3	4	5	AVG	STDEV	Error %
SQ-1	87.39	89.04	89.68	89.36	89.17	88.93	0.89	1.0
SQ-2	88.01	89.29	88.75	89.9	89.74	89.14	0.77	0.9
SQ-3	87.15	89.72	89.4	89.09	88.13	88.70	1.05	1.2
SQ-4	90.04	89.93	90.13	90.15	89.59	89.97	0.23	0.3
IB-W-MT-1	87.62	84.54	87.44	87.6	87.46	86.93	1.34	1.5
IB-W-MB-2	84.09	87.07	87.62	88.37	88.23	87.08	1.75	2.0
IB-W-T-3	84.04	84.01	87.53	86.13	84.61	85.26	1.53	1.8
IB-W-MT-4	83.91	87.51	85.99	87.95	87.18	86.51	1.62	1.9
IB-W-M-5	89.54	88.95	88.19	88.96	89.34	89.00	0.52	0.6
IB-F-B-1	78.96	76.94	79.21	80.07	79.67	78.97	1.21	1.5
IB-F-B-2	78.09	79.71	79.43	79.41	79.27	79.18	0.63	0.8
SQ-5	88.54	89.16	87.14	87.31	89.54	88.34	1.08	1.2
SQ-6	84.39	89.79	86.79	88.85	89.79	87.92	2.32	2.6
SQ-7	88.24	88.79	88.13	88.46	88.86	88.50	0.32	0.4
IB-W-MB-6	88.63	89.18	87.76	88.51	88.72	88.56	0.51	0.6
IB-W-B-7	84.07	88.12	87.51	87.13	86.13	86.59	1.58	1.8
IB-W-MT-8	89.04	87.37	89.31	90.13	88.94	88.96	1.00	1.1
IB-F-T-3	78.22	75.53	77.85	77.64	78.61	77.57	1.20	1.5
IB-F-T-4	79.86	80.16	78.83	80.37	79.8	79.80	0.59	0.7
SQ-8	89.98	90.39	91.22	90.74	90.78	90.62	0.46	0.5
SQ-9	89.19	89.23	89.75	90.07	89.31	89.51	0.38	0.4
SQ-10	89.92	90.39	89.64	90.93	91.44	90.46	0.73	0.8
SQ-11	88.83	88.34	88.48	90.02	90.86	89.31	1.09	1.2
SQ-12	87.96	89.29	89	89.63	88.77	88.93	0.63	0.7
SQ-13	92.11	88	88.25	91.76	90.32	90.09	1.92	2.1
IB-W-MB-9	88.92	87.57	90.03	89.4	88.86	88.96	0.91	1.0
IB-W-MB-10	87.57	87.81	87.99	88.84	89.19	88.28	0.70	0.8

IB-W-MT-11	89.9	89.71	90.03	90.06	90.04	89.95	0.15	0.2
IB-F-T-5	78.54	79.75	79.41	79	78.66	79.07	0.51	0.6
IB-F-B-6	76.84	78.01	77.39	78.29	78.2	77.75	0.62	0.8
IB-F-B-7	80.95	80.27	80	80.05	80.5	80.35	0.39	0.5
IB-F-B-8	75.44	77.14	79.26	77.35	73.04	76.45	2.34	3.1
IB-F-T-9	79.61	80.89	81.03	81.19	80.64	80.67	0.63	0.8
IB-F-T-10	77.53	79.99	80.2	80.63	80.76	79.82	1.32	1.7
IB-F-B-11	81.12	80.9	80.63	81.09	80.03	80.75	0.45	0.6
IB-F-T-12	79.8	80.67	79.57	80.36	80.93	80.27	0.57	0.7

Table C. 3: Brinell Hardness Raw Data Log.

Brinell (HB)	1	2	3	4	5	AVG	STDEV	Error %
SQ-1	218.63	210.3	214.68	212.1	217.12	214.57	3.44	1.6
SQ-2	216.1	215.75	233.2	233.2	233.05	226.26	9.44	4.2
SQ-3	213.26	188.53	216.13	211.74	211.02	208.14	11.13	5.3
SQ-4	219.1	227.8	229.69	231.17	216.29	224.81	6.68	3.0
IB-W-MT-1	200.72	206.13	212.88	193.89	196.78	202.08	7.58	3.8
IB-W-MB-2	210.53	212.32	204.97	199.84	203.66	206.26	5.11	2.5
IB-W-T-3	191.15	196.99	200.62	191.05	208.08	197.58	7.14	3.6
IB-W-MT-4	210.02	213.33	217.2	211.99	210.86	212.68	2.82	1.3
IB-W-M-5	202.79	206.12	197.79	208.9	204.82	204.08	4.16	2.0
IB-F-B-1	172.23	168.34	175.35	170.44	169.49	171.17	2.74	1.6
IB-F-B-2	169.61	169.74	162.73	170.79	172.36	169.05	3.70	2.2
SQ-5	227.45	227.75	224.22	230.45	229.77	227.93	2.44	1.1
SQ-6	223.27	224.52	226.71	222.75	225	224.45	1.56	0.7
SQ-7	220.34	225.71	220.21	221.29	221.23	221.76	2.27	1.0
IB-W-MB-6	203.16	212.37	211.24	215.17	218.57	212.10	5.75	2.7
IB-W-B-7	202.58	207.55	202.15	204.74	208.45	205.09	2.85	1.4
IB-W-MT-8	215.81	220.96	215.7	209.72	207.06	213.85	5.50	2.6
IB-F-T-3	170.3	170.2	173.3	169.89	174.03	171.54	1.96	1.1
IB-F-T-4	159.5	167.27	159.7	166.42	168.81	164.34	4.41	2.7
SQ-8	234.62	231.92	220.29	225.23	238.07	230.03	7.20	3.1
SQ-9	220.35	215.75	214.74	220.77	217.82	217.89	2.69	1.2
SQ-10	227.56	233.26	223.74	206.89	221.38	222.57	9.85	4.4
SQ-11	186.74	210.01	224.05	225.34	211.67	211.56	15.53	7.3
SQ-12	234.21	220.86	233.8	224.74	222.32	227.19	6.38	2.8
SQ-13	229.73	233.19	223.09	228.18	240.19	230.88	6.35	2.8
IB-W-MB-9	227.69	226.71	227.94	226.46	218.41	225.44	3.98	1.8
IB-W-MB-10	216.15	218.88	205.81	215.81	217.98	214.93	5.25	2.4

IB-W-MT-11	229.4	223.78	228.86	216.14	222.06	224.05	5.44	2.4
IB-F-T-5	177.28	173.65	174	177.08	178.27	176.06	2.09	1.2
IB-F-B-6	172.54	177.24	171.81	175.22	174.31	174.22	2.17	1.2
IB-F-B-7	173.6	171.14	176.85	173.36	172.69	173.53	2.09	1.2
IB-F-B-8	175.9	177.12	178.23	178.82	178.71	177.76	1.24	0.7
IB-F-T-9	182.5	183.4	185.1	179.1	185.22	183.06	2.50	1.4
IB-F-T-10	180.61	180.07	174.97	180.06	175.8	178.30	2.69	1.5
IB-F-B-11	180.24	170.13	170.78	173.63	162.28	171.41	6.49	3.8
IB-F-T-12	181.84	176.99	174.9	176.95	176.21	177.38	2.63	1.5

Table C. 4: Vickers Hardness Raw Data Log.

Vickers (HV)	1	2	3	4	5	AVG	STDEV	Error %
SQ-1	189.6	182.6	181.7	178.4	168.2	180.10	7.80	4.3
SQ-2	173.8	184.6	182.9	184.7	184.3	182.06	4.67	2.6
SQ-3	182.8	183.8	186.7	183.6	181.4	183.66	1.94	1.1
SQ-4	190.4	194.6	180.8	183.02	185.5	186.86	5.61	3.0
IB-W-MT-1	196.8	197.3	199.4	195.1	197	197.12	1.54	0.8
IB-W-MB-2	203.6	196.6	209.6	196.5	212.6	203.78	7.35	3.6
IB-W-T-3	193	200.7	195.8	189.9	193.8	194.64	4.00	2.1
IB-W-MT-4	195.6	192.1	198.4	193.8	194.5	194.88	2.34	1.2
IB-W-M-5	207.4	209.05	201.4	206.4	210.8	207.01	3.55	1.7
IB-F-B-1	173.1	168.4	172.8	167.3	172.3	170.78	2.72	1.6
IB-F-B-2	166.9	163.39	172.4	169.12	174.8	169.32	4.49	2.7
SQ-5	188.6	191.7	182.6	184.8	184.4	186.42	3.67	2.0
SQ-6	181.8	180.7	182.9	184.3	185.1	182.96	1.79	1.0
SQ-7	186.4	185	183.5	182.3	183	184.04	1.65	0.9
IB-W-MB-6	196.5	198.3	195.8	201.4	197.1	197.82	2.20	1.1
IB-W-B-7	192.4	191	189	186.5	194.4	190.66	3.05	1.6
IB-W-MT-8	205.8	205.5	211.3	209.2	207.2	207.80	2.44	1.2
IB-F-T-3	162	166.3	165.1	164.8	167.6	165.16	2.08	1.3
IB-F-T-4	171.2	166.6	170.5	171.4	170.4	170.02	1.96	1.2
SQ-8	190.8	191.1	190.5	189.8	181.2	188.68	4.21	2.2
SQ-9	187.2	185.9	187.4	187.9	192.7	188.22	2.61	1.4
SQ-10	199.8	194	201.8	196.8	198.8	198.24	2.98	1.5
SQ-11	184.4	180	178.4	180.6	183.8	181.44	2.57	1.4
SQ-12	181.4	189.6	186.8	180.4	184	184.44	3.81	2.1
SQ-13	194.7	188.3	190.8	190.6	190.9	191.06	2.30	1.2
IB-W-MB-9	207	205.7	203.5	198.6	197.9	202.54	4.12	2.0
IB-W-MB-10	207.4	203.5	202.4	203.8	201.8	203.78	2.18	1.1

IB-W-MT-11	198.7	195.4	197.2	198.8	205.7	199.16	3.91	2.0
IB-F-T-5	171.1	170.5	166.9	166.3	170.5	169.06	2.27	1.3
IB-F-B-6	165.6	164.9	167.6	168.5	166.5	166.62	1.46	0.9
IB-F-B-7	161.3	164.8	164.7	164.1	162.7	163.52	1.50	0.9
IB-F-B-8	160.08	162.8	165.4	164.9	159.4	162.52	2.73	1.7
IB-F-T-9	167.5	167.8	164.8	166.8	170.2	167.42	1.94	1.2
IB-F-T-10	161.5	160.05	165.3	156.8	162.9	161.31	3.18	2.0
IB-F-B-11	167.3	163.1	159.6	165.8	166.8	164.52	3.19	1.9
IB-F-T-12	157.9	165.8	161.4	156.6	158.8	160.10	3.64	2.3

Table C. 5: Leeb Hardness Raw Data Log.

Leeb	1	2	3	4	5	AVG	STDEV	Error %
SQ-1	274	250	172	264	186	229.20	46.87	20.5
SQ-2	260	287	269	243	203	252.40	31.86	12.6
SQ-3	463	459	461	463	465	462.20	2.28	0.5
SQ-4	469	460	463	464	466	464.40	3.36	0.7
IB-W-MT-1	282	276	274	226	212	254.00	32.47	12.8
IB-W-MB-2	279	217	260	229	218	240.60	27.63	11.5
IB-W-T-3	441	442	439	442	437	440.20	2.17	0.5
IB-W-MT-4	456	450	450	448	449	450.60	3.13	0.7
IB-W-M-5	453	453	454	451	453	452.80	1.10	0.2
IB-F-B-1	407	406	406	409	409	407.40	1.52	0.4
IB-F-B-2	401	400	402	398	400	400.20	1.48	0.4
SQ-5	467	462	458	461	459	461.40	3.51	0.8
SQ-6	464	459	461	458	459	460.20	2.39	0.5
SQ-7	465	462	461	455	460	460.60	3.65	0.8
IB-W-MB-6	447	445	453	448	453	449.20	3.63	0.8
IB-W-B-7	440	437	437	441	442	439.40	2.30	0.5
IB-W-MT-8	458	459	463	464	459	460.60	2.70	0.6
IB-F-T-3	398	399	397	402	399	399.00	1.87	0.5
IB-F-T-4	400	398	402	406	401	401.40	2.97	0.7
SQ-8	479	477	464	471	466	471.40	6.58	1.4
SQ-9	458	460	460	464	455	459.40	3.29	0.7
SQ-10	465	467	464	473	469	467.60	3.58	0.8
SQ-11	460	463	459	460	470	462.40	4.51	1.0
SQ-12	463	458	464	465	470	464.00	4.30	0.9
SQ-13	469	462	461	469	458	463.80	4.97	1.1
IB-W-MB-9	453	450	462	455	464	456.80	5.97	1.3
IB-W-MB-10	451	444	450	448	446	447.80	2.86	0.6

IB-W-MT-11	444	455	451	457	452	451.80	4.97	1.1
IB-F-T-5	402	405	399	406	407	403.80	3.27	0.8
IB-F-B-6	393	400	395	398	396	396.40	2.70	0.7
IB-F-B-7	400	396	394	400	397	397.40	2.61	0.7
IB-F-B-8	393	399	397	398	397	396.80	2.28	0.6
IB-F-T-9	401	394	403	402	404	400.80	3.96	1.0
IB-F-T-10	396	399	403	401	398	399.40	2.70	0.7
IB-F-B-11	400	401	391	400	395	397.40	4.28	1.1
IB-F-T-12	394	400	399	397	402	398.40	3.05	0.8

Appendix D: Surface Topography Logs

Table D. 1: The Raw R_a Roughness Table

S/N	Specimen	Roughness R_a (μm)
1	IB-F-B-1	0.16
2	IB-F-B-2	0.263
3	IB-F-T-3	0.213
4	IB-F-T-4	0.272
5	IB-F-T-5	0.361
6	IB-F-B-6	0.316
7	IB-F-B-7	0.201
8	IB-F-B-8	0.262
9	IB-F-T-9	0.277
10	IB-F-T-10	0.272
11	IB-F-B-11	0.203
12	IB-F-T-12	0.195
13	IB-W-MT-1	0.136
14	IB-W-MB-2	0.233
15	IB-W-T-3	0.172
16	IB-W-MT-4	0.193
17	IB-W-M-5	0.108
18	IB-W-MB-6	0.326
19	IB-W-B-7	0.355
20	IB-W-MT-8	0.333
21	IB-W-MB-9	0.268
22	IB-W-MB-10	0.228

23	IB-W-MT-11	0.246
24	SQ-1	0.283
25	SQ-2	0.2
26	SQ-3	0.259
27	SQ-4	0.247
28	SQ-5	0.334
29	SQ-6	0.149
30	SQ-7	0.236
31	SQ-8	0.353
32	SQ-9	0.295
33	SQ-10	0.28
34	SQ-11	0.262
35	SQ-12	0.279
36	SQ-13	0.127

Appendix E: Complete Micrographic and Chemical Profiles

Following E.1 to E.3 are pairs of the Scanning Electron Micrograph (SEM) and Energy Dispersive Spectroscopy (EDS) for the testing coupons.

E.1 Grade 300 Universal Beam (Web Extractions)

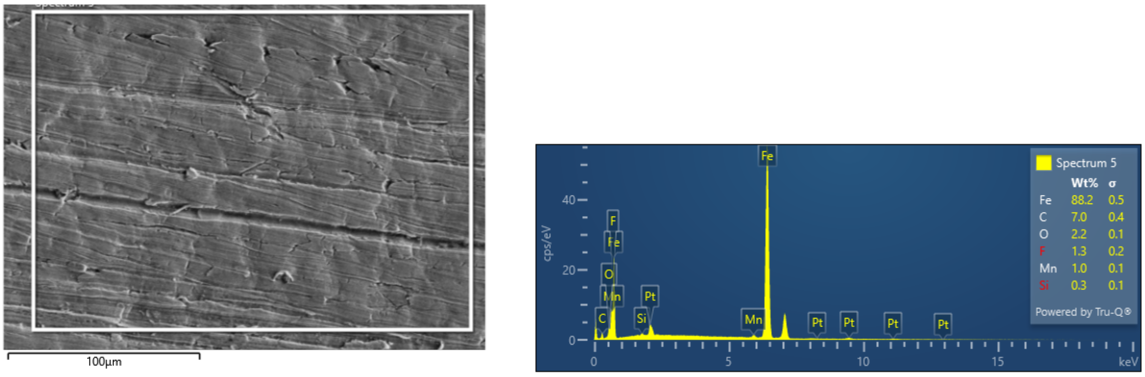

Figure E. 1: SEM and EDS for IB-W-T-3

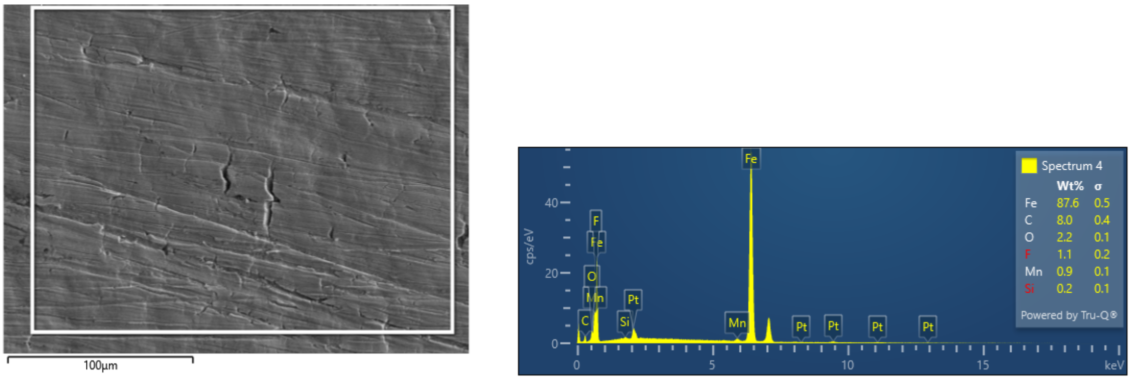

Figure E. 2:SEM and EDS for IB-W-M-5

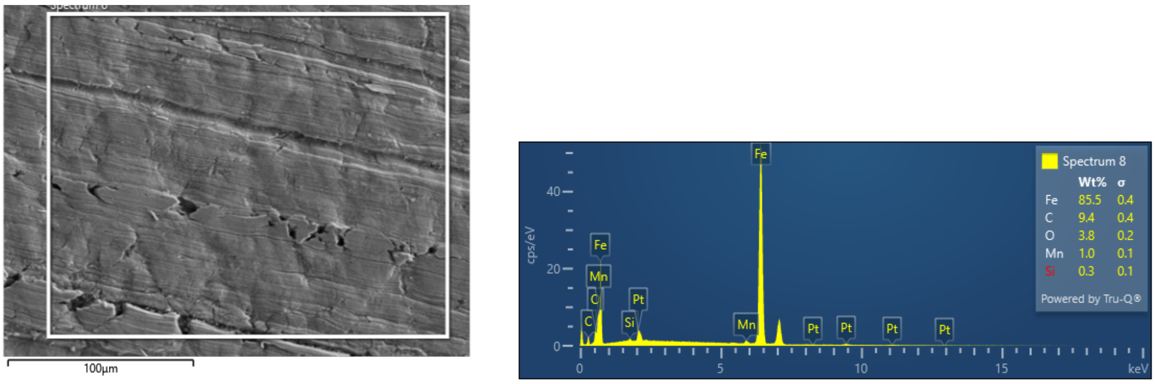

Figure E. 3: SEM and EDS for IB-W-B-7

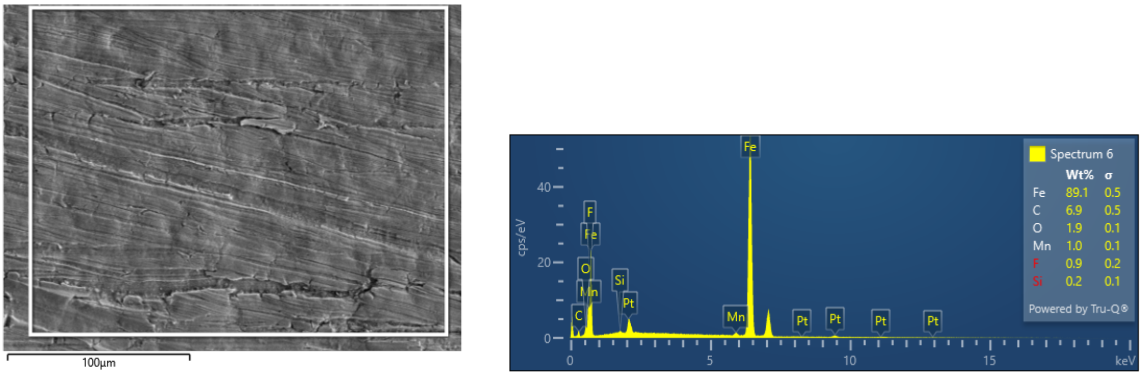

Figure E. 4: SEM and EDS for IB-W-MB-10

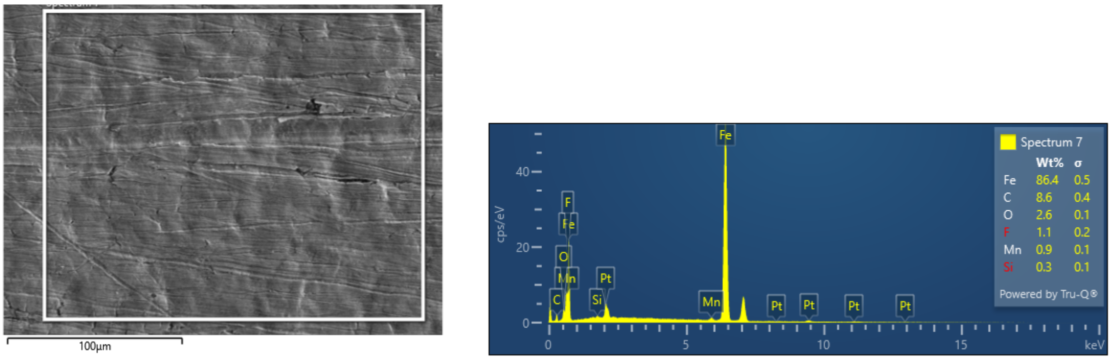

Figure E. 5: SEM and EDS for IB-W-MT-11

E.2 Grade 300 Universal Beam (Flange Extractions)

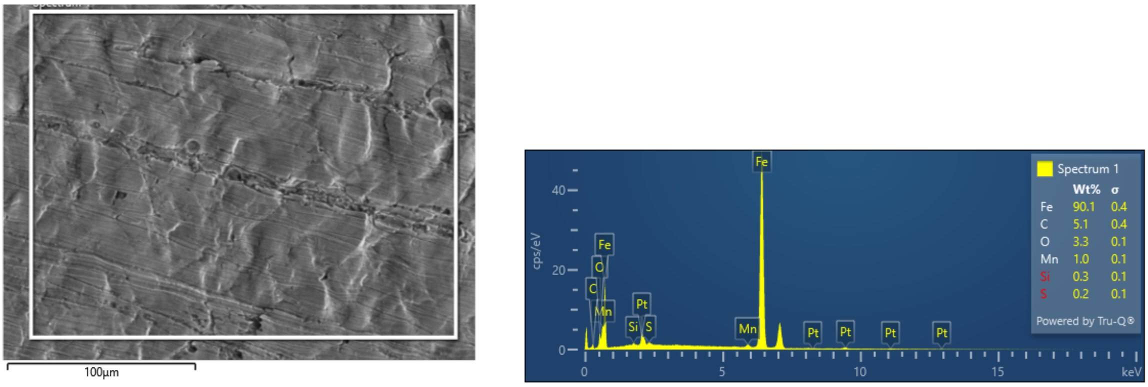

Figure E. 6: SEM and EDS for IB-F-T-3

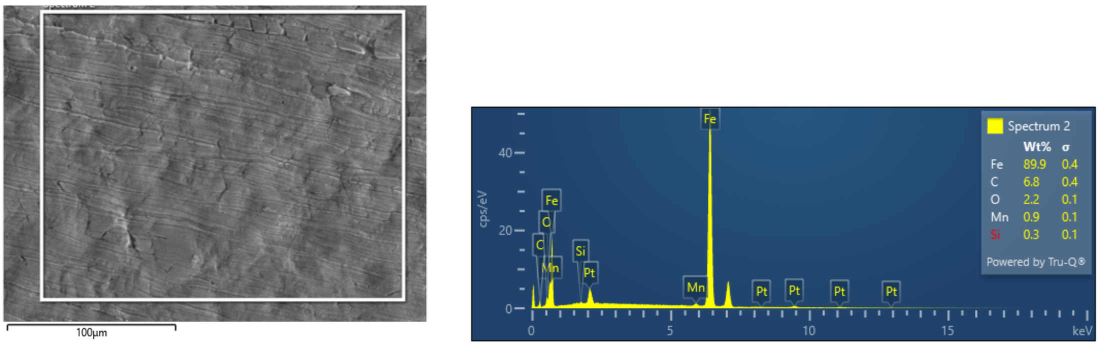

Figure E. 7: SEM and EDS for IB-F-B-11

E.3 Grade 350 Square Hollow Section (SHS)

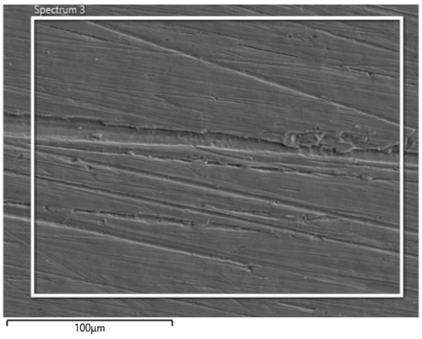

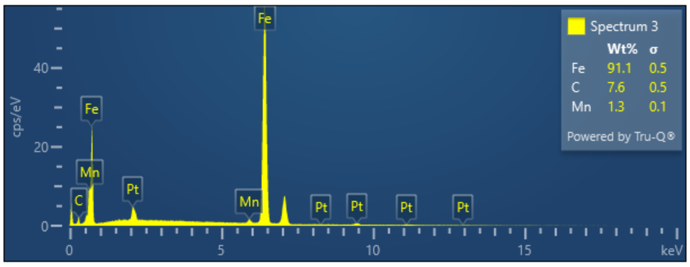

Figure E. 8: SEM and EDS for SQ-10

Appendix F: Predictive Linear Regression Models

F.1 Supplementary Linear Regression Models with Regression Formula

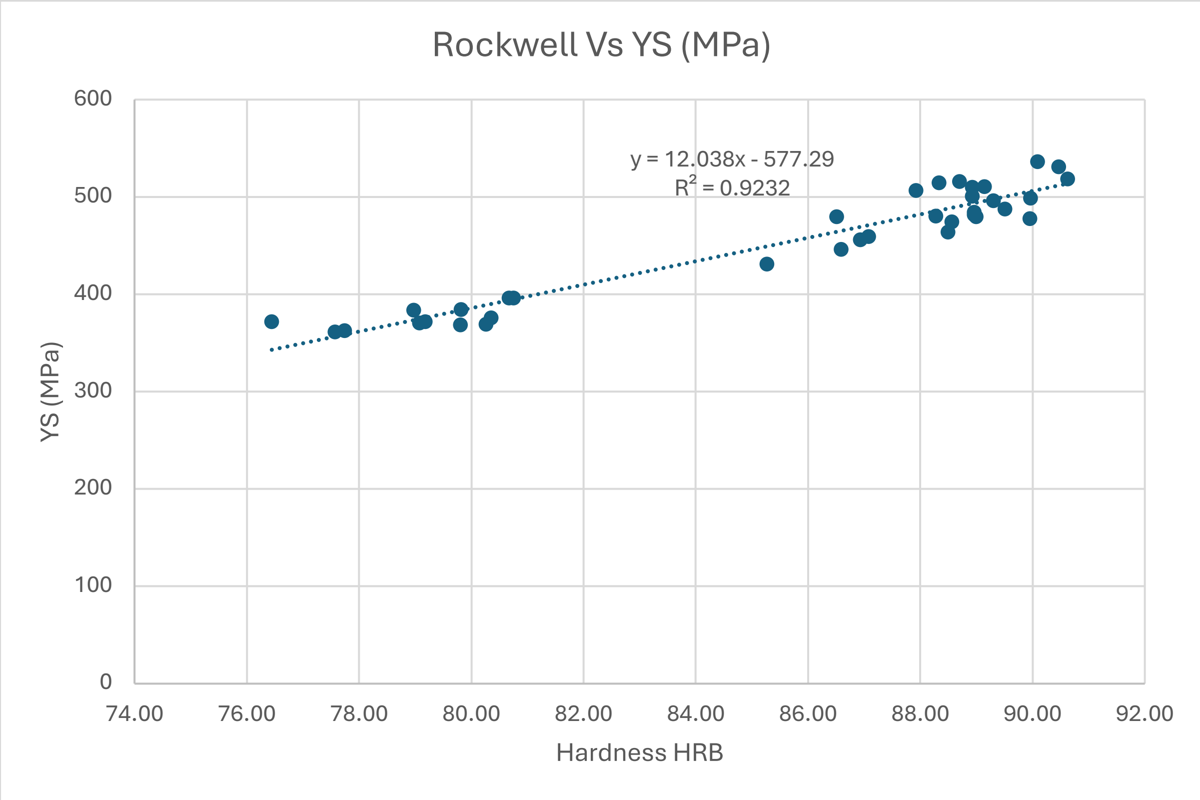

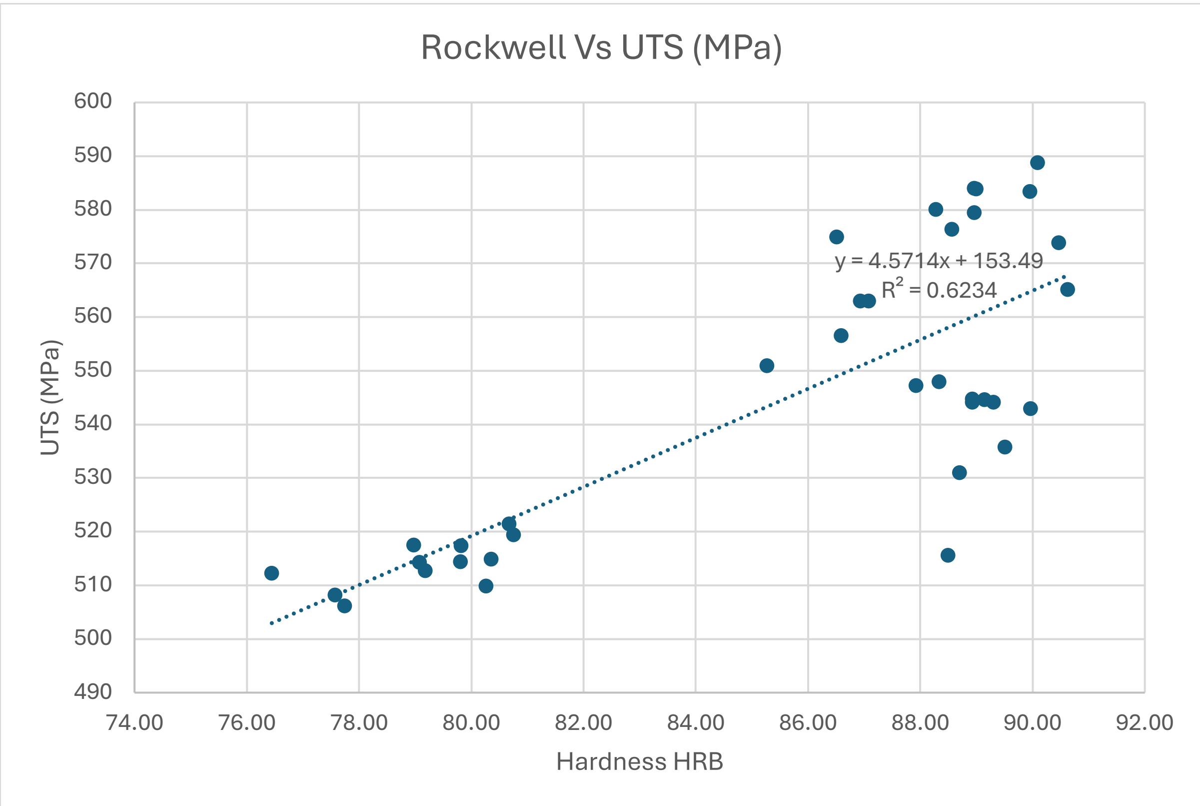

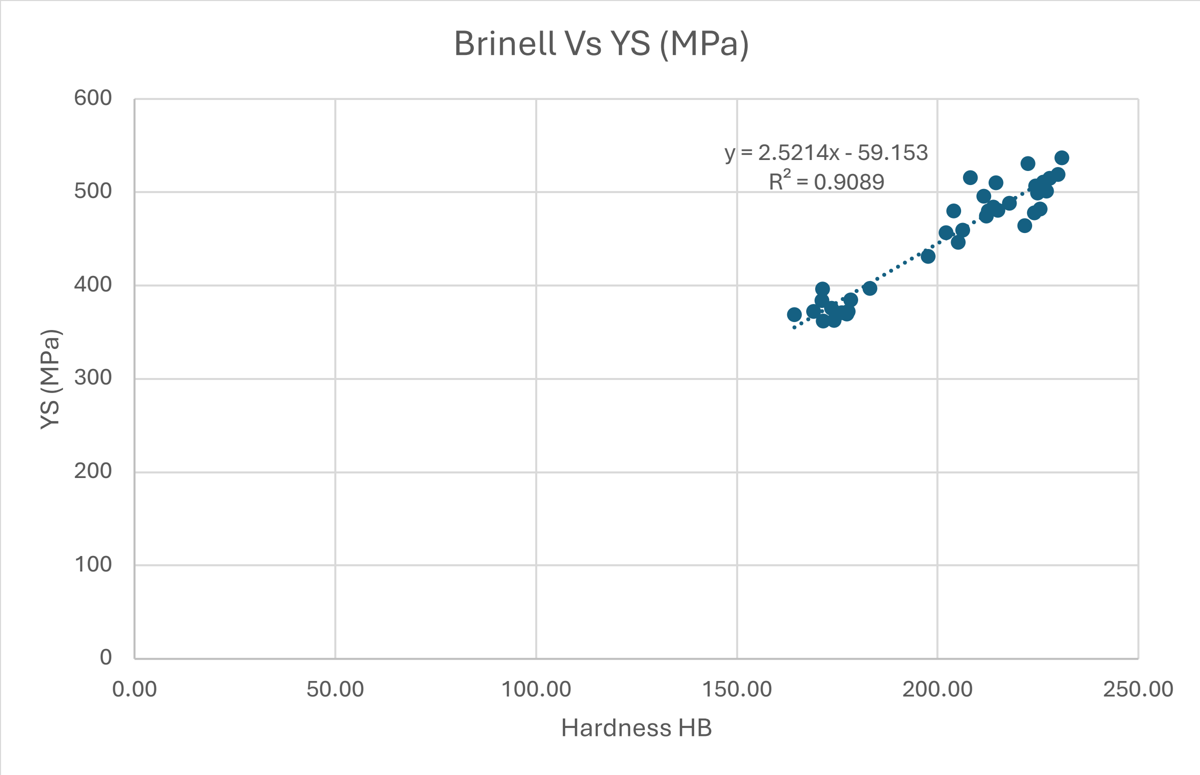
Brinell Vs YS (MPa)
y = 2.5214x - 59.153
R² = 0.9089
YS (MPa)
600
500
400
300
200
100
0
0.00
50.00
100.00
150.00
200.00
250.00
Hardness HB

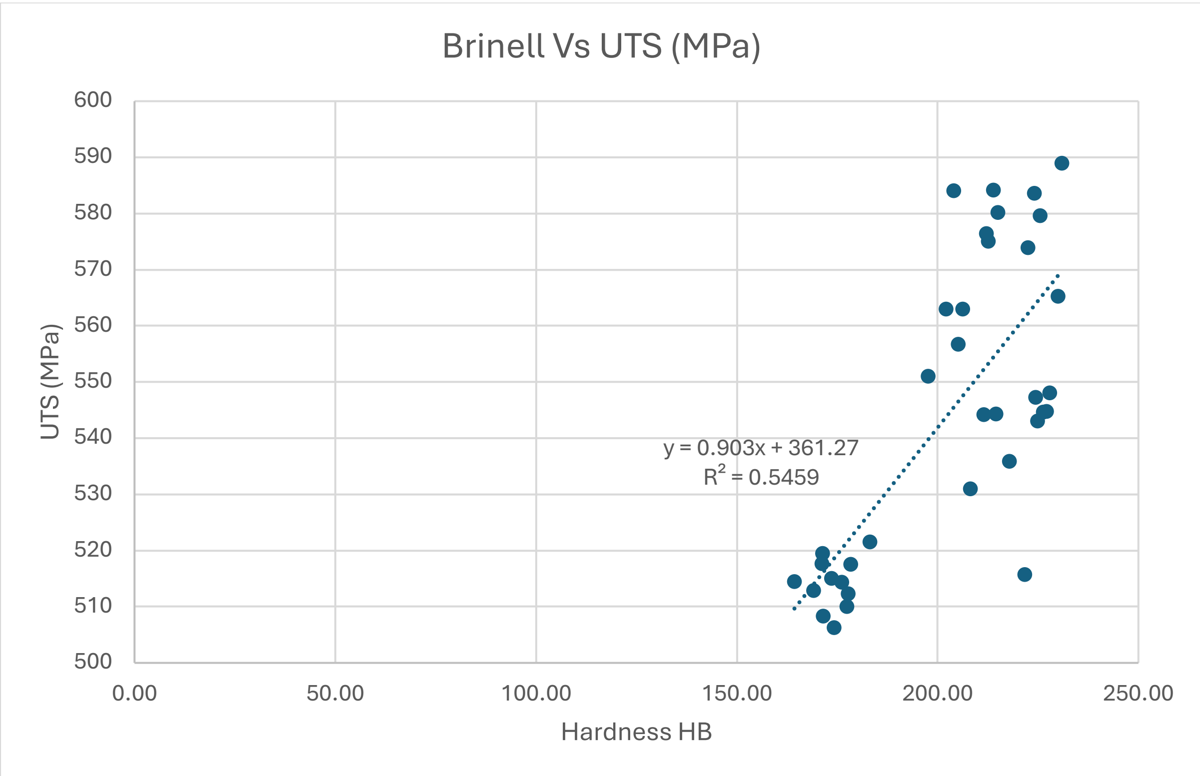
Brinell Vs UTS (MPa)
y = 0.903x + 361.27
R² = 0.5459
UTS (MPa)
600
590
580
570
560
550
540
530
520
510
500
0.00
50.00
100.00
150.00
200.00
250.00
Hardness HB

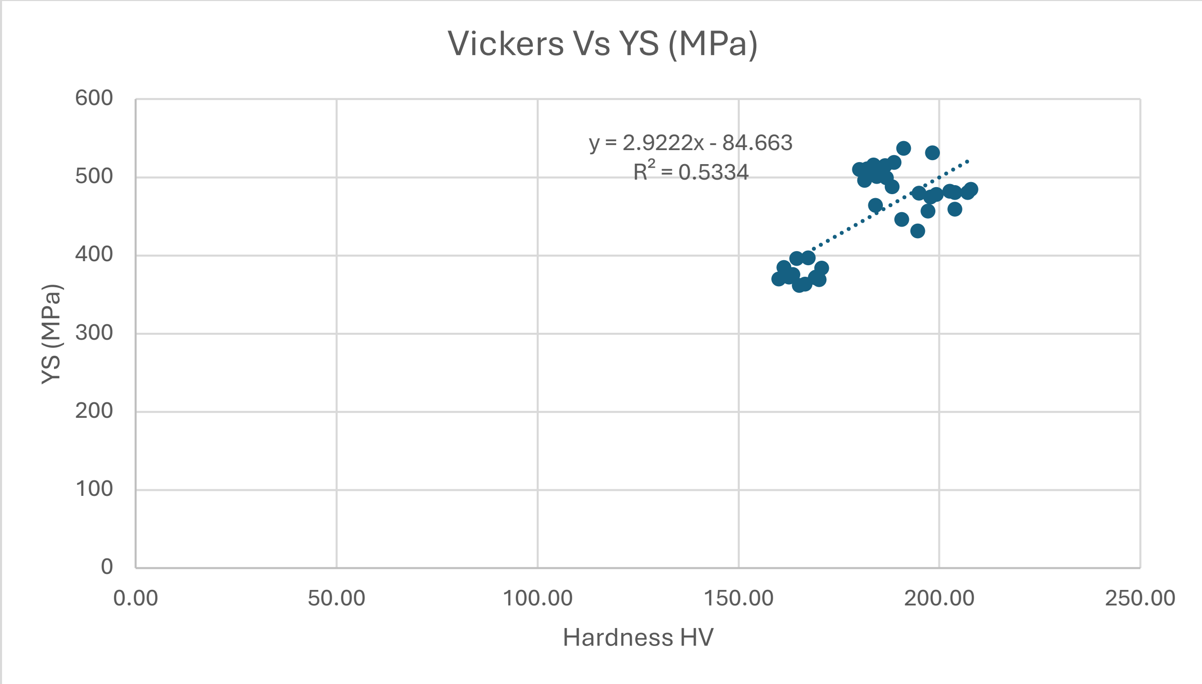
Vickers Vs YS (MPa)
y = 2.9222x - 84.663
R² = 0.5334
YS (MPa)
Hardness HV
0
100
200
300
400
500
600
0.00
50.00
100.00
150.00
200.00
250.00

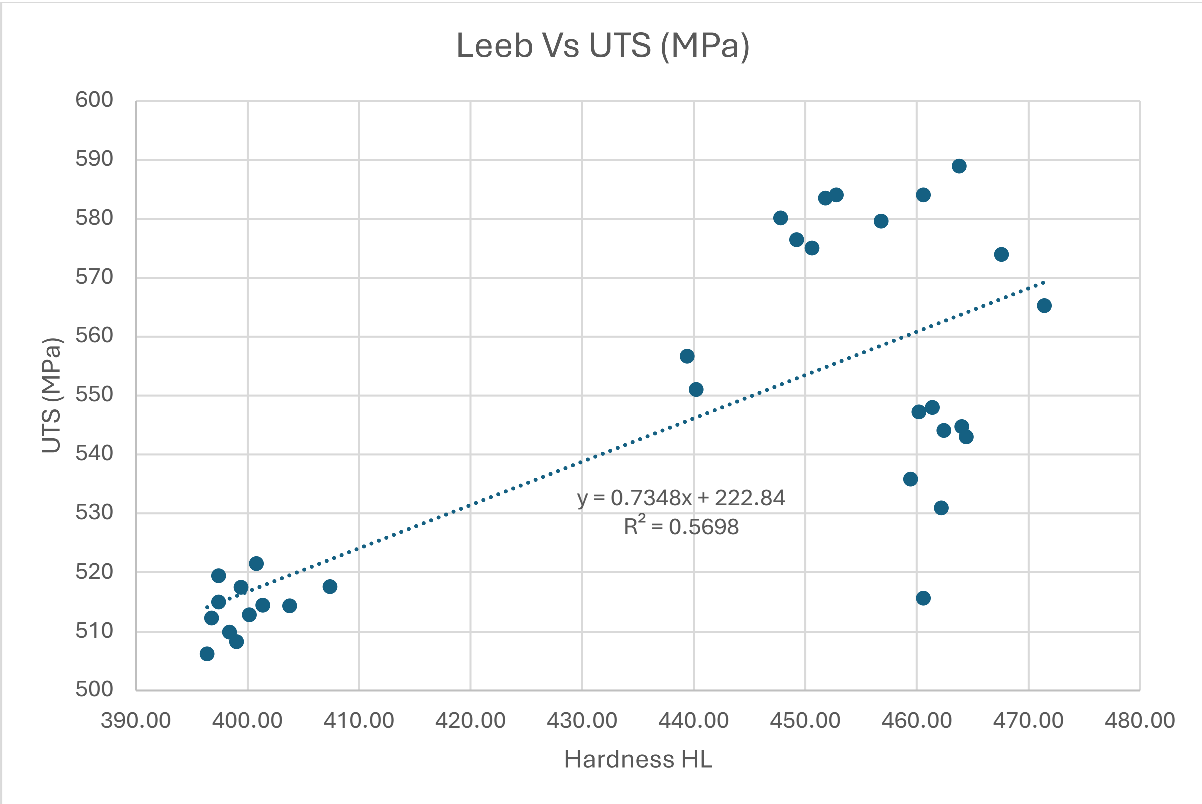
Leeb Vs UTS (MPa)
y = 0.7348x + 222.84
R² = 0.5698
UTS (MPa)
Hardness HL
500
510
520
530
540
550
560
570
580
590
600
390.00
400.00
410.00
420.00
430.00
440.00
450.00
460.00
470.00
480.00

F.2 Itemized Regression Error logs

Table F. 1: Rockwell Regression Error logs.

Specimen	Yield (MPa)	UTS (MPa)	Rockwell hardness	Yield (from Regression)	UTS (from Regression)	Squared Error (YS)	Squared Error (UTS)	Percentage Error (YS)	Percentage Error (UTS)	Residual Error (YS)	Residual Error (UTS)
SQ-1	510	544.24	88.93	493.23	560.02	281.39	248.87	3%	-3%	16.77	-15.78
SQ-2	511	544.67	89.14	495.75	560.98	232.46	265.87	3%	-3%	15.25	-16.31
SQ-3	516	531	88.70	490.46	558.96	652.47	781.99	5%	-5%	25.54	-27.96
SQ-4	499	543	89.97	505.74	564.77	45.49	473.92	-1%	-4%	-6.74	-21.77
IB-W-MT-1	456.46	563	86.93	469.20	550.89	162.24	146.63	-3%	2%	-12.74	12.11
IB-W-MB-2	459.23	563	87.08	470.93	551.55	136.91	131.12	-3%	2%	-11.70	11.45
IB-W-T-3	431.01	551	85.26	449.12	543.27	327.90	59.82	-4%	1%	-18.11	7.73
IB-W-MT-4	479.98	575	86.51	464.09	548.95	252.39	678.46	3%	5%	15.89	26.05
IB-W-M-5	480.05	584	89.00	494.04	560.33	195.83	560.44	-3%	4%	-13.99	23.67
IB-F-B-1	383.89	517.58	78.97	373.35	514.49	111.07	9.53	3%	1%	10.54	3.09
IB-F-B-2	372.05	512.8	79.18	375.90	515.46	14.84	7.09	-1%	-1%	-3.85	-2.66
SQ-5	514.8	548	88.34	486.12	557.32	822.38	86.83	6%	-2%	28.68	-9.32
SQ-6	506.9	547.29	87.92	481.12	555.42	664.86	66.04	5%	-1%	25.78	-8.13
SQ-7	464.13	515.7	88.50	488.02	558.04	570.96	1792.73	-5%	-8%	-23.89	-42.34
IB-W-MB-6	474.68	576.449	88.56	488.80	558.33	199.24	328.18	-3%	3%	-14.12	18.12
IB-W-B-7	446.11	556.64	86.59	465.10	549.34	360.79	53.34	-4%	1%	-18.99	7.30
IB-W-MT-8	484.21	584.1	88.96	493.59	560.15	87.92	573.48	-2%	4%	-9.38	23.95

IB-F-T-3	361.79	508.27	77.57	356.50	508.09	28.01	0.03	1%	0%	5.29	0.18
IB-F-T-4	369.02	514.429	79.80	383.39	518.31	206.51	15.03	-4%	-1%	-14.37	-3.88
SQ-8	519.02	565.22	90.62	513.62	567.76	29.19	6.45	1%	0%	5.40	-2.54
SQ-9	487.96	535.89	89.51	500.23	562.68	150.59	717.49	-3%	-5%	-12.27	-26.79
SQ-10	530.87	573.94	90.46	511.72	567.04	366.89	47.65	4%	1%	19.15	6.90
SQ-11	496.05	544.15	89.31	497.78	561.74	2.98	309.53	0%	-3%	-1.73	-17.59
SQ-12	500.92	544.76	88.93	493.25	560.02	58.84	233.01	2%	-3%	7.67	-15.26
SQ-13	536.68	588.88	90.09	507.19	565.32	869.70	555.15	5%	4%	29.49	23.56
IB-W-MB-9	482.02	579.57	88.96	493.56	560.14	133.23	377.39	-2%	3%	-11.54	19.43
IB-W-MB-10	480.77	580.12	88.28	485.42	557.05	21.67	532.08	-1%	4%	-4.65	23.07
IB-W-MT-11	478.16	583.52	89.95	505.50	564.68	747.70	355.01	-6%	3%	-27.34	18.84
IB-F-T-5	371.05	514.32	79.07	374.58	514.96	12.45	0.41	-1%	0%	-3.53	-0.64
IB-F-B-6	362.86	506.19	77.75	358.62	508.90	18.01	7.33	1%	-1%	4.24	-2.71
IB-F-B-7	375.79	514.98	80.35	390.01	520.82	202.25	34.11	-4%	-1%	-14.22	-5.84
IB-F-B-8	372.31	512.31	76.45	342.97	502.96	861.01	87.51	8%	2%	29.34	9.35
IB-F-T-9	396.7	521.53	80.67	393.84	522.27	8.18	0.55	1%	0%	2.86	-0.74
IB-F-T-10	384.36	517.47	79.82	383.61	518.39	0.57	0.84	0%	0%	0.75	-0.92
IB-F-B-11	396.08	519.46	80.75	394.83	522.65	1.57	10.17	0%	-1%	1.25	-3.19
IB-F-T-12	369.4	509.95	80.27	388.95	520.42	382.28	109.58	-5%	-2%	-19.55	-10.47

Table F. 2: Vickers Regression Error logs.

Specimen	Yield (MPa)	UTS (MPa)	Vickers Hardness	Yield (from Regression)	UTS (from Regression)	Squared Error (YS)	Squared Error (UTS)	Percentage Error (YS)	Percentage Error (UTS)	Residual Error (YS)	Residual Error (UTS)
SQ-1	510	544.24	180.10	441.63	538.38	4675.11	34.38	13%	1%	68.37	5.86
SQ-2	511	544.67	182.06	447.35	541.71	4050.97	8.75	12%	1%	63.65	2.96
SQ-3	516	531	183.66	452.03	544.43	4092.38	180.48	12%	-3%	63.97	-13.43
SQ-4	499	543	186.86	461.39	549.89	1414.44	47.42	8%	-1%	37.61	-6.89
IB-W-MT-1	456.46	563	197.12	491.36	567.34	1218.08	18.83	-8%	-1%	-34.90	-4.34
IB-W-MB-2	459.23	563	203.78	510.82	578.67	2661.83	245.62	-11%	-3%	-51.59	-15.67
IB-W-T-3	431.01	551	194.64	484.11	563.12	2820.04	146.87	-12%	-2%	-53.10	-12.12
IB-W-MT-4	479.98	575	194.88	484.82	563.53	23.38	131.62	-1%	2%	-4.84	11.47
IB-W-M-5	480.05	584	207.01	520.26	584.17	1616.97	0.03	-8%	0%	-40.21	-0.17
IB-F-B-1	383.89	517.58	170.78	414.39	522.52	930.27	24.37	-8%	-1%	-30.50	-4.94
IB-F-B-2	372.05	512.8	169.32	410.13	520.04	1450.07	52.35	-10%	-1%	-38.08	-7.24
SQ-5	514.8	548	186.42	460.09	549.13	2992.80	1.28	11%	0%	54.71	-1.13
SQ-6	506.9	547.29	182.96	449.98	543.24	3239.58	16.38	11%	1%	56.92	4.05
SQ-7	464.13	515.7	184.04	453.14	545.08	120.81	863.24	2%	-6%	10.99	-29.38
IB-W-MB-6	474.68	576.449	197.82	493.41	568.53	350.69	62.71	-4%	1%	-18.73	7.92
IB-W-B-7	446.11	556.64	190.66	472.48	556.35	695.57	0.09	-6%	0%	-26.37	0.29
IB-W-MT-8	484.21	584.1	207.80	522.57	585.51	1471.50	2.00	-8%	0%	-38.36	-1.41
IB-F-T-3	361.79	508.27	165.16	397.97	512.95	1308.82	21.93	-10%	-1%	-36.18	-4.68

IB-F-T-4	369.02	514.429	170.02	412.17	521.22	1861.87	46.16	-12%	-1%	-43.15	-6.79
SQ-8	519.02	565.22	188.68	466.70	552.98	2737.62	149.90	10%	2%	52.32	12.24
SQ-9	487.96	535.89	188.22	465.35	552.19	511.05	265.82	5%	-3%	22.61	-16.30
SQ-10	530.87	573.94	198.24	494.63	569.25	1313.05	22.04	7%	1%	36.24	4.69
SQ-11	496.05	544.15	181.44	445.54	540.66	2551.16	12.20	10%	1%	50.51	3.49
SQ-12	500.92	544.76	184.44	454.31	545.76	2172.72	1.00	9%	0%	46.61	-1.00
SQ-13	536.68	588.88	191.06	473.65	557.03	3972.46	1014.63	12%	5%	63.03	31.85
IB-W-MB-9	482.02	579.57	202.54	507.20	576.56	634.00	9.05	-5%	1%	-25.18	3.01
IB-W-MB-10	480.77	580.12	203.78	510.82	578.67	903.18	2.10	-6%	0%	-30.05	1.45
IB-W-MT-11	478.16	583.52	199.16	497.32	570.81	367.20	161.53	-4%	2%	-19.16	12.71
IB-F-T-5	371.05	514.32	169.06	409.36	519.59	1467.97	27.77	-10%	-1%	-38.31	-5.27
IB-F-B-6	362.86	506.19	166.62	402.23	515.44	1550.31	85.51	-11%	-2%	-39.37	-9.25
IB-F-B-7	375.79	514.98	163.52	393.18	510.16	302.24	23.21	-5%	1%	-17.39	4.82
IB-F-B-8	372.31	512.31	162.52	390.24	508.45	321.53	14.87	-5%	1%	-17.93	3.86
IB-F-T-9	396.7	521.53	167.42	404.57	516.80	61.96	22.39	-2%	1%	-7.87	4.73
IB-F-T-10	384.36	517.47	161.31	386.72	506.40	5.56	122.52	-1%	2%	-2.36	11.07
IB-F-B-11	396.08	519.46	164.52	396.10	511.86	0.00	57.70	0%	1%	-0.02	7.60
IB-F-T-12	369.4	509.95	160.10	383.18	504.34	189.92	31.45	-4%	1%	-13.78	5.61

Table F. 3: Brinell Regression Error Logs.

Specimen	Yield (MPa)	UTS (MPa)	Brinell Hardness	Yield (from Regression)	UTS (from Regression)	Squared Error (YS)	Squared Error (UTS)	Percentage Error (YS)	Percentage Error (UTS)	Residual Error (YS)	Residual Error (UTS)
SQ-1	510	544.24	214.57	481.85	555.02	792.21	116.28	6%	-2%	28.15	-10.78
SQ-2	511	544.67	226.26	511.34	565.58	0.11	437.34	0%	-4%	-0.34	-20.91
SQ-3	516	531	208.14	465.64	549.22	2536.02	331.85	10%	-3%	50.36	-18.22
SQ-4	499	543	224.81	507.68	564.27	75.39	452.56	-2%	-4%	-8.68	-21.27
IB-W-MT-1	456.46	563	202.08	450.37	543.75	37.07	370.63	1%	3%	6.09	19.25
IB-W-MB-2	459.23	563	206.26	460.92	547.53	2.86	239.43	0%	3%	-1.69	15.47
IB-W-T-3	431.01	551	197.58	439.02	539.68	64.16	128.08	-2%	2%	-8.01	11.32
IB-W-MT-4	479.98	575	212.68	477.10	553.32	8.30	470.02	1%	4%	2.88	21.68
IB-W-M-5	480.05	584	204.08	455.42	545.56	606.42	1477.80	5%	7%	24.63	38.44
IB-F-B-1	383.89	517.58	171.17	372.44	515.84	131.22	3.04	3%	0%	11.45	1.74
IB-F-B-2	372.05	512.8	169.05	367.08	513.92	24.71	1.25	1%	0%	4.97	-1.12
SQ-5	514.8	548	227.93	515.54	567.09	0.55	364.39	0%	-3%	-0.74	-19.09
SQ-6	506.9	547.29	224.45	506.78	563.95	0.02	277.50	0%	-3%	0.12	-16.66
SQ-7	464.13	515.7	221.76	499.98	561.52	1285.41	2099.08	-8%	-9%	-35.85	-45.82
IB-W-MB-6	474.68	576.449	212.10	475.64	552.80	0.92	559.36	0%	4%	-0.96	23.65
IB-W-B-7	446.11	556.64	205.09	457.97	546.47	140.68	103.43	-3%	2%	-11.86	10.17
IB-W-MT-8	484.21	584.1	213.85	480.05	554.38	17.32	883.48	1%	5%	4.16	29.72
IB-F-T-3	361.79	508.27	171.54	373.38	516.17	134.28	62.48	-3%	-2%	-11.59	-7.90

IB-F-T-4	369.02	514.429	164.34	355.21	509.67	190.61	22.66	4%	1%	13.81	4.76
SQ-8	519.02	565.22	230.03	520.83	568.98	3.29	14.16	0%	-1%	-1.81	-3.76
SQ-9	487.96	535.89	217.89	490.22	558.02	5.13	489.78	0%	-4%	-2.26	-22.13
SQ-10	530.87	573.94	222.57	502.02	562.25	832.04	136.72	5%	2%	28.85	11.69
SQ-11	496.05	544.15	211.56	474.28	552.31	473.96	66.59	4%	-1%	21.77	-8.16
SQ-12	500.92	544.76	227.19	513.67	566.42	162.66	469.11	-3%	-4%	-12.75	-21.66
SQ-13	536.68	588.88	230.88	522.98	569.75	187.75	365.92	3%	3%	13.70	19.13
IB-W-MB-9	482.02	579.57	225.44	509.28	564.84	742.91	216.85	-6%	3%	-27.26	14.73
IB-W-MB-10	480.77	580.12	214.93	482.76	555.35	3.97	613.64	0%	4%	-1.99	24.77
IB-W-MT-11	478.16	583.52	224.05	505.76	563.59	761.85	397.39	-6%	3%	-27.60	19.93
IB-F-T-5	371.05	514.32	176.06	384.75	520.25	187.82	35.15	-4%	-1%	-13.70	-5.93
IB-F-B-6	362.86	506.19	174.22	380.14	518.59	298.44	153.87	-5%	-2%	-17.28	-12.40
IB-F-B-7	375.79	514.98	173.53	378.38	517.97	6.71	8.91	-1%	-1%	-2.59	-2.99
IB-F-B-8	372.31	512.31	177.76	389.04	521.78	279.93	89.75	-4%	-2%	-16.73	-9.47
IB-F-T-9	396.7	521.53	183.06	402.42	526.58	32.77	25.47	-1%	-1%	-5.72	-5.05
IB-F-T-10	384.36	517.47	178.30	390.42	522.28	36.70	23.10	-2%	-1%	-6.06	-4.81
IB-F-B-11	396.08	519.46	171.41	373.05	516.06	530.60	11.59	6%	1%	23.03	3.40
IB-F-T-12	369.4	509.95	177.38	388.09	521.44	349.24	132.07	-5%	-2%	-18.69	-11.49

Table F. 4: Leeb Regression Error Logs.

Specimen	Yield (MPa)	UTS (MPa)	Leeb Hardness (mean)	Yield (from Regression)	UTS (from Regression)	Squared Error (YS)	Squared Error (UTS)	Percentage Error (YS)	Percentage Error (UTS)	Residual Error (YS)	Residual Error (UTS)
SQ-3	516	531	462.20	500.86	562.46	229.12	990.02	3%	-6%	15.14	-31.46
SQ-4	499	543	464.40	505.29	564.08	39.62	444.41	-1%	-4%	-6.29	-21.08
IB-W-T-3	431.01	551	440.20	456.55	546.30	652.33	22.10	-6%	1%	-25.54	4.70
IB-W-MT-4	479.98	575	450.60	477.50	553.94	6.16	443.49	1%	4%	2.48	21.06
IB-W-M-5	480.05	584	452.80	481.93	555.56	3.53	808.98	0%	5%	-1.88	28.44
IB-F-B-1	383.89	517.58	407.40	390.49	522.20	43.50	21.32	-2%	-1%	-6.60	-4.62
IB-F-B-2	372.05	512.8	400.20	375.98	516.91	15.47	16.87	-1%	-1%	-3.93	-4.11
SQ-5	514.8	548	461.40	499.25	561.88	241.74	192.56	3%	-3%	15.55	-13.88
SQ-6	506.9	547.29	460.20	496.83	560.99	101.31	187.83	2%	-3%	10.07	-13.70
SQ-7	464.13	515.7	460.60	497.64	561.29	1122.95	2078.35	-7%	-9%	-33.51	-45.59
IB-W-MB-6	474.68	576.449	449.20	474.68	552.91	0.00	553.98	0%	4%	0.00	23.54
IB-W-B-7	446.11	556.64	439.40	454.94	545.71	77.96	119.44	-2%	2%	-8.83	10.93
IB-W-MT-8	484.21	584.1	460.60	497.64	561.29	180.38	520.35	-3%	4%	-13.43	22.81
IB-F-T-3	361.79	508.27	399.00	373.57	516.03	138.67	60.14	-3%	-2%	-11.78	-7.76
IB-F-T-4	369.02	514.429	401.40	378.40	517.79	87.98	11.29	-3%	-1%	-9.38	-3.36
SQ-8	519.02	565.22	471.40	519.39	569.22	0.14	16.04	0%	-1%	-0.37	-4.00
SQ-9	487.96	535.89	459.40	495.22	560.41	52.76	601.09	-1%	-5%	-7.26	-24.52
SQ-10	530.87	573.94	467.60	511.74	566.43	365.96	56.36	4%	1%	19.13	7.51
SQ-11	496.05	544.15	462.40	501.27	562.61	27.21	340.83	-1%	-3%	-5.22	-18.46

SQ-12	500.92	544.76	464.00	504.49	563.79	12.74	362.03	-1%	-3%	-3.57	-19.03
SQ-13	536.68	588.88	463.80	504.09	563.64	1062.37	637.05	6%	4%	32.59	25.24
IB-W-MB-9	482.02	579.57	456.80	489.99	558.50	63.47	444.09	-2%	4%	-7.97	21.07
IB-W-MB-10	480.77	580.12	447.80	471.86	551.88	79.41	797.30	2%	5%	8.91	28.24
IB-W-MT-11	478.16	583.52	451.80	479.92	554.82	3.08	823.54	0%	5%	-1.76	28.70
IB-F-T-5	371.05	514.32	403.80	383.23	519.55	148.45	27.38	-3%	-1%	-12.18	-5.23
IB-F-B-6	362.86	506.19	396.40	368.33	514.11	29.91	62.80	-2%	-2%	-5.47	-7.92
IB-F-B-7	375.79	514.98	397.40	370.34	514.85	29.67	0.02	1%	0%	5.45	0.13
IB-F-B-8	372.31	512.31	396.80	369.13	514.41	10.08	4.40	1%	0%	3.18	-2.10
IB-F-T-9	396.7	521.53	400.80	377.19	517.35	380.59	17.49	5%	1%	19.51	4.18
IB-F-T-10	384.36	517.47	399.40	374.37	516.32	99.77	1.32	3%	0%	9.99	1.15
IB-F-B-11	396.08	519.46	397.40	370.34	514.85	662.39	21.26	6%	1%	25.74	4.61
IB-F-T-12	369.4	509.95	398.40	372.36	515.58	8.75	31.75	-1%	-1%	-2.96	-5.63

F.3 Supplementary Residual Plots

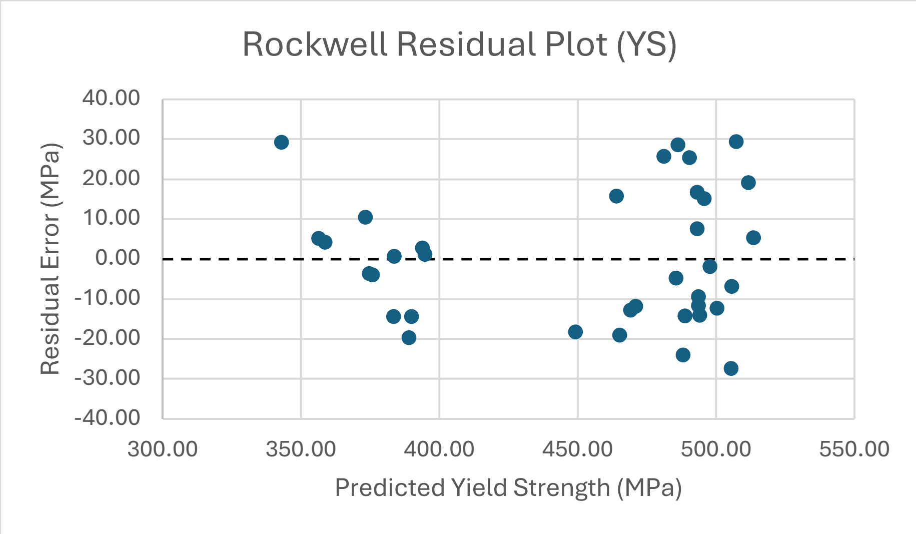

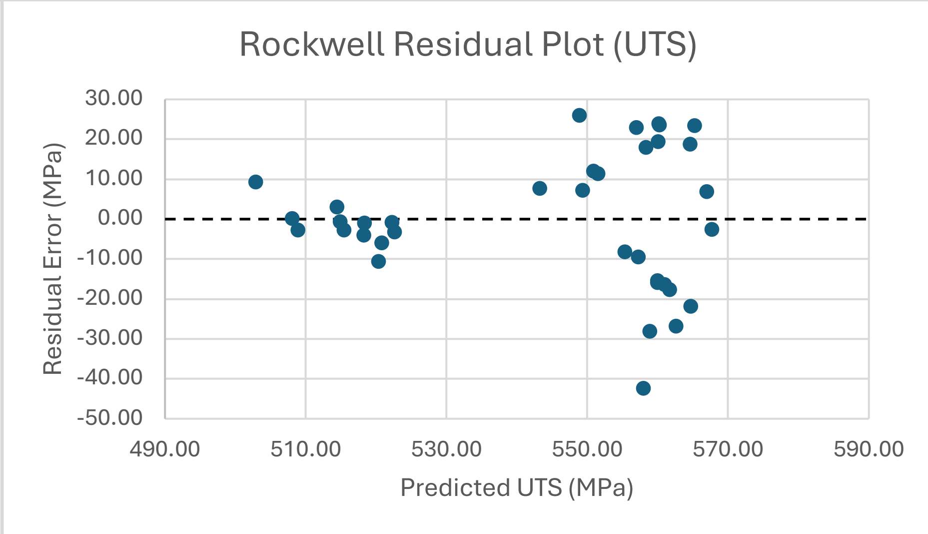

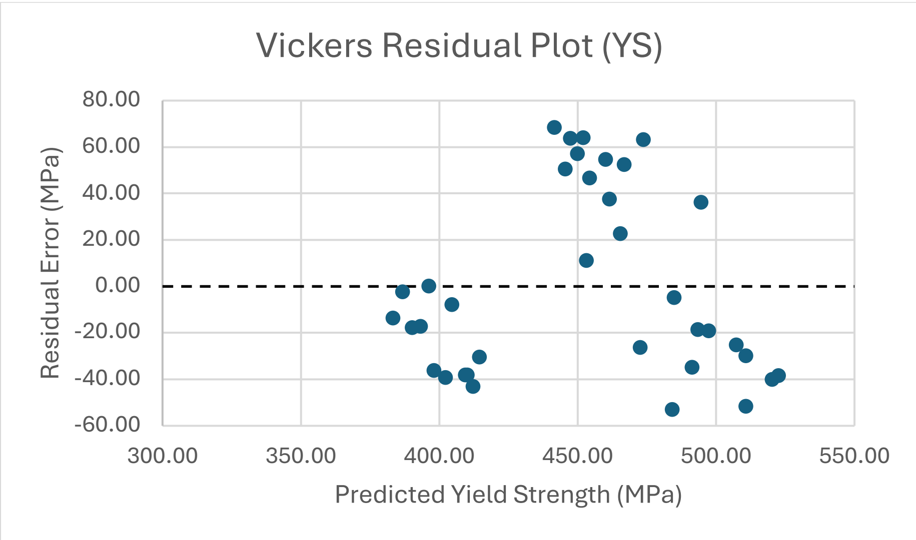

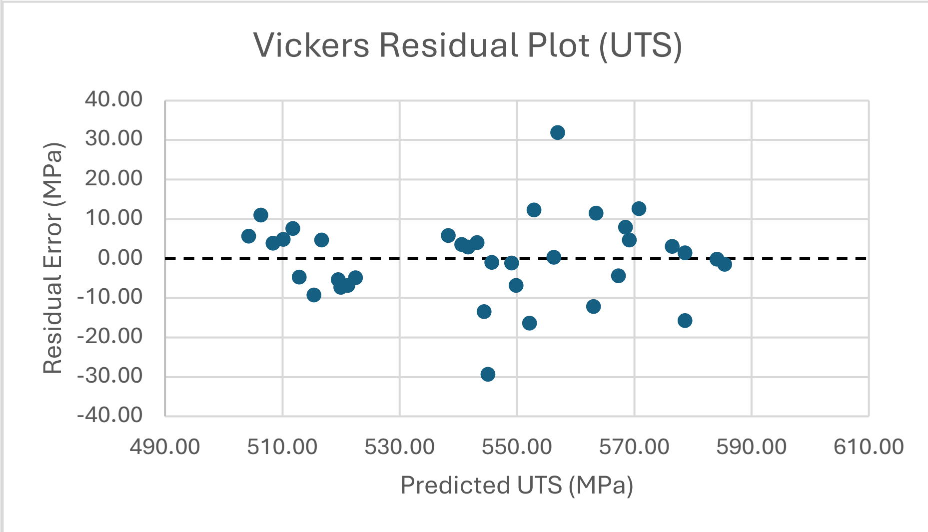

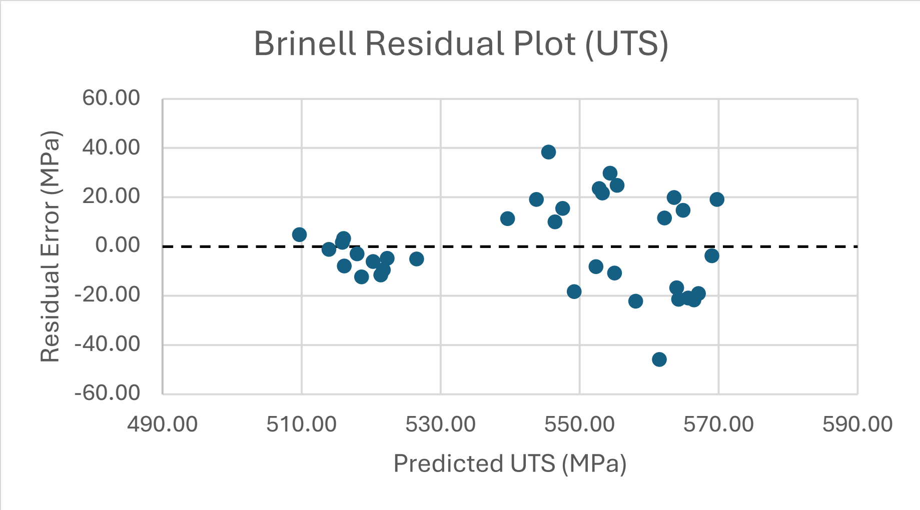
Brinell Residual Plot (UTS)
Residual Error (MPa)
60.00
40.00
20.00
0.00
-20.00
-40.00
-60.00
490.00
510.00
530.00
550.00
570.00
590.00
Predicted UTS (MPa)

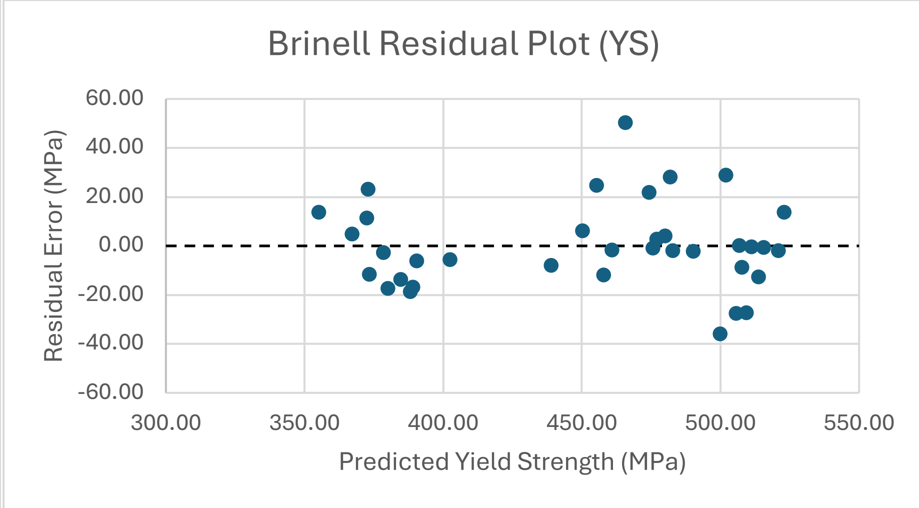
Brinell Residual Plot (YS)
Residual Error (MPa)
60.00
40.00
20.00
0.00
-20.00
-40.00
-60.00
300.00
350.00
400.00
450.00
500.00
550.00
Predicted Yield Strength (MPa)

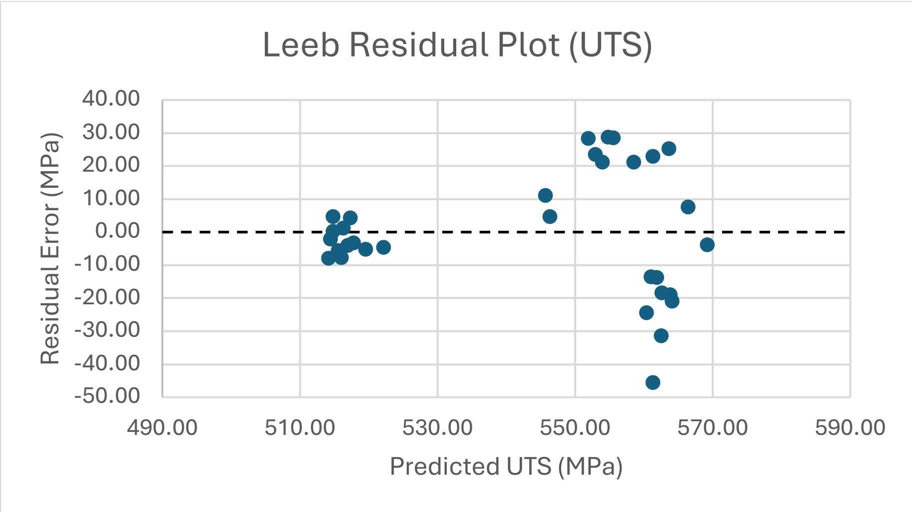
Leeb Residual Plot (UTS)
Residual Error (MPa)
40.00
30.00
20.00
10.00
0.00
-10.00
-20.00
-30.00
-40.00
-50.00
490.00
510.00
530.00
550.00
570.00
590.00
Predicted UTS (MPa)

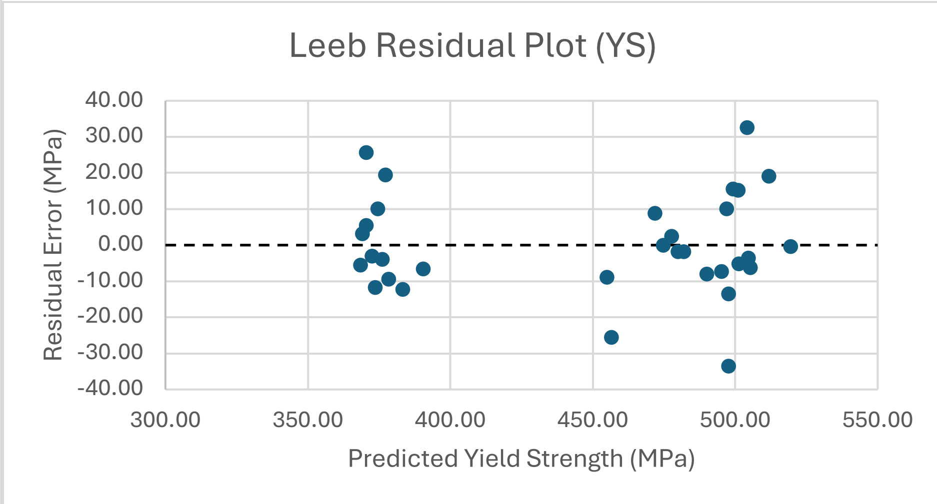
Leeb Residual Plot (YS)
Residual Error (MPa)
40.00
30.00
20.00
10.00
0.00
-10.00
-20.00
-30.00
-40.00
300.00
350.00
400.00
450.00
500.00
550.00
Predicted Yield Strength (MPa)

F.4 Regression Sensitivity Analysis (Inclusion of Invalid Boundary Data)

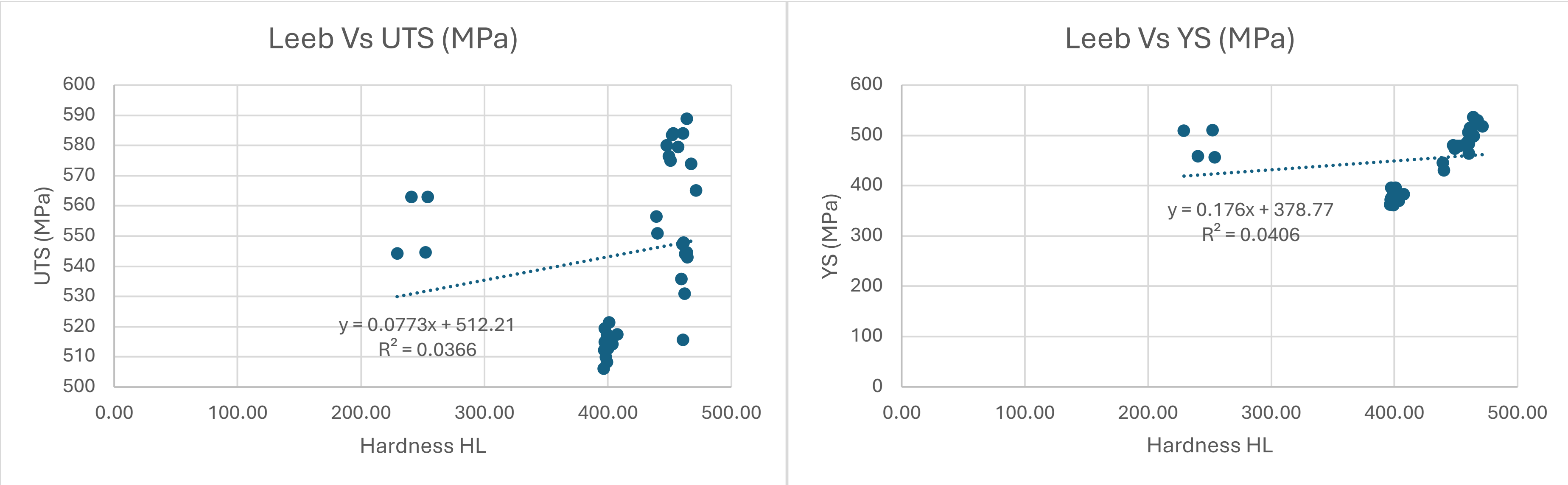

Figure F. 1: Regression sensitivity analysis demonstrating the catastrophic statistical degradation of the Leeb vs. Ultimate Tensile Strength (left) and Leeb vs. Yield Strength (right) models when mechanically invalid, uncoupled specimens (HL < 300) are reintroduced to the dataset. The inclusion of these boundary-violating data points mathematically collapses the coefficient of determination ($R^2 < 0.05$).

Appendix G: In-Situ Field Testing Raw Data

Table G. 1: Raw Leeb hardness (HL) measurement logs for in-situ structural elements.

	Point						
Structural Element	**1**	**2**	**3**	**4**	**5**	**Mean**	**calculated YS (MPa) using regression formula**
Thin RHS (Floor Decking)	240	254	218	240	220		N/A (Invalid Scatter)
C-Channel (Cabin Chassis)	366	363	368	359	371	365.4	305.89
Rusted UB	399	386	394	395	394	393.6	362.69